Visible Light Communications Based Indoor Tracking and Navigation

A Dissertation
Presented to
the Faculty of the School of Engineering and Applied Science
University of Virginia

In Partial Fulfillment
of the Requirements for the Degree
Doctor of Philosophy in Electrical Engineering

by

Zafer Vatansever

May 2019

APPROVAL SHEET

This dissertation is submitted in partial fulfillment of the
requirements for the degree of
PhD in Electrical Engineering

Zafer Vatansever, Author

This dissertation has been read and approved by the examining committee:

Prof. Maite Brandt-Pearce, PhD Advisor

Prof. Stephen G. Wilson, Committee Chair

Dr. Daniel S. Weller

Dr. Nicola Bezzo

Dr. Madhur Behl

Accepted for the School of Engineering and Applied Science:

Dean, School of Engineering and Applied Science

May 2019

Abstract

Visible light communications (VLC) using LED lights as transmitters is an emerging technology that can provide services such as illumination, localization, and mapping, in addition to communications. Since the visible light spectrum is unregulated, and the cost of VLC systems is decreasing, the widespread deployment of VLC systems is imminent.

In this dissertation, we begin by introducing a powerful VLC-based indoor positioning method that uses probabilistic tracking filters and a pre-collected database of optical power distribution, also known as a fingerprint map. In fingerprint-based localization methods, the location-related data collection process needs to be done *a priori*. This makes fingerprint-based localization algorithms difficult to use. We propose three ways of automating or progressively building the fingerprint map. In the first method, we utilize methods from geological science that are used to build a map of a surveillance area, namely, ordinary Kriging and radial basis functions. In the second method, we propose to equip the lamps with cameras to capture the light intensity distribution. The fingerprint map can be extracted from these images. In the final method, we rely on a large number of users that are connected to Wi-Fi to collect the light intensity measurements for us. We test the effect of these different data collection methods on agent tracking using Kalman and particle filters and find that the localization accuracy remains on the order of the fingerprint map resolution despite collected data inaccuracies. We also investigate the effect of unexpected failures in the VLC infrastructure on agent tracking. The root mean square error (RMSE) of VLC-fingerprint tracking is around 6 centimeters for a fingerprint grid step size of 10 centimeters.

To achieve accurate localization, prior belief in the landmark locations must be absolute. In reality, the landmark locations may not be given *a priori*. We use

a distance geometry based method to localize the LED landmarks. The method does not require any prior information about either the LED or the agent location. The resulting agent localization accuracy decreases proportionally to the landmark localization error. The landmark localization RMSE is better than 20 centimeters for our proposed method, and the agent tracking RMSE is around 10 centimeters.

After localizing itself, an agent needs to learn its environment. Indoor mapping is a problem that has garnered much attention, and the widely accepted solution is to use LIDAR. Although LIDAR provides excellent maps with high fidelity, they are bulky, expensive, and signal processing intensive. In this dissertation, we propose a sparse indoor mapping method that requires lightweight signal processing and inexpensive sensor design. We utilize the channel state information (CSI) of the optical wireless communication system and obtain the time-of-flight of the reflected light rays from the CSI. The technique is able to generate a coarse outline of the indoor space with respect to the agent position. With the use of an additional outlier rejection step, the mapping RMSE reduces to less than 5 centimeters at high signal-to-noise ratio values.

Acknowledgements

First of all, I owe my deepest appreciation to my advisor, Prof. Maite Brandt-Pearce, for her relentless support, understanding, and patience. It was her persistent encouragement which pushed me to be my best and guided me in the right direction whenever I was lost. She inspired me not only as a role model but also as a friend. Her leadership, exemplary work ethic, determination, and positiveness fostered my personal and academic skills.

My gratitude extends to my dissertation advisory committee members, Prof. Stephen G. Wilson, Prof. Daniel S. Weller, Prof. Nicola Bezzo and Prof. Madhur Behl, for their invaluable time and helpful suggestions. Additionally, I am appreciative of the support and services of the folks in the administration office in the Department of Electrical and Computer Engineering at UVa.

I want to acknowledge the financial support given to me by the Republic that M. Kemal Ataturk has founded, the UVa Research Innovation Grant, National Science Foundation, and the Department of Electrical and Computer Engineering.

Without the love and support of my family, this would have been an insurmountable journey. I cannot thank enough my parents, Yusuf and Nalan, my wife, Serap, and my sister, Zeynep, for giving me an unwavering love and support. I dare not even imagine how it would have been without them! I strive every day to make them proud! I thank my parents for teaching me the virtues of hard work, honesty, and honor. My wife for giving me such love and support during the dark times, despite all the sacrifices asked of her. My love for them is eternal. This dissertation was impossible without their support.

I dedicate this work to the victims of oppression, torture, racism, and discrimination.

Contents

List of Figures

List of Tables

List of Acronyms

AOA: Angle-of-arrival

CIR: Channel impulse response

CSI: Channel state information

EKF: Extended Kalman filter

FOV: Field-of-view

GPS: Global positioning system

IPN: Indoor positioning and navigation

KF: Kalman filter

LBS: Location-based service

LED: Light-emitting diode

LIDAR: Light detection and ranging

LOS: Line-of-sight

NLOS: Non-line-of-sight

OWC: Optical wireless communications

PD: Photodetector

PF: Particle filter

RANSAC: Random sampling and concensus

RBF: Radial basis function

RMSE: Root mean square error

RSS: Received signal strength

SNR: Signal-to-noise ratio

SLAM: Simultaneous localization and mapping

TOA: Time-of-arrival

VCSEL: Vertical-cavity surface-emitting laser

VLC: Visible light communications

VLP: Visible light positioning

WSN: Wireless sensor network

Chapter 1

Introduction

Localization and mapping are critical tasks towards *contextual understanding*[1] of the environment that an agent interacts. An agent can be identified as a mobile user electronic device, a robot, or any machinery that has sensing capabilities. These devices or automata can perform several tasks, such as sensing, service, and surveillance. *Location-aware*[2] algorithms, which help to process location-related data from remote sensing, create energy efficient, smart spaces, as well as provide location-based services (LBS).

In this dissertation, we propose a suite of algorithms that enable the use of optical wireless communication systems for inexpensive and accurate location and mapping of indoor spaces. The outdoor localization problem is solved by the global positioning system (GPS) that relies on orbital satellites [3]. However, localization of an agent indoors is still an open problem since there is no consensus on a single technology like GPS [4]. For indoors, the mapping problem is generally solved by light detection and ranging (LIDAR) systems or camera sensors. Considering the limited resources of a mobile device and high cost of LIDARs, there is a need for low-cost position-

[1] Contextual understanding refers to providing data related to the physical medium of an agent.
[2] The ability to localize oneself and make informed plans and decisions.

ing and mapping methods that use cheap sensors and inexpensive signal processing algorithms.

There are several competing technologies to solve the indoor localization and mapping problem, such as Wi-Fi, Bluetooth, ultra-wideband, imaging (still and video), and ultrasound [4]. The advancement of semiconductor technology has made new, low-cost devices such as light-emitting diodes (LED) and vertical-cavity surface-emitting lasers (VCSEL) commonplace. These devices have made visible light another candidate signal to solve the localization and mapping problem [5, 6].

In this chapter, the motivation for developing an optical wireless-based indoor localization and mapping system is introduced, and the research goals of this dissertation are summarized.

1.1 Background

GPS systems cannot be adopted indoors. Challenges for indoor positioning include severe signal reflection, signal attenuation, non-line-of-sight (NLOS) conditions, fast temporal changes, and requirements of high positioning accuracy [5].

A recent research report [7] shows that the market for indoor positioning applications will be around $4.4 billion by the end of 2019. Considering that people spend most of their time indoors and hand-held mobile devices with ever-increasing capabilities are everywhere, the indoor positioning and navigation market is expected to grow in the future. The possible applications of indoor positioning and navigation services can be listed as

- Location aware personalized advertising,
- Wayfinding/indoor navigation,

- Human or asset tracking,
- Point of interest search, and
- Healthcare applications.

Potential deployment areas of such systems can be any indoor area such as airports, hospitals, offices, shopping malls, and museums.

The problem of indoor positioning and navigation (IPN) consists of many steps that are interconnected as shown in Fig.1.1. Indoor applications of IPN, especially localization, include many open research issues. Furthermore, there is still a need for smaller, cheaper, and energy efficient sensors for IPN applications.

The IPN problem has garnered much attention in the last decade. There are many IPN-enabling signal media available, as shown in Fig. 1.2:

***Computer vision*:** Computer vision (CV) systems use camera inputs, extract features from these images, and use them to detect landmarks and locate the agent [8,9]. CV-based solutions require the camera to be on during the localization process. They can, therefore, drain the battery on a mobile agent, and the signal processing can be expensive.

***Ultrasound*:** Ultrasound is an active sensing method that uses high-frequency sound waves. It is one of the oldest localization solution, e.g., SONAR, [10]. The idea is to calculate the time-of-flight (TOF) of the transmitted sound.

***Inertial measurement unit*:** Inertial measurement unit (IMU) is a name given to a combination of sensors such as accelerometer, gyroscope, and magnetometer. These systems have been used since the dark ages in the form of an astrolabe and compass. They are used both for outdoor and indoor applications [11].

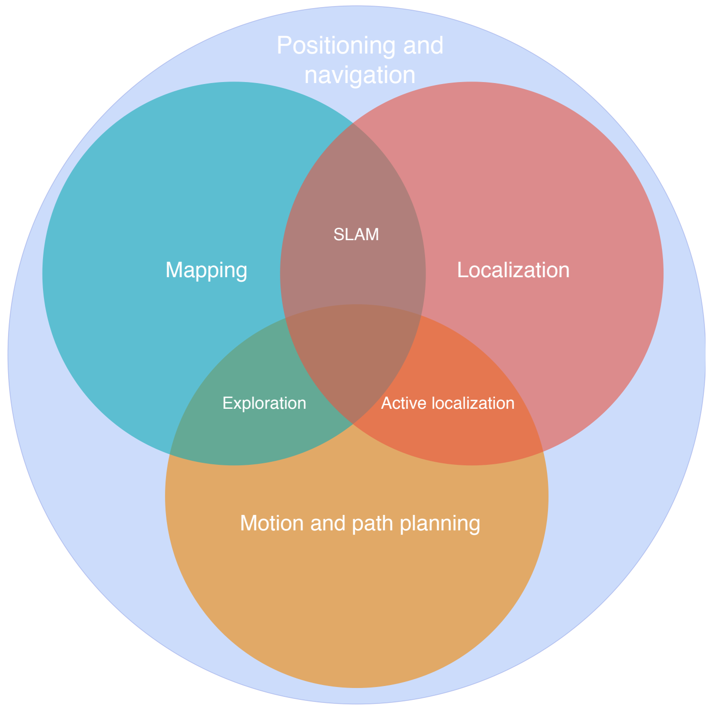

Figure 1.1: Complete positioning and navigation problem. Figure adopted from [1]. (SLAM is an abbreviation for simultaneous mapping and localization.)

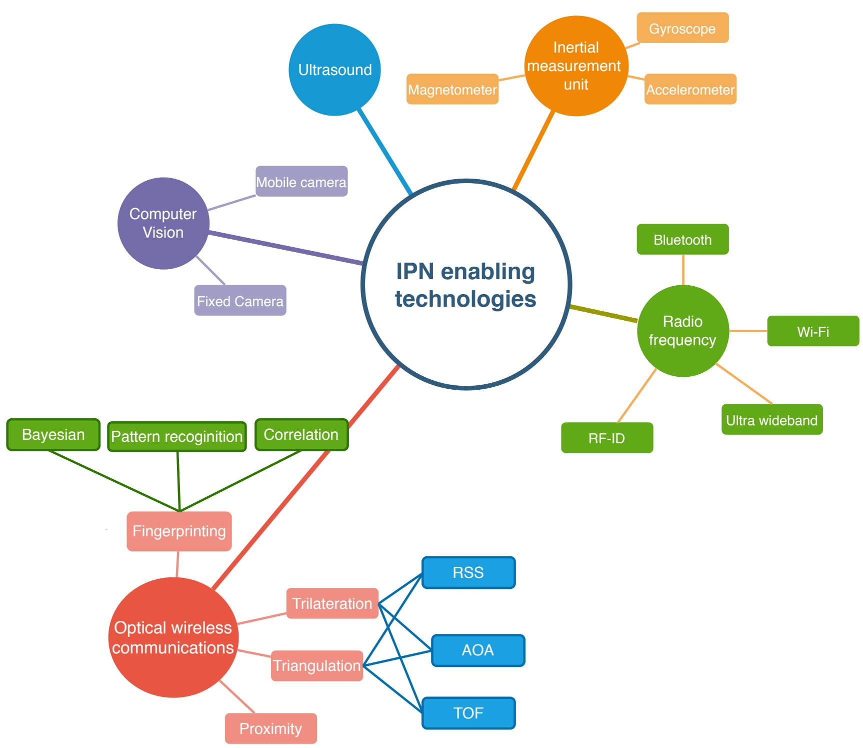

Figure 1.2: Technologies adopted for indoor positioning and navigation.

***Ultra wideband*:** RF signals with hundreds of MHz of bandwidth can be used as active location devices, similar to radar, and called ultra wideband systems. The effects of small scale fading are minimized for an ultra wideband system compared with narrowband RF, which enables accurate distance estimation from the path loss model [12].

***Bluetooth*:** Bluetooth is a popular RF short-range connectivity standard. Its beacons consume less energy than Wi-Fi access points, which make them a suitable candidate for solving the indoor localization problem. Bluetooth fingerprinting is a well-known technique [13].

***Other RF techniques*:** Radio frequency systems can use the Wi-Fi infrastructure [14] or RF-ID technologies [15]. The pervasive deployment of Wi-Fi favors these approaches. On the other hand, the low cost and low energy requirements of RF tags create localization solutions for industrial problems [16].

***Optical wireless communications*:** Communication systems that use light to transmit signals have been used in fiber-optic communications for a long time. The use of free space optical systems indoors has been an active research topic since the early 2000s. There are several advantages of optical wireless communication (OWC) systems such as the deterministic nature of light propagation, unregulated spectrum, wide-spread deployment of lighting fixtures indoors, and inexpensive and low energy sensors, e.g., photodetectors (PD). Our work focuses on OWC solutions, with an emphasis on a PD as the receiver, and systems that employ LED lighting infrastructure and/or an agent-mounted laser diode.

The technologies discussed so far can be used in cooperation, as complementary, or interchangeable with each other. The solutions used for localization are similar to each other. These method are generally divided into three types: multilateration-multiangulation [17], proximity [18], and fingerprinting [19].

- Multilateration methods rely on estimating the distance to a landmark such as a light-emitting diode (LED) lamp, with a known location. The types of measurements used for distance estimation are the optical received signal strength (RSS) and the time-of-flight (TOF). If the RSS is used, the propagation loss of the channel is used to calculate the distance from at least three landmarks to find the location of the agent [17].

- Multiangulation is similar to multilateration. This method uses angle-of-arrival (AOA) measurement to locate the agent with respect to at least three landmarks [20]. This technique requires a receiver array to estimate the angles.

- Proximity methods require a dense grid of landmarks, such as lighting fixtures, with known positions, each transmitting its location information and a unique identifier. The user location is estimated by the agent's proximity to the LED landmark locations [18, 21].

- Fingerprint-based localization is the focus of research in this study. The word fingerprint is used to represent a quantity measured at known locations and is stored in a database, also known as a fingerprint map or *site survey*. Bayesian filtering, pattern recognition, and correlation algorithms can be used to match the online measurements with the *a priori* collected fingerprint map [19].

In this dissertation, we tackle the problem of indoor localization and mapping using OWC, as depicted in Fig 1.3. In the first part of our work, we focus on agent localization. We use the optical RSS to build a fingerprint map. This map is used as a look-up table in probabilistic tracking filters. In Fig.1.3, the blue encircled part represents our localization focused research.

The localization problem we consider in this part of the work is not limited to agent localization. Most localization problems assume that the landmark locations are known beforehand: we also look at a scenario where the LED landmark locations are unknown. We use a distance geometry based method that does not require any prior information about the agent location.

Our second effort consists of building a sparse map of the surveillance area by observing the channel state information, such as the RSS and channel impulse response (CIR). Our OWC-based indoor mapping algorithms work in conjunction with an inexpensive sensor, a PD, and simple signal processing algorithms. In Fig.1.3, the green encircled part represents our mapping focused research.

The goal of this study is to propose a complete and versatile OWC-based indoor mapping and localization system. A broad application spectrum ranging from LBS to remote sensing can benefit from our proposed solutions.

1.2 Research Goals

The primary goal of this dissertation is to propose a complete localization and mapping system that does not require expensive sensors, intensive computing, or abundant deployment, and provides high accuracy. The following is a detailed description of the research metrics of this dissertation.

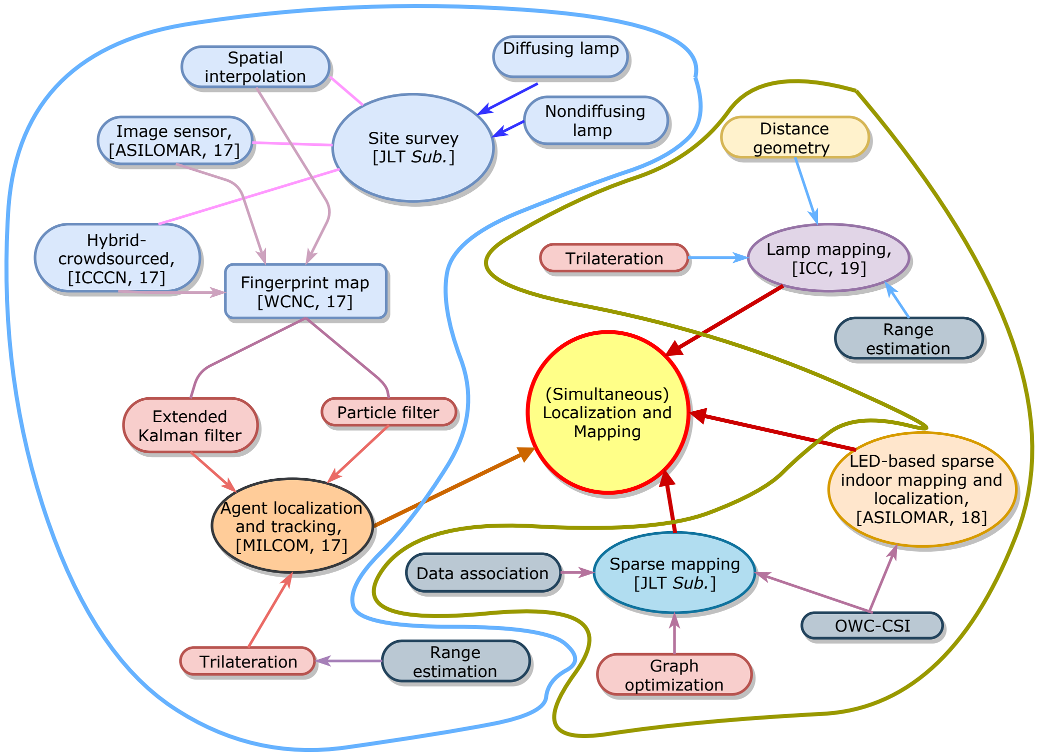

Figure 1.3: Overview of the research described in this dissertation.

Requirement-oriented

The versatility of fingerprint-based solutions comes from the fact that they can be tailored depending on the accuracy requirements. Fingerprint databases store *a priori* collected location-related data. The granularity of the data collection dictates the accuracy of the algorithm. In addition, while collecting this database, applications such as mapping, remote sensing, and occupancy detection can be realized by collecting other features.

Accuracy

The primary goal of a localization algorithm is to pinpoint the agent location. The main localization approaches used in this dissertation are fingerprint-based and range-based approaches. Our metric of accuracy evaluation of the proposed solutions is the root mean square error (RMSE) of the position estimate.

Cost

A critical design criterion in this dissertation is low cost and low complexity. LED-based lighting schemes for indoor spaces are expected to be widespread in the near future, which will make LEDs ubiquitous. Unlike other technologies, OWC-based IPN systems will not result in any additional infrastructure cost. In addition, user electronic devices have already embraced LEDs, VCSELs, and PDs. Landmark discovery and mapping applications can benefit from these device-integrated transmitters.

Computational Cost

LIDARs and cameras adopted for mapping solutions use resource-hungry signal processing algorithms that lead to high power consumption and computation such as iterative cloud point or scan matching algorithms that require constant updates. The signal processing and feature extraction processes in our methods are designed for frugal energy consumption in mind, which leads to a rapid sparse map building process.

1.3 Literature Review

As OWC research has advanced, visible light positioning (VLP) has become increasingly popular. In this section, we describe recent works on VLP triangulation, fingerprinting, and proximity, defined above. Indoor mapping applications that use OWC channel state information (CSI) are new to the literature.

Indoor localization using OWC

The deterministic nature of light allows extracting distance and angle features accurately from the measurements. Two main sensor types used in VLP research are cameras and PDs [5, 22].

Distance between the transmitter and receiver is calculated using the VLC channel model, and multilateration is used for finding the position of the agent in [17]. An important assumption is that the positions of the transmitter and the receiver planes are parallel to each other. A simplified approach when the relationship between the irradiance angle and the incidence angle are not given *a priori* may lead to inaccurate localization. The problem of a tilted receiver is considered in [23–25]. The estimation of a tilted receiver requires a combination of AOA and RSS approaches.

The multiangulation approach is similar to multilateration. Multiangulation requires complicated PDs or cameras to extract angular information or location of the LED landmarks. A combination of multiple PDs that are facing different directions can be used for multiangulation from the AOA measurements [14, 26, 27]. Another sensor type commonly used in VLP research is a camera [20]. The high power consumption of cameras makes them undesirable for mobile applications, and therefore they are not considered in this dissertation.

Fingerprint approaches are more challenging to implement in real-life because building and maintaining a fingerprint database that consists of the optical RSS is a hard problem due to several challenges for VLP indoor positioning including people, obstructions of line-of-sight (LOS), non-line-of-sight (NLOS) conditions, perturbations in the transmitted optical power from the LEDs, other fast temporal changes, and requirements of high positioning accuracy [5, 28]. Fingerprinting for RF-based indoor localization such as Wi-Fi RSS is a well-studied problem [29, 30]. In the context of VLP, fingerprint methods assign a unique frequency or code to each LED, so that the optical RSS from the LEDs can be distinguished [19, 31, 32] at the receiver. A common approach to locate the agent is to match the online measurement with the fingerprint (offline) database using the nearest neighbor algorithm [33, 34]. Although

2D [19] and 3D [33] VLC fingerprinting localization solutions are available [30,32,35], there are limited efforts in automated building and maintaining an optical fingerprint map in the literature. One of the critical contributions of this dissertation is to automate or aid the fingerprint map building process.

Landmark discovery in OWC-networks

In a localization and mapping problem, the locations of the landmarks are used as reference points (anchors) that the agent locates itself with respect to. This topic is well studied under the auspices of wireless sensor networks [36]. In this dissertation, we aim to localize unknown LED landmarks using a method called distance geometry [36, 37]. While other methods, such as multilateration and nonlinear least squares, require the locations of the measurements, distance geometry method does not require any prior knowledge about the agent and the landmark locations.

Indoor mapping using channel state information:

In this dissertation, we use the location of a reflector as the primary basis for map-building. The RF systems have been known since a long time to exploit the use of channel state information for reflector location. The estimation of a reflector's location using multipath has been described in many studies using RF signals [38–40]. There are growing interest and re-discovery of using non-line-of-sight (NLOS) components of the RF signal for localization and obstacle detection [41–43].

In the context of using light, TOF sensors, e.g., LIDAR, are the most widely used sensor type for indoor mapping applications [44]. LIDARs consist of an array of light emitters (edge-emitting lasers or VCSELs) and receivers (PD) [45]. However, these sensors are bulky, expensive, and resource intensive. In OWC systems, the word "mapping" is generally used for building a database of fingerprints of channel features, such as CIR and RSS [19,31,34]. In this dissertation, our proposed solutions for indoor mapping cover building a sparse physical map based on the LED landmarks or wall locations.

1.4 Dissertation Organization

The dissertation is organized as follows:

Chapter 2 describes the OWC channel model. The LED lamp models used are introduced. OWC channel features used during the entire dissertation are explained.

Chapter 3 is an overview of the localization, tracking, and mapping algorithms, which introduces the workhorse signal processing concepts used: the Kalman and particle filters. Simultaneous localization and mapping methods such as extended Kalman filter and graph optimization are explained. Finally, deterministic localization methods such as multilateration and distance geometry are introduced.

In Chapter 4, we introduce our OWC fingerprint-based localization algorithm. We introduce methods for automating the data collection process for fingerprint database preparation. Furthermore, we discuss the effect of errors unbeknownst to the system on the tracking performance.

Chapter 5 explains how an LED landmark can be localized without any prior location information. We also discuss the advantages of the proposed method by comparing it to traditional wireless sensor network localization approaches.

Mapping using the channel state information is described in Chapter 6. We begin this chapter by introducing a mapping and localization method that relies on the LED infrastructure. Next, we extend the problem and propose a solution that can reduce the cost of traditional mapping approaches both computationally and economically.

Chapter 7 summarizes the whole dissertation and provides, concludes regarding the results. The contributions of this dissertation are explained. Future research directions are also discussed.

Chapter 2

Optical Wireless Communications Systems

The spectrum crunch for the RF wavebands, the unregulated spectrum of the visible light, and the pervasive deployment of LEDs that ranges from ceiling mounted luminaries to consumer electronic devices have led an ever-growing interest in optical wireless communications (OWC) systems, also known as visible light communications (VLC). The goal of this chapter is to give an overview of OWC systems and discuss how these systems are adopted for our localization and mapping methods.

2.1 OWC Channel Model

For indoor VLC systems, the received optical signal can be represented as

$$P_r(t) = P_T(t) * h(t) + n(t), \tag{2.1}$$

where the operator "$*$" denotes convolution, $P_T(t)$ is the transmitted optical intensity, and $n(t)$ is the additive noise that includes thermal and shot noises. $h(t)$ is the indoor channel impulse response that can be modeled as

$$h(t) = h_{\text{LOS}}(t) + h_{\text{NLOS}}(t), \tag{2.2}$$

where $h_{\text{LOS}}(t)$ and $h_{\text{NLOS}}(t)$ are the line-of-sight (LOS) and non-line-of-sight (NLOS) parts of the received light, respectively. The LOS part represents the light that is received directly from the LED; the NLOS part is caused by multiple reflections from the walls as shown in Fig. 2.1 (a). An example of an impulse response of an indoor VLC channel is illustrated in Fig. 2.1 (b), in which the first peak is the LOS part, and the NLOS components cause the other peaks with long tails. Given specific information about an indoor environment, the impulse response can be approximated by using ray tracing [46].

For commonly used light sources that have an unrestricted beam shape, e.g., LEDs, the intensity of the emitted light for a particular radiation angle ϕ can be modeled using the Lambertian law [46]. The LOS link gain between a transmitter and a receiver can thus be described as

$$h_{\text{LOS}} = \frac{(m+1)}{2\pi d^2} A_r \cos^m(\phi)\cos(\varphi) \tag{2.3}$$

where d is the propagation distance and φ represents the incident angle at the receiver. The parameter m represents the Lambertian mode, which depends on the LED's beamwidth semiangle. A_r is the photodetector (PD) active area. Note that the use of a light diffuser would change the beam characteristics.

The channel gain of each NLOS ray can be calculated as

$$h_{\text{NLOS}} = \sum_{i=1}^{\infty} \mathfrak{H}_i \varsigma^i, \tag{2.4}$$

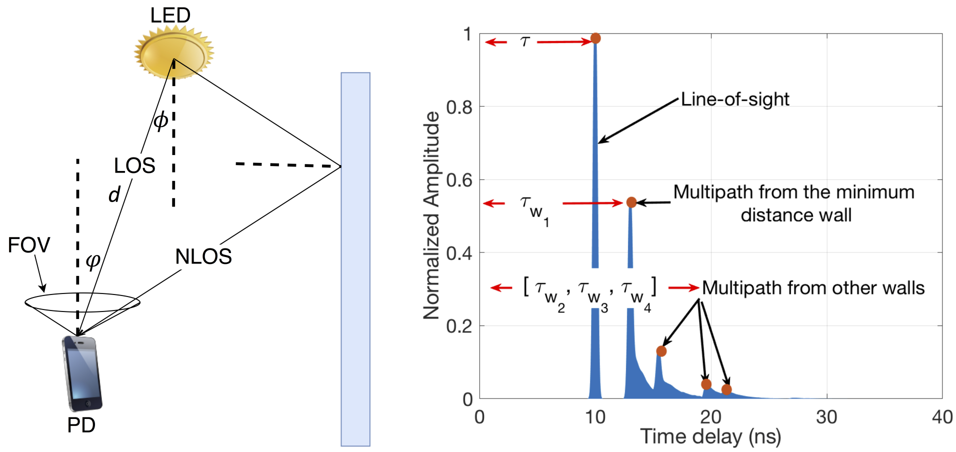

(a) (b)

Figure 2.1: Propagation of an optical wireless link. (a) shows the geometry of LOS and NLOS propagation of light. (b) shows the LOS and NLOS parts of the impulse response of the channel.

where ς is the wall reflection coefficient, and $\mathfrak{H}_i$ represents the ith bounce link attenuation,

$$\begin{aligned} \mathfrak{H}_0 &= \frac{(m+1)A_r \cos^m(\phi_0)\cos(\varphi_0)}{2\pi d_0^2} \\ \mathfrak{H}_1 &= A_r \frac{\cos(\phi_1)\cos(\varphi_1)}{\pi d_1^2} \\ &\vdots \\ \mathfrak{H}_k &= A_r \frac{\cos(\phi_k)\cos(\varphi_k)}{\pi d_k^2} \end{aligned}, \tag{2.5}$$

where d_k represents the distance of the kth bounce link. ϕ_k and φ_k are the radiation angle and incident angle at the kth bounce's diffusion point, respectively [47].

The complete impulse response is represented as the superposition of the LOS and the NLOS components with their appropriate gains and their delays based on the propagation distance of the ray from the lamp to the receiver.

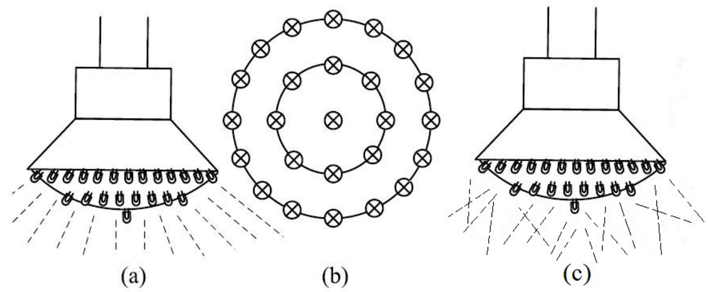

Figure 2.2: Nondiffusing lamp, (a) side view, b) bottom view. c) Diffusing lamp side view.

2.2 LED Transmitter Models

We use two different and commonly deployed LED lamp models [19]: nondiffusing and diffusing lamps. The LED layout configuration of both lamps consists of three layers, with 1, 8, and 16 LEDs, as shown in Fig. 2.2 (a) and (c). Fig. 2.2 (a) shows the light rays from a nondiffusing 25-LED lamp. A nondiffusing lamp consists of LEDs with fixed well-designed irradiance angles that do not change over time. The optical power distribution of the nondiffusing lamp is deterministic. Fig. 2.2 (c) represents the same 25-LED lamp but now using random irradiance angles (diffused model), which results in a unique (observable but not necessarily predictable) optical power distribution in the room.

The diffusing lamp model is a modification of the nondiffusing lamp. We introduce random transmission angles to mimic the random refraction of light beams through a crystal, as in a chandelier or a light diffuser [19]. The diffusing lamps are commonly used in large indoor spaces such as conference halls and museums. Classical architectural lighting styles for these environments include chandeliers, which contain many small moving crystal refracting elements that cannot be modeled as deterministic. In this dissertation, we address the ability to perform indoor positioning when chandeliers or other diffused light sources are used for VLP lighting.

In this dissertation, we modify the 25-LED lamp proposed in [48] to imitate the behavior of a diffusing lamp. Each LED has a random inclination angle; the random angle is used to model the refraction of light through a prism.

In Fig. 2.3, the difference between the power contours for deterministic and random 25-LED lamps is shown. Note that the radiation pattern emitted by the 25-LED lamp is practically identical to an equally bright single LED for 60° half angle emitters. The room is $5 \times 5 \times 3$ m^3, with four LED luminaries on the ceiling, positioned at $(x, y, z) = (1.25, 1.25, 3)$, $(1.25, 3.75, 3)$, $(3.75, 1.25, 3)$ and $(3.75, 3.75, 3)$. The transmitted power from each LED is 20 milliwatts, yielding a total transmitted power of 500 mW per lamp. The random irradiance angles of the diffusing model have a normal distribution with zero mean and standard deviation of 30°. In Fig. 2.3 (a), (b) and (e), the power distribution in the room floor when the deterministic lamp model is used with different LED semiangles is shown, while Fig. 2.3 (b), (d) and (e) shows the effect of random transmit angles when the proposed random (diffusing) model is used. The refraction of light through the diffuser results in nonuniform power distribution in the room.

2.3 Signal to Noise Ratio Analysis

There are two noise sources: shot and thermal noise in a classical signal-to-noise ratio (SNR) analysis for an OWC system [47]. Shot noise depends on the direct and ambient light. Thermal noise results from the electronic noise. Previous works, like [17, 49], assume these two are the main noise sources in the system.

In a real-world scenario, other unknowns affect the system; they are lumped together as *uncertainty* noise in this study. This uncertainty noise may be caused by the shadowing of the LOS between the transmitter and the UE, uneven dimming of

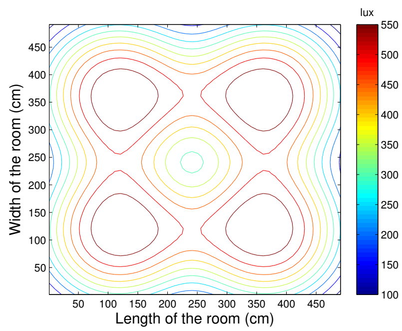

(a) Semiangle 10°

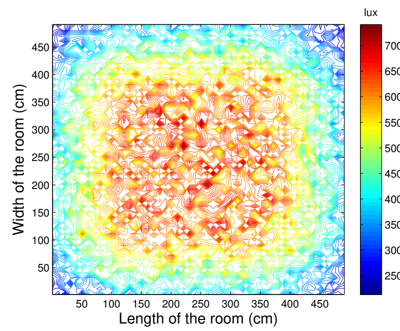

(b)Semiangle 10°

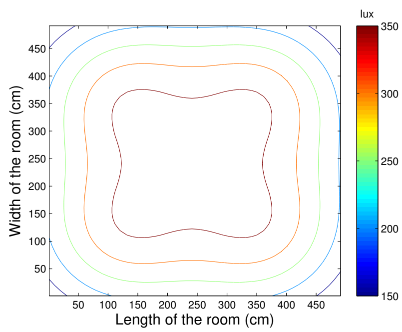

(c) Semiangle 30°

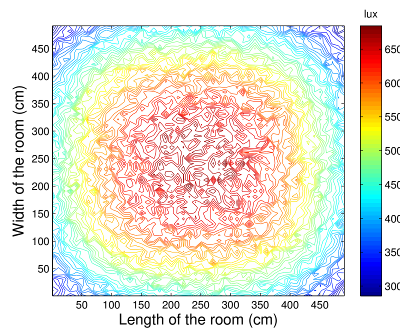

(d) Semiangle 30°

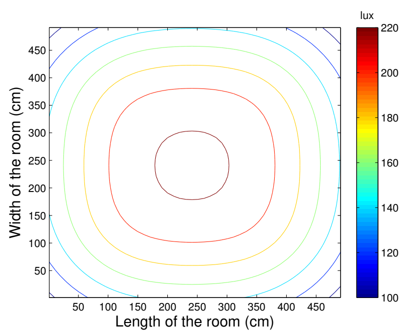

(e) Semiangle 60°

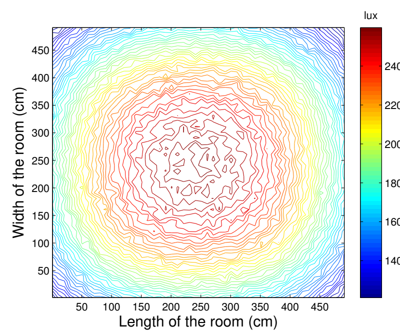

(f) Semiangle 60°

Figure 2.3: Top-down power contours of the room floor for (a), (c), (e) the deterministic 25-LED lamps and (b), (d), (f) the random inclination angle (diffusing) lamp model.

the lamps, uncertainties during the construction of the fingerprint map, an unknown inclination of the mobile device, etc. The SNR calculation for the system is modified as

$$SNR = \frac{\rho^2 P_r^2}{\sigma^2_{\text{shot}} + \sigma^2_{\text{thermal}} + \sigma^2_{\text{uncertainty}}} \tag{2.6}$$

where ρ is the receiver responsivity, and P_r is the average received optical power (RSS). Modeling the dependence of the uncertainty on P_r is beyond the scope of this thesis; its variance $\sigma^2_{\text{uncertainty}}$ is taken to be a constant that defines the effective SNR.

2.4 Summary

This chapter introduces the fundamental concepts of the OWC channel. The OWC channel equations play a critical role in accurate localization and mapping. Equations (2.3) and (2.4) are used in later chapters to calculate the distance between an OWC transmitter and receiver.

Chapter 3

Overview of Tracking and Mapping Algorithms

Simultaneous localization and mapping (SLAM) is a general name for the problem of localizing an agent while building a map of the environment. The goal of this dissertation is to answer three critical SLAM questions using an OWC system: *localization* of the agent, *initialization* of the landmarks, and *building* a map that stores quantitative features such as optical RSS, TOF, CIR, and physical features such as locations of LEDs, walls, and obstacles. To achieve these goals, we adopt probabilistic methods such as Kalman and particle filters, as well as deterministic methods of multilateration and distance geometry. In this chapter, we briefly overview these methods.

3.1 Agent Dynamic Models

Probabilistic tracking filters rely on accurate modeling of state dynamics of the target. In this section, we introduce two state dynamic models used in our work before introducing the probabilistic tracking filters.

3.1.1 Constant Velocity Model for Hand-held Mobile Devices

The agent is not expected to make sudden changes or random accelerations during its movement; for that reason, we use the well-known constant velocity model [50] for our simulations. The state vector is defined as $\mathbf{x}_t = [x_t,\ y_t,\ \dot{x}_t\ , \dot{y}_t]^T$, where x_t and y_t are the Cartesian coordinates of the agent at time sample index t. The corresponding velocity components are represented by $\dot{x}_t$ and $\dot{y}_t$. The state equation can be written as

$$\mathbf{x}_{t+1} = \underbrace{\begin{bmatrix} 1 & 0 & \Delta t & 0 \\ 0 & 1 & 0 & \Delta t \\ 0 & 0 & 1 & 0 \\ 0 & 0 & 0 & 1 \end{bmatrix}}_{\mathbf{A}_t} \begin{bmatrix} x_t \\ y_t \\ \dot{x}_t \\ \dot{y}_t \end{bmatrix} + \mathbf{q}_t \tag{3.1}$$

where $\mathbf{A}_t$ is the state transition matrix at time index t, Δt is the sampling time, $\mathbf{x}_t$, is propagated through, and $\mathbf{q}_t \sim \mathcal{N}(0, \mathbf{Q}_t)$ is a Gaussian distributed random process noise with covariance $\mathbf{Q}_t$ as described in [51]. The process noise is used to model the random acceleration between the measurements. Δt is the sampling time.

3.1.2 Differential Drive Dynamic Model for Mobile Robot

The dynamic model of the robot that is used in the mapping simulations of this dissertation is a differential drive model described in [52]. The state (pose) of the robot is represented as $\mathbf{x}_t = \begin{bmatrix} x_t,\ y_t,\ \theta_t \end{bmatrix}^T$, where x_t and y_t are the Cartesian coordinates of the robot at time t, and θ_t is the heading angle.

Fig. 3.1 illustrates the motion of the mobile agent for two time steps. Assume that the control input, $u_t = (v,\ w)^T$, is constant between t and $t+1$, where v is the

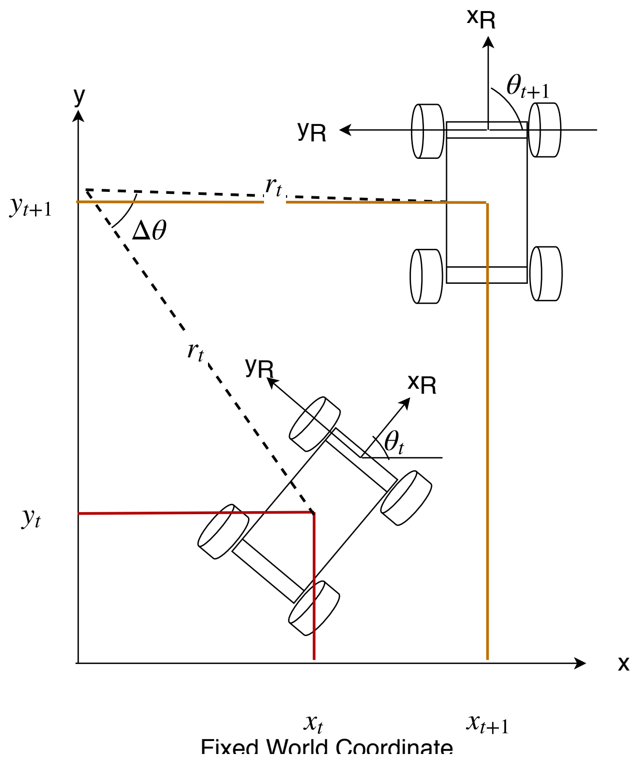

Figure 3.1: Ackermann steering model for mobile agent motion

translational velocity and w is the angular velocity. If the agent is turning, the radius of the turning circle can be found as

$$r_t = |\frac{v}{w}|. \tag{3.2}$$

The new state of the agent can be calculated using

$$\begin{bmatrix} x_{t+1} \\ y_{t+1} \\ \theta_{t+1} \end{bmatrix} = \begin{bmatrix} x_t + r_t(\sin(\Delta\theta + \theta_t) - \sin(\theta_t)) \\ y_t + r_t(\cos(\Delta\theta + \theta_t) - \cos(\theta_t)) \\ \Delta\theta + \theta_t \end{bmatrix} + n_{t+1} \tag{3.3}$$

where $\Delta\theta$ is the turning angle. If the agent is moving on a straight line, the equation of motion can be written as

$$\begin{bmatrix} x_{t+1} \\ y_{t+1} \\ \theta_{t+1} \end{bmatrix} = \begin{bmatrix} x_t + v\Delta t \\ y_t + v\Delta t \\ \theta_t \end{bmatrix} + n_{t+1} \tag{3.4}$$

where n_{t+1} is the additive noise that is used to model the uncertainties or noise in the system.

3.2 Probabilistic Tracking Filters

The definition of the word estimation is *"the process by which we infer the value of a quantity of interest* $\mathbf{x}$*, by processing data that is in some way dependent of* $\mathbf{x}$*"* according to [53]. We use state estimation to translate the optical measurements to physical quantities in this dissertation.

3.2.1 Bayes Filter

Bayes' rule allows us to estimate a value in a maximum *a posteriori* sense. If we have prior information and observations, we can calculate the value that maximizes the posterior distribution. Bayes' rule can be recursively expanded for time series. It allows us to calculate the posterior distribution using *a priori* information and time-stamped measurements in *predict*, *update*, and *normalize* steps [51].

- ***Initialization***: The recursion starts with a prior belief $p(\mathbf{x}_0)$,
- ***State space model***: $\mathbf{x}_t \sim p(\mathbf{x}_t|\mathbf{x}_{t-1})$,
- ***Measurement model***: $\mathbf{z}_t \sim p(\mathbf{z}_t|\mathbf{x}_t)$

We estimate the posterior state, $\mathbf{x}_t$, by using the measurement, $\mathbf{z}_t$,

$$p(\mathbf{x}_{t-1}|\mathbf{z}_{1:t-1}) \rightarrow p(\mathbf{x}_t|\mathbf{z}_{1:t}) \tag{3.5}$$

- ***Prediction*** step of the Bayes filter is calculated as follows:

$$p(\mathbf{x}_t, \mathbf{x}_{t-1}|\mathbf{z}_{1:t-1}) = p(\mathbf{x}_t|\mathbf{x}_{t-1}, \mathbf{z}_{1:t-1})p(\mathbf{x}_{t-1}|\mathbf{z}_{1:t-1}), \tag{3.6}$$

$$= p(\mathbf{x}_t|\mathbf{x}_{t-1})p(\mathbf{x}_{t-1}|\mathbf{z}_{1:t-1}), \tag{3.7}$$

$$p(\mathbf{x}_t|\mathbf{z}_{1:t}) = \int p(\mathbf{x}_t|\mathbf{x}_{t-1})p(\mathbf{x}_{t-1}|\mathbf{z}_{1:t-1})d\mathbf{x}_{t-1}, \tag{3.8}$$

- ***Update*** step of the Bayes filter is calculated using the predicted (prior) distribution and the measurement as follows:

$$p(\mathbf{x}_t|\mathbf{z}_{1:t}) = \frac{1}{p(\mathbf{z}_t|\mathbf{z}_{1:t-1})}p(\mathbf{z}_t|\mathbf{x}_t)p(\mathbf{x}_t|\mathbf{z}_{1:t-1}), \tag{3.9}$$

$$p(\mathbf{z}_t|\mathbf{z}_{1:t-1}) = \int p(\mathbf{z}_t|\mathbf{x}_t)p(\mathbf{x}_t|\mathbf{z}_{1:t-1})d\mathbf{x}_t. \tag{3.10}$$

  Recall that the measurements are conditionally independent.

3.2.2 Linear-Discrete Kalman Filter

In this section, we describe an extension of recursive Bayes filters that uses a Gaussian approximation and matrix multiplications known as the Kalman filter (KF). Introduced in the seminal paper [54], the KF is one of the most potent state estimation tools. The KF is the best linear unbiased estimator in the minimum mean square error (MMSE) sense when the process and the measurements are linear, and the associated noise distributions are Gaussian.

Unbiased estimator: Dropping the time indices, when the expected value of an estimated quantity, $\mathbb{E}[\hat{\mathbf{x}}]$, e.g., the predicted state of the robot, and the expected value of the quantity $\mathbf{x}$, $\mathbb{E}[\mathbf{x}]$, are equal, then the estimator is said to be *unbiased*:

$$\mathbb{E}[\hat{\mathbf{x}}] = \mathbb{E}[\mathbf{x}]. \tag{3.11}$$

Then, given the measurement, $\mathbf{z}$, and the variance defined as $\mathbb{E}[||\mathbf{x}-\hat{\mathbf{x}}||^2]$, a minimum variance unbiased estimation is defined as

$$\hat{\mathbf{x}} = \arg\min_{\hat{\mathbf{x}}} \mathbb{E}[||\mathbf{x} - \hat{\mathbf{x}}||^2|\mathbf{z}] = \mathbb{E}[\mathbf{x}|\mathbf{z}], \tag{3.12}$$

where $\mathbb{E}[||\mathbf{x} - \hat{\mathbf{x}}||^2] = trace(\mathbb{E}[(\mathbf{x} - \hat{\mathbf{x}})(\mathbf{x} - \hat{\mathbf{x}})^{\mathrm{T}}])$.

Linear State Space Representation:

To derive the KF, we first introduce a linear state space model

$$\mathbf{x}_t = \mathbf{A}_{t-1}\mathbf{x}_{t-1} + \mathbf{q}_{t-1} \tag{3.13}$$

$$\mathbf{z}_t = \mathbf{H}_t\mathbf{x}_t + \mathbf{r}_t, \tag{3.14}$$

where t is the time index, $\mathbf{x}$ is the state of the agent, and $\mathbf{z}$ is the measurement. $\mathbf{q}_{t-1}$ and $\mathbf{r}_t$ are the process and the measurement noise, with $\mathcal{N}(0, \mathbf{Q}_{t-1})$ and $\mathcal{N}(0, \mathbf{R}_t)$ distributions, respectively. $\mathbf{A}$ is the state transition matrix. $\mathbf{H}$ is the measurement matrix. The prior distribution of the initial state is assumed to be known and is given as $\mathbf{x}_0 \sim \mathcal{N}(\hat{x}_0, \hat{P}_0)$.

Similar to a general Bayes filter, the KF consists of predict and update states:

- ***Prediction***

$$\hat{\mathbf{x}}_{t|t-1} = \mathbf{A}_{t-1}\hat{\mathbf{x}}_{t-1|t-1} + \mathbf{u}_t \tag{3.15}$$

$$\mathbf{P}_{t|t-1} = \mathbf{A}_{t-1}\mathbf{P}_{t-1|t-1}\mathbf{A}_{t-1}^{\mathrm{T}} + \mathbf{Q}_{t-1} \tag{3.16}$$

- ***Update***

$$\nu_t = \mathbf{z}_t - \mathbf{H}_t\hat{\mathbf{x}}_{t|t-1} \tag{3.17}$$

$$\mathbf{S_t} = \mathbf{H}_t\mathbf{P}_{t|t-1}\mathbf{H}_t^T + \mathbf{R}_t \tag{3.18}$$

$$\mathbf{K}_t = \mathbf{P}_{t|t-1}\mathbf{H}_t^{\mathrm{T}}\mathbf{S_t}^{-1} \tag{3.19}$$

$$\hat{\mathbf{x}}_{t|t} = \hat{\mathbf{x}}_{t|t-1} + \mathbf{K}_t\nu_t \tag{3.20}$$

$$\mathbf{P}_{t|t} = \mathbf{P}_{t|t-1} - \mathbf{K}_t\mathbf{S_t}\mathbf{K}_t^{\mathrm{T}} \tag{3.21}$$

where $\mathbf{u}_t$ is the control input, ν_t is the innovation, $\mathbf{S}_t$ is the innovation covariance, and $\mathbf{K}_t$ is the Kalman gain, all at time t.

3.2.3 Extended Kalman Filter

In real life situations, the process and/or the measurement equations may be nonlinear functions of the state. For example, the Euclidean distance is a nonlinear function of the agent and landmark locations. The extended Kalman filter (EKF) uses the Jacobian of the nonlinear equations in the system [51]. This leads to sub-optimal filter performance. Assume that the dynamic model of the agent and the measurement function are nonlinear in the following form:

$$\begin{gathered} \hat{\mathbf{x}}_{t|t-1} = \mathbf{a}(\hat{\mathbf{x}}_{t-1|t-1}, \mathbf{u}_t, t) + \mathbf{q}_{t-1} \\ \mathbf{z}_t = \mathbf{h}(\hat{\mathbf{x}}(t|t-1)) + \mathbf{r}_t \end{gathered} \tag{3.22}$$

The Jacobian of **a** and **h** in (3.22) is calculated as follows:

$$\nabla \mathbf{A}_t = \frac{\partial \mathbf{a}}{\partial \mathbf{x}} = \begin{bmatrix} \frac{\partial \mathbf{a}_1}{\partial \mathbf{x}_1} & \cdots & \frac{\partial \mathbf{a}_1}{\partial \mathbf{x}_m} \\ \vdots & \ddots & \vdots \\ \frac{\partial \mathbf{a}_n}{\partial \mathbf{x}_1} & \cdots & \frac{\partial \mathbf{a}_n}{\partial \mathbf{x}_m} \end{bmatrix}, \ \nabla \mathbf{H}_t = \frac{\partial \mathbf{h}}{\partial \mathbf{x}} = \begin{bmatrix} \frac{\partial \mathbf{h}_1}{\partial \mathbf{x}_1} & \cdots & \frac{\partial \mathbf{h}_1}{\partial \mathbf{x}_m} \\ \vdots & \ddots & \vdots \\ \frac{\partial \mathbf{h}_n}{\partial \mathbf{x}_1} & \cdots & \frac{\partial \mathbf{h}_n}{\partial \mathbf{x}_m} \end{bmatrix} \tag{3.23}$$

The EKF uses these expressions as follows:

- ***Prediction***

$$\hat{\mathbf{x}}_{t|t-1} = \mathbf{a}(\hat{\mathbf{x}}_{t-1|t-1}, \mathbf{u}_t, t) \tag{3.24}$$

$$\mathbf{P}_{t|t-1} = \nabla \mathbf{A}_{t-1} \mathbf{P}_{t-1|t-1} \nabla \mathbf{A}_{t-1}^{\mathrm{T}} + \mathbf{Q}_{t-1} \tag{3.25}$$

- ***Update***

$$\nu_t = \mathbf{z}_t - \mathbf{h}(\hat{\mathbf{x}}_{t|t-1}) \tag{3.26}$$

$$\mathbf{S_t} = \nabla \mathbf{H}_t \mathbf{P}_{t|t-1} \nabla \mathbf{H}_t^T + \mathbf{R}_t \tag{3.27}$$

$$\mathbf{K}_t = \mathbf{P}_{t|t-1} \nabla \mathbf{H}_t^{\mathrm{T}} \mathbf{S_t}^{-1} \tag{3.28}$$

$$\hat{\mathbf{x}}_{t|t} = \hat{\mathbf{x}}_{t|t-1} + \mathbf{K}_t \nu_t \tag{3.29}$$

$$\mathbf{P}_{t|t} = (\mathbf{I} - \mathbf{K}_t \nabla \mathbf{H}_t) \mathbf{P}_{t|t-1} \tag{3.30}$$

As can be seen from (3.24-3.30), the main difference between the EKF and the linear KF is the way the nonlinear system equations are linearized.

3.2.4 Particle Filter

The particle filter (PF) is a Monte Carlo algorithm that can estimate the internal state of a dynamic system by using Bayesian statistical inference [55]. While the KF performs optimally with Gaussian distributed variables, the PF can handle nonlinearity and non-Gaussian noise. The motivation behind the PF is straightforward: generate many candidate solutions, and choose the ones with the highest probability.

The candidate solutions (the state of the agent) are represented with weighted particles. As the number of particles goes to infinity, the accuracy of estimation and the number of particles are proportional.

- ***Initialization:*** Generate a set of weighted particles $\{(w_t^{(i)}, x_t^{(i)}) \,:\, i = 1, \ldots, N\}$, where N is the number of particles, $x_t^{(i)}$ represent particle i, and $w_t^{(i)}$ is the particle weight, such that $x_0^{(i)}$ is drawn from a prior distribution $x_0^{(i)} \sim p(\mathbf{x}_0)$, and the weights of particles are equal, $w_0^{(i)} = \frac{1}{N}$.

- ***Prediction:*** Propagate each particle through the state transition equation:

$$x_t^{(i)} = a(x_{t-1}^{(i)}, u_t^{(i)}) \tag{3.31}$$

Using the measurement model, update the particle weights:

$$\tilde{w}_t^{(i)} = w_{t-1}^{(i)} p(z_t | x_t^{(i)}) \tag{3.32}$$

Normalize the updated weights:

$$w_t^{(i)} = \frac{\tilde{w}_t^{(i)}}{\sum_{i=1}^{N} \tilde{w}_t^{(i)}} \tag{3.33}$$

The state estimate, $\hat{\mathbf{x}}_t$, is calculated as

$$\hat{\mathbf{x}}_t = \mathbb{E}[\mathbf{x}_t] \approx \sum_{i=1}^{N} x_t^{(i)} w_t^{(i)} \tag{3.34}$$

- ***Resampling:*** Systematic resampling algorithm is used in this step. The goal is to sample the particles uniformly with random offsets.

3.2.5 Discussion on Probabilistic Tracking Filters

The KF is optimal for a linear system with Gaussian noise. The EKF applies local linearization in case of a nonlinear system and/or multimodal noise. In this case, the estimation is sub-optimal. The approximation errors during the calculation of the derivatives may introduce errors that may degrade the filtering performance.

The linearization step in the EKF decreases the uncertainty, although in reality the uncertainty caused by random accelerations or environmental effects is still present. If the system is highly nonlinear, the performance of the EKF may not be sufficient.

The PF, on the other hand, simulates the system by using particles that represent possible state values. The computational complexity of the PF increases as the number of particles increases. However, it does not need a linearization step in the process or measurement steps. The particles converge to a state if there is no motion or measurement as time progresses. As the measurement noise decreases, the particle weights tend to be uniformly distributed. Another problem of the PF is that there is no way of estimating how many particles are needed in a problem. A comparison of the KF and the PF is given in Table 3.1.

Table 3.1: Differences between the KF and the PF.

	Kalman filter	**Particle filter**
Maintains	Mean and covariance	Set of particles
Implements	Predict and update	Predict and update (calculate the likelihood of particles)
Constraints	Gaussian noise, linear system dynamics, and measurement model	Large number of particles required
Advantages	Computationally inexpensive, sub-optimal nonlinear extensions: EKF, unscented KF	No linearization required, can operate with multimodal noise

3.2.6 Extended Kalman Filter SLAM

Simultaneous localization and mapping (SLAM) is a general name given to a suite of algorithms that are used to find the location of an agent, e.g., a robot, as well as building a map of the environment without any prior knowledge of the environment. There are several algorithms involved in solving the SLAM problem.

In this part of the dissertation, we explain the difference between extended Kalman filter (EKF) SLAM and EKF-based localization algorithms. Unlike the localization tasks above, the LED landmark locations are unknown *a priori* for SLAM tasks. The fundamental difference between EKF-localization and EKF-SLAM is the processing of the state and error covariance matrices related to the landmarks [52]. Recall that since each LED has its unique code, the data association is not a problem for measurement matching. Table 3.2 shows the main differences between EKF-SLAM and EKF-localization.

Table 3.2: Differences between EKF-SLAM and EKF-Localization. Table is adopted from [2].

Action	**EKF-SLAM**	**EKF-Localization**
Agent moves	Agent motion	EKF Prediction
A new landmark is detected	Landmark initialization	State augmentation
A known landmark is observed	Map correction	EKF Update

In the EKF-SLAM algorithm, the state of the agent and the map are merged into one larger state vector defined as $\bar{\mathbf{x}} = \begin{bmatrix} \mathbf{x}, & \mathbf{m} \end{bmatrix}$. The time index is dropped for simplicity, and $\mathbf{m} = \begin{bmatrix} \ell_1, & \ldots, \ell_\mathbf{k} \end{bmatrix}$ represents the landmark locations for k landmarks. The new state vector and the covariance matrix are given as

$$\bar{\mathbf{x}} = \begin{bmatrix} \mathbf{x} \\ \mathbf{m} \end{bmatrix} \quad \mathbf{P} = \begin{bmatrix} \mathbf{P_{xx}} & \mathbf{P_{xm}}, \\ \mathbf{P_{mx}} & \mathbf{P_{mm}} \end{bmatrix} \tag{3.35}$$

EKF-SLAM assumes that the initial location of the robot is known, so there is no uncertainty about the robot's initial location with respect to the coordinate system. The landmarks are not moving so their locations are chosen as constant and the state transition matrix is augmented with an identity matrix, $\mathbf{I}$, as a new landmark is observed.

The EKF-SLAM method can be broken down into two main steps, described below, using the same notation as for the EKF above.

- ***Prediction*** step of the EKF-SLAM can be written as

$$\bar{\mathbf{x}}_{t|t-1} = \begin{bmatrix} \nabla \mathbf{A}_{\mathbf{x}_{t-1}} & 0 \\ 0 & \mathbf{I}_k \end{bmatrix} \begin{bmatrix} \mathbf{x}_{t-1} \\ \mathbf{m}_{\mathrm{t}-1} \end{bmatrix} + \begin{bmatrix} \mathbf{u}_t \\ 0 \end{bmatrix} \tag{3.36}$$

$$\mathbf{P}_{t|t-1} = \begin{bmatrix} \nabla \mathbf{A}_{\mathbf{x}_{t-1}} \mathbf{P_{xx}}^{(t-1)} \nabla \mathbf{A}^T_{\mathbf{x}_{t-1}} & \nabla \mathbf{A}_{\mathbf{x}_{t-1}} \mathbf{P_{xm}}^{(t-1)} \\ (\nabla \mathbf{A}_{\mathbf{x}_{t-1}} \mathbf{P_{xm}}^{(t-1)})^T & \mathbf{P_{mm}} \end{bmatrix} \tag{3.37}$$

- ***Update*** step of the EKF-SLAM can be written as follows.

$$\nu_{t+1} = \mathbf{z}_t - \mathbf{h}(\bar{\mathbf{x}}_t, \mathbf{m}_t) \tag{3.38}$$

$$\mathbf{S_t} = \mathbf{H}_t \begin{bmatrix} \mathbf{P_{xx}} & \mathbf{P_{xm}} \\ \mathbf{P_{mx}} & \mathbf{P_{mm}} \end{bmatrix}_t \mathbf{H}_t^T + \mathbf{R}_t \tag{3.39}$$

$$\mathbf{K}_t = \begin{bmatrix} \mathbf{P_{xx}} & \mathbf{P_{xm}} \\ \mathbf{P_{mx}} & \mathbf{P_{mm}} \end{bmatrix}_t \mathbf{H}_t^{\mathrm{T}} \mathbf{S_t}^{-1} \tag{3.40}$$

$$\bar{\mathbf{x}}_{t|t} = \bar{\mathbf{x}}_{t|t-1} + \mathbf{K}_t \nu_t \tag{3.41}$$

$$\mathbf{P}_t = \mathbf{P}_{t|t-1} - \mathbf{K}_t \mathbf{S_t} \mathbf{K}_t^{\mathrm{T}} \tag{3.42}$$

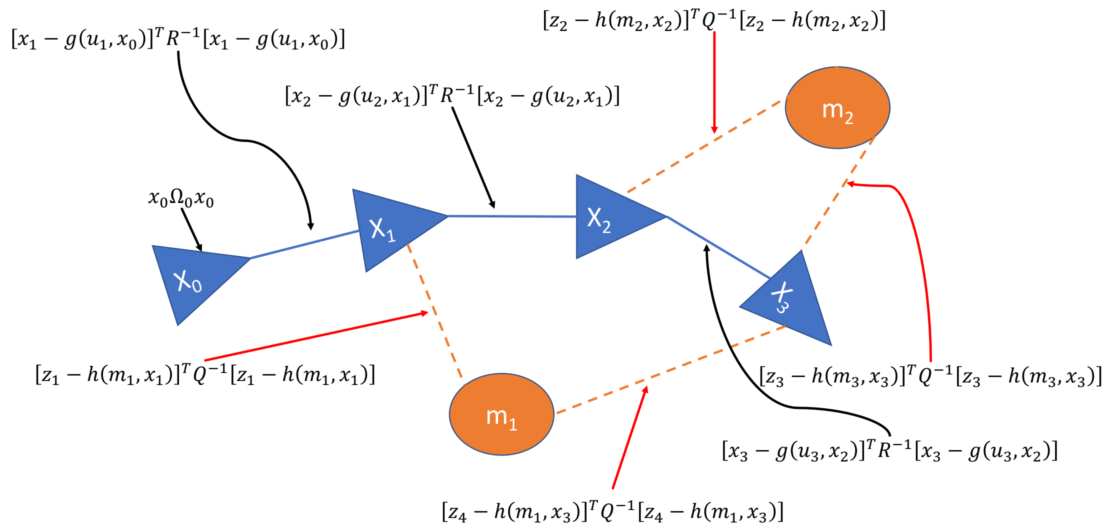

Figure 3.2: Representation of a SLAM problem as a graph.

3.2.7 Graph SLAM

Graph SLAM represents the state of the agent, the landmarks, and the measurements as a graph that consists of nodes and edges [56]. A node represents an agent pose or a landmark location. An edge between two nodes represents a constraint between them. The initial location of the agent, each of the movement of the agent, and observation to the landmarks during the motion are constraints that are used to build a graph. An example is shown in Fig. 3.2 where an agent, represented with a triangle, moves for four times steps and observes two different circular landmarks. The sum of all the constraints in the graph can be written in the form

$$\begin{aligned}\mathbf{J}_{\text{GraphSLAM}} = \mathbf{x}_0^T \mathbf{\Omega_0} \mathbf{x}_0 + \sum_t (\mathbf{x}_t - \mathbf{g}(\mathbf{u}_t, \mathbf{x}_{t-1}))^T \mathbf{R}_t^{-1} (\mathbf{x}_t - \mathbf{g}(\mathbf{u}_t, \mathbf{x}_{t-1})) \\ + \sum_t ((\mathbf{z}_t - \mathbf{h}(\mathbf{m}_t, \mathbf{x}_t))^T \mathbf{Q}_t^{-1} (\mathbf{z}_t - \mathbf{h}(\mathbf{m}_t, \mathbf{x}_t)) \quad (3.43)\end{aligned}$$

where $\mathbf{x}_0^T \mathbf{\Omega_0} \mathbf{x}_0$ is the initial location of the agent with absolute certainty, and $\mathbf{\Omega}$ is the information matrix. Dimensions of $\mathbf{\Omega}$ depend on the number of constraints in the graph. $\mathbf{g}(\cdot)$ is the relative motion with a known control input of the agent, $\mathbf{u}$ is the control input, and $\mathbf{R}$ is the covariance of the process noise. $\mathbf{h}$ is the measurement model, and $\mathbf{Q}$ is the measurement noise. These constraints can be represented as an information matrix, $\mathbf{\Omega}$, and an information vector, ξ as shown in Fig. 3.3. $\mathbf{\Omega}$ keeps a record of the relative robot poses and the observed and unobserved landmarks during the movement of the robot. ξ stores the relative motion of the robot, i.e., the displacement of the robot, and the measurements to the observed landmark. The location of the agent and the map, $\bar{\mathbf{x}}$, can be recovered using

$$\bar{\mathbf{x}} = \mathbf{\Omega}^{-1}\xi. \tag{3.44}$$

3.3 Deterministic Methods for Tracking and Localization

Deterministic localization methods rely on an accurate parameterization of the relationship between the agent and landmark, as well as accurate measurements. In this dissertation, we use a traditional localization method called *multilateration*, and a relatively new approach called *distance geometry*.

3.3.1 Multilateration

The multilateration method relies on estimating the distances between the agent to be localized and at least three landmarks with known locations, as shown in Fig. 3.4. Once this set of locations and distance measurements are known, a least squares solution to localize the agent can be applied [57]. Using more than three landmarks

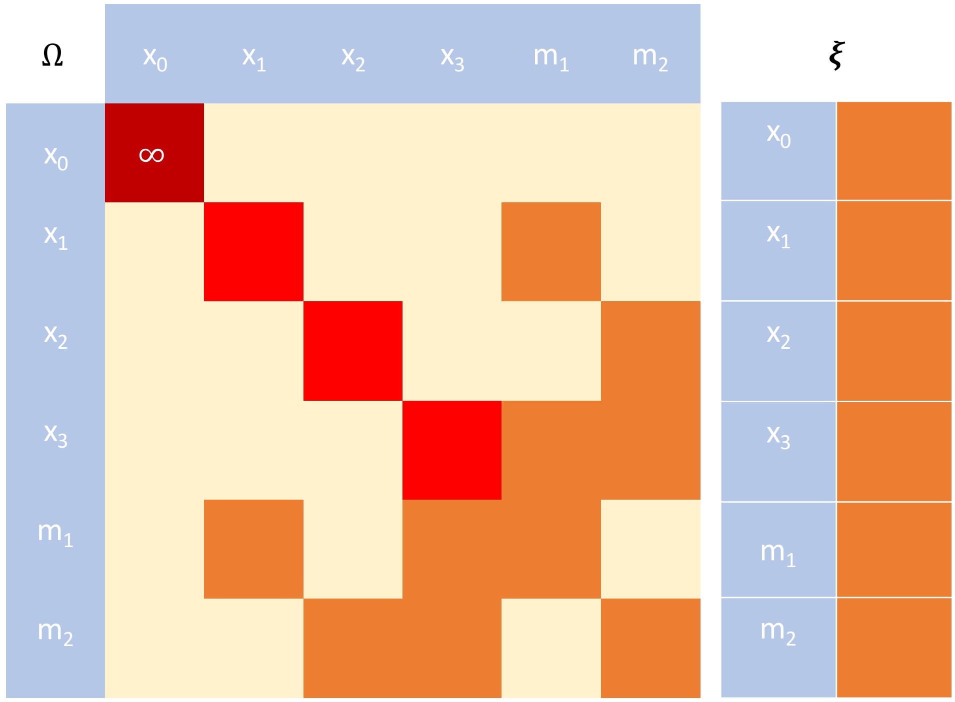

Figure 3.3: Information matrix, $\mathbf{\Omega}$, and the information vector, ξ.

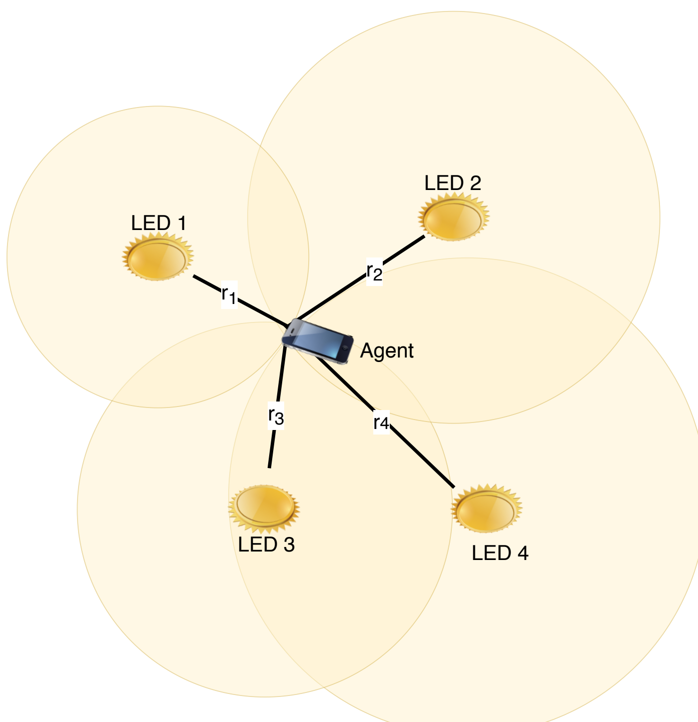

Figure 3.4: Illustration of a multilateration scenario.

increases the robustness of the agent localization.

The solution to the multilateration problem in 2D is straightforward. We start by writing the relationship between the LED landmarks and the agent:

$$\begin{bmatrix} (x_1 - x)^2 + (y_1 - y)^2 \\ (x_2 - x)^2 + (y_2 - y)^2 \\ \vdots \\ (x_k - x)^2 + (y_k - y)^2 \end{bmatrix} = \begin{bmatrix} r_1^2 \\ r_2^2 \\ \vdots \\ r_k^2 \end{bmatrix} \tag{3.45}$$

where $(x_i,\ y_i)$ is the known ith LED landmark location, $(x,\ y)$ is the unknown agent location, and r_i is the distance between the LED landmark and the agent. This distance is obtained from the OWC channel model explained in Section 2.1. (3.45) can be written in the form of $A\mathbf{x} = b$ as follows

$$\underbrace{\begin{bmatrix} 2(x_k - x_1) \ \ 2(y_k - y_2) \\ 2(x_k - x_2) \ \ 2(y_k - y_2) \\ \vdots \\ 2(x_k - x_{k-1}) \ \ 2(y_k - y_{k-1})) \end{bmatrix}}_{A} \underbrace{\begin{bmatrix} r_1^2 - r_k^2 - x_1^2 - y_1^2 + x_k^2 - y_k^2 \\ r_2^2 - r_k^2 - x_2^2 - y_2^2 + x_k^2 - y_k^2 \\ \vdots \\ r_{k-1}^2 - r_k^2 - x_{k-1}^2 - y_{k-1}^2 + x_k^2 - y_k^2 \end{bmatrix}}_{b} \tag{3.46}$$

where k is the number landmarks in the system. The position of the agent can be estimated by $\mathbf{x} = (A^T A)^{-1} A^T b$, which is the least-squares solution.

3.3.2 Distance Geometry

Distance geometry is a method for localizing an agent. It was developed for scenarios where there is no information about landmarks or agent locations, as well as no odometer or inertial measurements. The only assumption is that one of the landmarks is chosen as the anchor, e.g., the point of origin, where other elements are located in relation to the anchor. The information computed is the distance between the landmarks and the agent, which is obtained from RSS measurements [37, 58].

The position of the agent, the LEDs, and inter-landmark distances, r_{mn}, are unknown. The localization algorithm requires at least $3(J+K)-6 \leq (J \times K)$, measurements to avoid being under-determined, where $J \geq 3$ is the total number of LED nodes, and $K \geq 1$ is the number of agents. Fig. 3.5 shows a typical scenario, where an agent measures the distances to three LEDs J, as it moves for $3(J+K)-6$ time steps. The node localization problem can be written in the form $\mathbf{Ax} = \mathbf{b}$ for the scenario given in Fig. 3.5 where $J = 3$ and $K = 1$:

$$\mathbf{x} = \begin{bmatrix} r_{12}^2 + r_{23}^2 - r_{13}^2 \\ \frac{r_{13}^2}{r_{12}^2}(r_{12}^2 + r_{23}^2 - r_{13}^2) \\ \frac{r_{2}^2}{r_{12}^2}(r_{12}^2 + r_{13}^2 - r_{23}^2) \\ \frac{r_{13}^2}{r_{12}^2} \\ \frac{r_{23}^2}{r_{12}^2} \\ r_{13}^2 r_{12}^2 \end{bmatrix}, \ \mathbf{b} = \begin{bmatrix} D_{314} \\ D_{315} \\ D_{316} \\ D_{317} \\ D_{318} \\ D_{319} \end{bmatrix}, \tag{3.47}$$

$$\mathbf{A} = \begin{bmatrix} d_{34}^2 & d_{24}^2 & d_{14}^2 & D_{324}D_{214} & -D_{314}D_{214} & -1 \\ d_{35}^2 & d_{25}^2 & d_{15}^2 & D_{325}D_{215} & -D_{315}D_{215} & -1 \\ \vdots & \vdots & \vdots & \vdots & \vdots & \vdots \\ d_{39}^2 & d_{29}^2 & d_{19}^2 & D_{329}D_{219} & -D_{319}D_{219} & -1 \end{bmatrix},$$

where

$$D_{ijk} = d_{ik}^2 - d_{jk}^2, \ i, j = 1, 2, 3, \ k = 4, 5, \ldots, 9. \tag{3.48}$$

$\mathbf{A}$ and $\mathbf{b}$ contain distance measurements. $\mathbf{x}$ is a matrix of inter-node distances, which

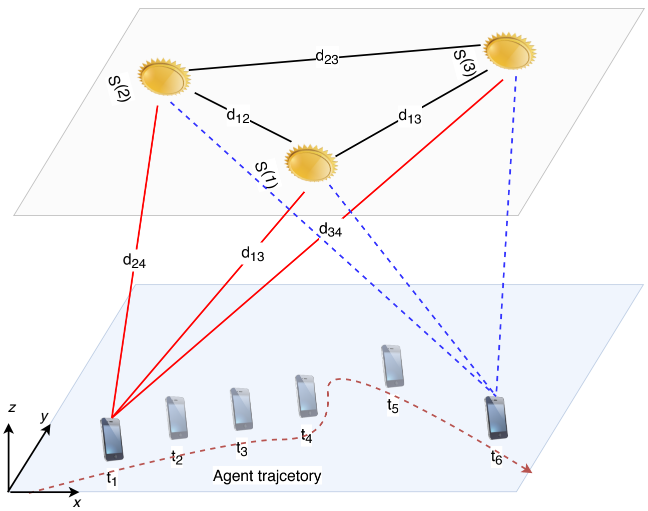

Figure 3.5: Distance geometry: a single agent moves and takes distance measurements for six-time steps. The distances between the LEDs are unknown.

are given as

$$\begin{aligned} r_{12} &= \sqrt{\frac{\frac{\mathbf{x}(2)}{\mathbf{x}(4)} + \frac{\mathbf{x}(3)}{\mathbf{x}(5)}}{2}}, \\ r_{23} &= \sqrt{\frac{\mathbf{x}(1) + \frac{\mathbf{x}(3)}{\mathbf{x}(5)}}{2}}, \\ r_{13} &= \sqrt{\frac{\mathbf{x}(1) + \frac{\mathbf{x}(2)}{\mathbf{x}(4)}}{2}}, \end{aligned} \tag{3.49}$$

where $\mathbf{x}(q)$ is the qth element of $\mathbf{x}$.

Using the inter-node distances obtained, and assuming that the LED nodes are located at $S^{(1)} = (0, 0)$, $S^{(2)} = (x_{S^{(2)}}, 0)$, and $S^{(3)} = (x_{S^{(3)}}, y_{S^{(3)}})$, where x and y are Cartesian coordinates using an arbitrary orientation in 2D, we obtain

$$\begin{aligned} x_{S^{(2)}} &= r_{12}, \\ x_{S^{(3)}} &= \frac{r_{12}^2 + r_{13}^2 - r_{23}^2}{2r_{12}}, \\ y_{S^{(3)}} &= \sqrt{r_{13}^2 - \left(\frac{r_{12}^2+r_{13}^2-r_{23}^2}{2r_{12}}\right)^2}. \end{aligned} \tag{3.50}$$

3.4 Summary

In this chapter, a brief overview of probabilistic and deterministic localization and mapping tools that are used is given. The probabilistic tracking filters described in Section 3.2.3 and 3.2.4 are capable of estimating the state of the agent by forming a relationship between the dynamic model of the motion, the measurements, and the uncertainties in the system. The SLAM algorithms given in Section 3.2.6 and 3.2.7 extends the localization problem to the estimation of a map of the environment where the agent is localized. The multilateration and the distance geometry methods discussed in Section 3.3 can be used to localize an agent or a landmark depending on the application. These methods are studied extensively under the name of *wireless sensor networks.* They can be used in cooperation with SLAM algorithms to initialize a previously unobserved landmark or to locate an agent with respect to other agents. How these methods for indoor localization is discussed in the next chapters.

Chapter 4

Fingerprint-Based Localization for VLP Systems

In this chapter, an indoor localization and tracking approach that uses the optical RSS and probabilistic tracking filters is proposed. The system relies on prior knowledge of the expected optical power intensity throughout the indoor space. We also propose solutions on how to collect, build, and maintain this database of optical RSS measurements, also known as fingerprint map.

Previous research efforts have considered VLC fingerprint-based positioning. Fingerprint methods require a matching process where a measured quantity is assigned to a position by looking up the possible position in the fingerprint map. A detailed discussion of VLP fingerprint-based techniques is given in [59]. RSS-based fingerprint maps are used with the EKF and the PF in [19, 60, 61]. k-nearest neighbors (k-NN) and correlation are used for positioning and tracking using fingerprints in [62]. In [34], an uplink VLP that uses diffuse components is proposed.

The research tasks in this chapter are given in Fig. 4.1. The main contributions of this chapter can be summarized as follows.

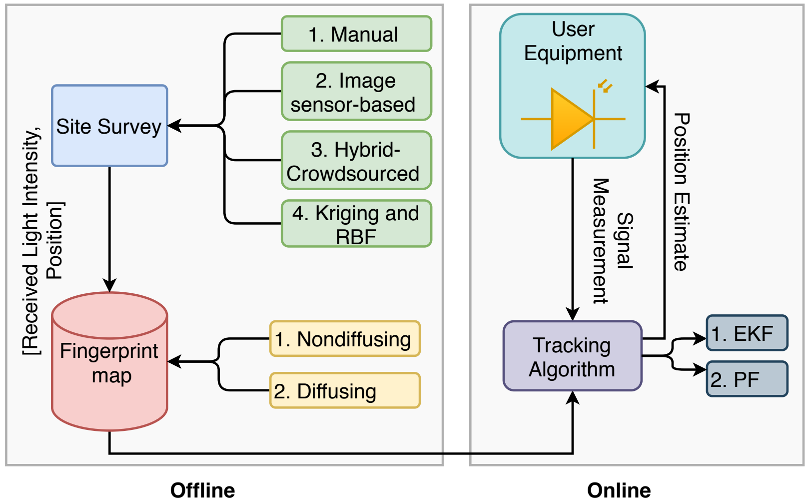

Figure 4.1: Overview of the completed research on VLP fingerprint localization.

The use of fingerprint map: The difference between our work and previous approaches is in the way we define the measurement equation for the tracking algorithm: we measure the RSS directly, and apply a finite difference method to calculate the Jacobian of the RSS measurements using the fingerprint map in the EKF update step, assuming that a database of expected power distribution in the room is provided to the users prior to tracking. Previous studies assume to know the orientation of the transmitter and receiver to recover the channel model and calculate the derivatives in the EKF. The fingerprint map is used similarly in the PF approach. The particles are used to simulate the agent state, and the corresponding measurement at particle locations are used to calculate the likelihood of the online measurement.

The investigation of fingerprint errors: The combined effects of LOS, NLOS, and shadowing unbeknownst to the fingerprint database system on probabilistic filtering methods have not been examined in the VLC-based literature. The results show that variations in the SNR of a particular lamp do not affect the accuracy dramatically, unlike for multilateration.

The fingerprint collection: Another key contribution of this chapter is to propose solutions to reduce the complexity of conducting the site survey. Site survey is defined as the process in which the optical RSS is collected, updated, and maintained to keep an up-to-date fingerprint map. We also show that the fingerprint maps obtained from the proposed site survey methods can be used for indoor positioning and tracking.

4.1 Indoor Localization Using VLC Fingerprints

A fingerprint is defined as a measurable quantity at a known location, e.g., the height of a hill with known coordinates. A fingerprint localization method consists of two steps: the offline data collection step and the online measurement and localization step.

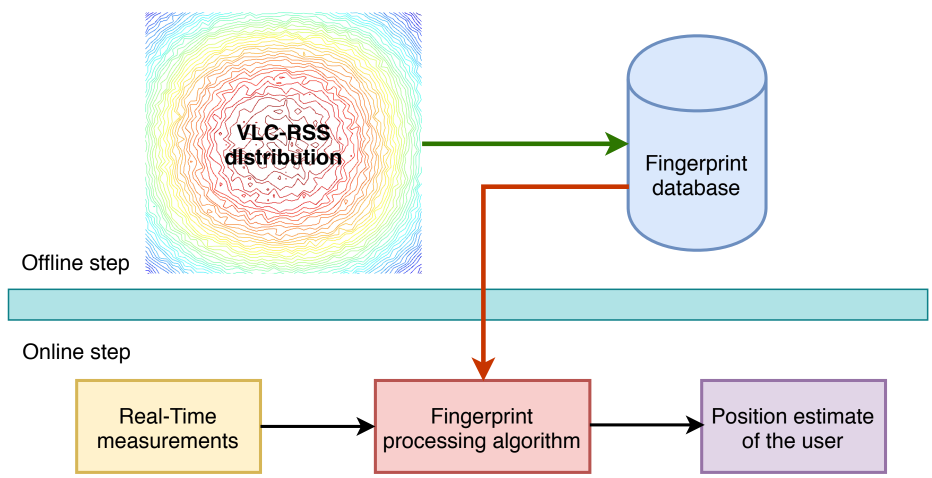

Figure 4.2: Step-by-step VLC fingerprint localization.

Fig. 4.2 illustrates our positioning method. The fingerprint database of RSS values in the room is collected in an off-line phase, prior to tracking. The physical area of the rectangular room at the height of a typical receiver is divided into a $K \times J$ grid. The expected RSS from lamp m at grid point (i, j) is denoted as $P_{ij}^{(m)}$, where $i = 1, \ldots, K$, $j = 1, \ldots, J$, and $m = 1, \ldots, M$. The spatial resolution of the grid is denoted by Δx

and Δy in Cartesian coordinates. The resulting lengths of the orthogonal walls of the room are $K \times \Delta x$ and $J \times \Delta y$. The grid resolution can be chosen depending on the positioning accuracy requirements [19, 61, 63].

The received power levels at the mobile receiver from the various lamps, used as the only real-time measurements for the algorithm, and the power distribution in the room are combined in the online phase using a probabilistic tracking filter. Next, we discuss how the fingerprint map and probabilistic tracking filters are used.

4.1.1 Role of Fingerprint Maps in Probabilistic Tracking Filters

As discussed in Section 1.2, one of the goals this dissertation is to achieve high accuracy positioning using the optical RSS measurements. The RSS measurements by themselves do not give the location of the agent. We convert the optical RSS measurements to the physical location using the probabilistic tracking filters instead. We use probabilistic tracking filters to translate the online optical RSS measurements to the agent's location by employing a database of RSS measurements.

As described in Section 3.2.3, the EKF relies on calculating the Jacobian of the measurements in the system. Equations (2.3) and (2.4) are highly nonlinear functions that depend on the irradiance angle φ and incidence angle ϕ of the light. Calculating and incorporating these angles is difficult since it is impossible to measure them for each optical RSS measurement. Recall that a single PD is used as the sensor. Instead, we use the fingerprint map to calculate the Jacobian, $\nabla \mathbf{H}$. The optical power distribution stored as a fingerprint map is used to compute the Jacobian as shown in Fig. 4.3 (a). First, the predicted agent position is calculated using (3.23). The four adjacent optical RSS values of the predicted position in the fingerprint map are obtained through the fingerprint map. Using a finite difference method, the

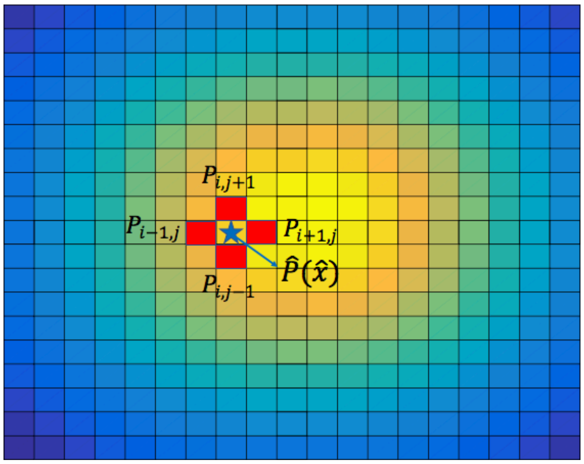

(a)

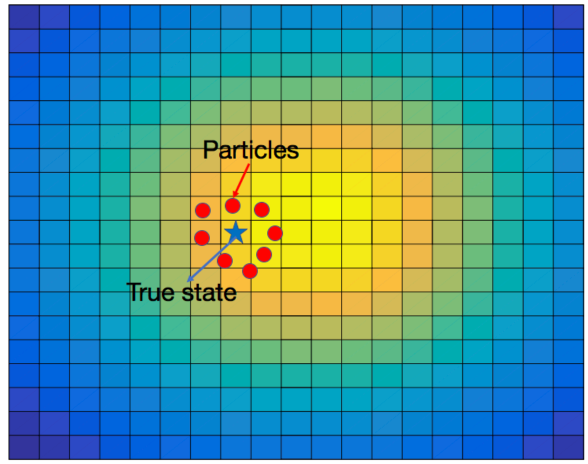

(b)

Figure 4.3: Use of fingerprint map in probabilistic tracking filters. (a) A finite difference method based linearization for the EKF, (b) Simulation of particles for the PF.

derivatives are calculated to linearize the measurements as [19]

$$\nabla \mathbf{H}_{\mathbf{x}_t} \approx \left[\frac{P_{(i+1,j)} - P_{(i-1,j)}}{2\Delta x} \quad \frac{P_{(i,j+1)} - P_{(i,j-1)}}{2\Delta y} \right], \tag{4.1}$$

where $P(\cdot)$ represents the optical RSS at the adjacent cardinal points. $\Delta x = \Delta y$ represent the granularity of the fingerprint map. These values can be chosen depending on accuracy requirements.

Fig. 4.3 (b) represents how the fingerprint database and the PF can be used together. The PF simulates the system using particles [55]. The particles are propagated through the state dynamic model, and the fingerprint database is used as a look-up table for the particles. The likelihood of the particles and the online measurement is calculated as discussed in Section 3.2.4. Each particle has a weight, and the purpose is to pick the particles with the highest weights to estimate the state of the agent [60].

4.1.2 From Optical RSS to Range for VLC Multilateration

In VLC-multilateration, the measurements are the optical RSS received from at least three LED landmarks at known locations. The deterministic nature of the light propagation makes it easy to estimate the range between the LED landmark and the agent under the LOS conditions. Assuming that the LED and the PD sensor on the agent are parallel to each other, the distance, d_i, between the ith LED and the agent can be estimated by modifying (2.3) accurately as follows

$$P_{\mathrm{R}}^{(i)} = P_{\mathrm{T}}^{(i)} \frac{(m+1)}{2\pi d^2} \cos^m(\phi) \cos(\varphi) A_r \tag{4.2}$$

$$d_i = \sqrt{\frac{(m+1) A_r \cos^m(\phi) \cos(\varphi) P_{\mathrm{T}}^{(i)}}{2\pi P_{\mathrm{R}}^{(i)}}} \tag{4.3}$$

The agent location can be estimated using the least squares solution explained in Section 3.3.1.

Fig. 4.4 shows how susceptible the VLC-multilateration is to noise. Even at moderate ($25 - 40$ dB) VLC-SNR values, the mean of the positioning error, μ, is 15 to 25 centimeters. In the next section, we compare the VLC-multilateration with fingerprint-based localization.

4.1.3 Simulation Results for Fingerprint-Based Indoor Localization

One of the key assumptions for the set of results shown in this section is that we are given perfect fingerprint maps that consist of the optical RSS for nondiffusing and diffusing lamps introduced in Section 2.2. We investigate the relationship between the RMSE and the fingerprint map resolution. We use two different resolutions: $\Delta x = \Delta y = 1$ decimeter (dm) and 1 centimeter (cm). We also test the performance of

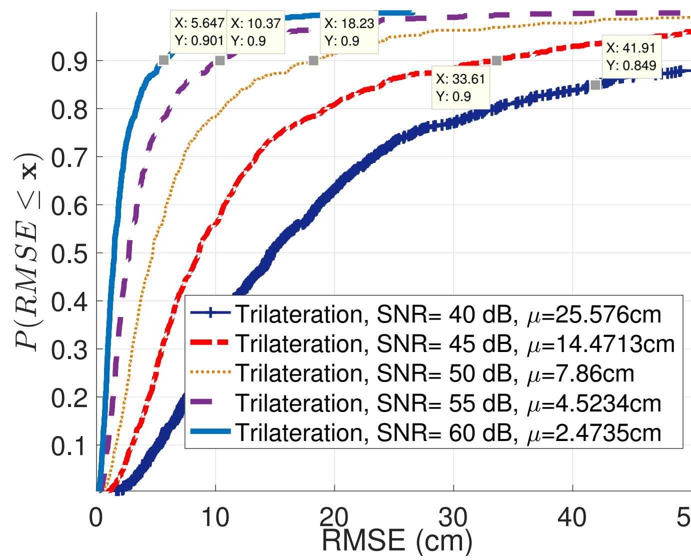

Figure 4.4: Cumulative distribution function of VLC-multilateration error for various VLC-SNR levels for a 3 LED lamp scenario.

the EKF on two test trajectories obtained using the constant velocity model described in Section 3.1. The performance metric used to evaluate the algorithm is the root mean square error (RMSE) between the estimated and the true positions of the mobile agent. Both light dimming and the uncertainties mentioned in Section 2.3 are modeled as different SNR levels. Some key parameters used in the simulation for the results in this chapter are given in Table 4.1.

Table 4.1: Simulation parameters used in this chapter

Parameter	Value
Room dimensions (L × W × H)	$5 \times 5 \times 3$ m^3
Transmitted power per lamp	20 Watts
Lambertian mode	1
LED bulb elevation and azimuth	$-90°$ and $0°$
Lamp position (x, y, z)	(1.25, 1.25, 3) m (3.75, 1.25, 3) m (3.75, 3.75, 3) m (1.25, 3.75, 3) m
PD height	0.75 m
PD field of view	70°
PD aperture	1 mm^2
PD elevation and azimuth	90° and 0°
Room reflection coefficient	0.8
Standard deviation of the random irradiation angles for diffusing lamp	40°
Section 4.3.2	
Image sensor lens aperture	$f/2.2$
Image sensor focal length	29 mm
Image sensor field of view	73.4°
Section 4.3.3	
Wi-Fi APs positions	(1, 1, 1.5) m (5, 1, 1.5) m (5, 5, 1.5) m
Wi-Fi transmitted power (P_t)	40 mW
Reference distance (d_0) m	1 m

A comparison of the fingerprint-based EKF method and the multilateration method proposed in [17] is shown in Fig. 4.5 (a). The EKF method performs better than VLC-multilateration for low SNR values. The performance of the deterministic 25-LED lamp with the EKF and the multilateration method can be compared, but a fair comparison for the diffusing lamp cannot be made. The irradiance and incidence angles are required for the multilateration method and recall that random power distributions affect the performance of VLC-multilateration. We also compare the performance of a single LED lamp with the 25-LED lamp. The results show that when the

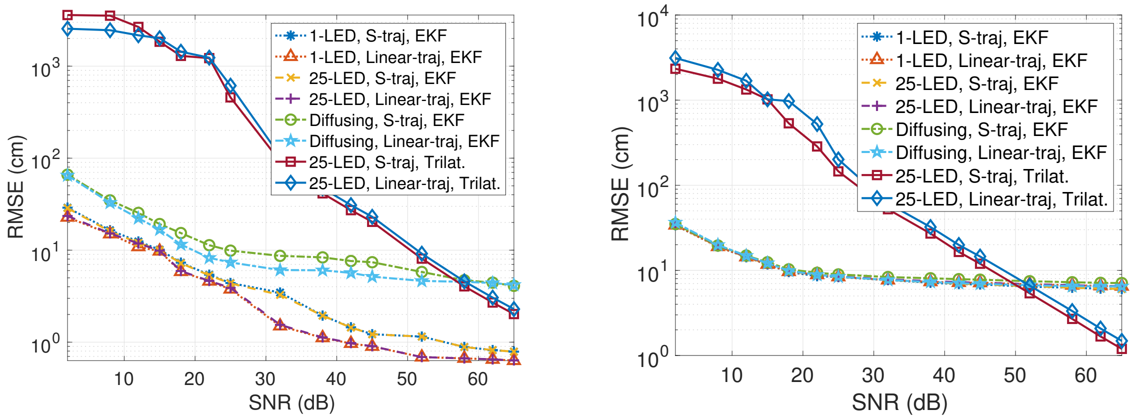

(a) (b)

Figure 4.5: Tracking performance of the EKF using a perfect fingerprint map. Performance comparison of the proposed method and multilateration method when the grid area is (a) 1 cm^2, (b) 10 cm ^{2}.

LED semiangle is large, the tracking performance is close because the power maps of the 25-LED lamp and single LED lamp are similar.

Fig. 4.5 (b) shows a comparison of the multilateration and the EKF methods when the grid area is 1 dm^2 instead of 1 cm^2 used in the results above. We observe that the positioning performance is similar when the 25-LED and the diffusing lamps are compared. The positioning accuracy is limited by the quantization error, yielding almost identical results for the diffusing lamp model and the 25-LED lamp. As the grid size increases, the number of power samples decreases, and the accuracy of the Jacobian of $\mathbf{h}(\cdot)$ reduces. When the SNR is high, multilateration performs better because it does not depend on the motion model and is not affected by the quantization error on the power map. The same conclusion holds for the tracking performance for a single LED lamp and a 25-LED lamp.

Fig. 4.6 (a) shows the tracking performance when the fingerprint map contains both the LOS and the NLOS components of light. It shows that the PF outperforms the EKF for both map resolutions. The linearization step in the EKF may

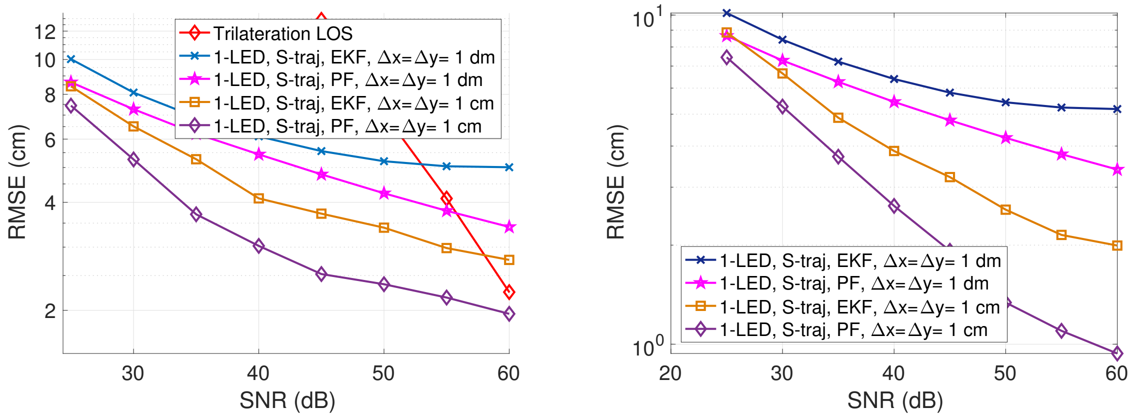

(a) (b)

Figure 4.6: Comparison of different localization methods and effect of grid granularity: (a) Tracking performance of EKF vs. PF vs. VLC-multilateration, (b) RMSE between the nearest tracking grid point and the nearest true trajectory grid point.

sometimes lead to miscalculation and introduce error [51]. The PF does not require the linearization step; instead, it simulates the candidate representations (particles) and looks at the likelihoods of the currently measured power level and the recorded power levels at the positions of the particles. In other words, the PF deals better with the nonlinearities than the EKF. Fig. 4.6 (a) also compares the performance of the RSS-multilateration algorithm versus our proposed Bayesian algorithms. We plot the results starting at the lowest SNR values used in [17]. The performance of the multilateration algorithm is highly sensitive to noise. When solving the multilateration problem, an accurate calculation of the distance between the transmitter and the receiver is needed. Noise in the system or even slight shadowing increases the error of the multilateration dramatically. At higher SNR values, our techniques measure only quantization error due to the grid.

To isolate the tracking errors due to just noise (without quantization errors), Fig. 4.6 (b) shows the RMSE between the quantized positions for both the position estimates and the measurements, which correspond to grid points. The results are as expected, i.e., the error decreases as the SNR increases. The PF again outperforms the EKF.

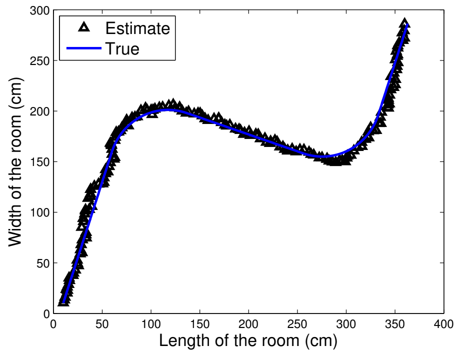

(a)

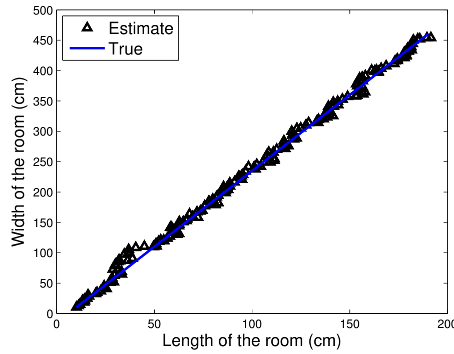

(b)

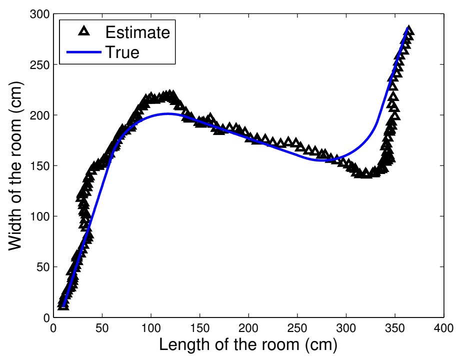

(c)

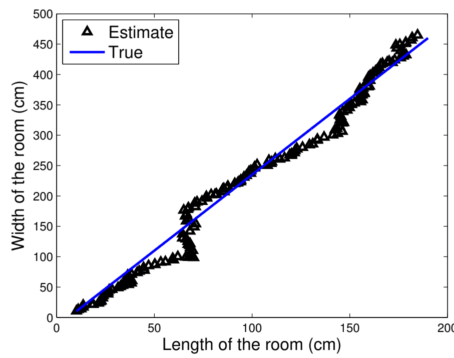

(d)

Figure 4.7: Different test trajectories and lamp types at VLC-SNR=45 dB.(a) Nondiffusing LED lamp, S-shaped trajectory, (b) Nondiffusing LED lamp, linear trajectory, (c) Diffusing LED lamp, S-shaped trajectory, (d) Diffusing LED lamp, linear trajectory.

Figs. 4.7 (a) and 4.7 (c) show example tracking results for nondiffusing and diffusing 25-LED lamp model for an S-shaped target trajectory, respectively. The positioning error for the constant velocity target shown in Fig. 4.7 (b) and (c) is higher than for the S-shaped motion; the straight motion is subject to lower average SNR because it is more often further from the LEDs.

4.2 Effects of Unknown Shadowing on Fingerprint VLP

In general, fingerprint databases are collected for identical lamps under the same conditions. However, different lamps may be affected by unknown shadowing in the system, i.e., unforeseen obstructions in the LOS that may lead to varying SNR levels for each lamp in real-time operation. Shadowing is considered catastrophic for most VLC and VLP systems. In this section, the effect of shadowing on fingerprint-based VLP tracking systems is discussed. The agent receives lower power from one of the lamps than what is expected as shown in Fig. 4.8. We model the shadowing as an additional path loss factor, α, on one of the four lamps [64].

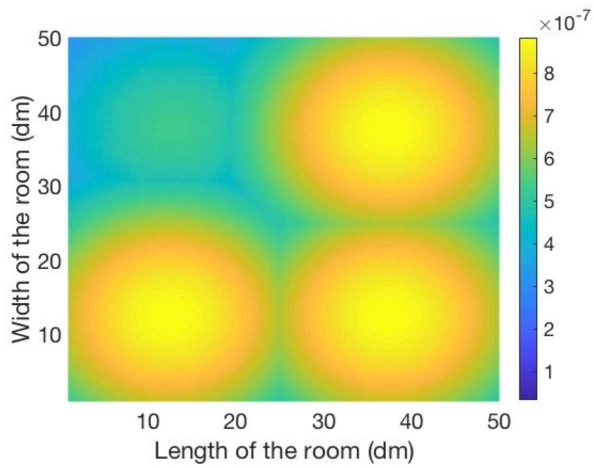

Figure 4.8: Optical intensity distribution in a scenario where one of the lamps has shadowing unbeknownst to the user.

A fingerprint map that is not updated over time does not have information about fluctuations in the optical intensity distribution or error caused by faulty lamps. We investigate this case and compare the performance of the Bayesian filters with the multilateration methods.

Fig. 4.9 (a) shows the effect of shadowing on the performance of the EKF and the

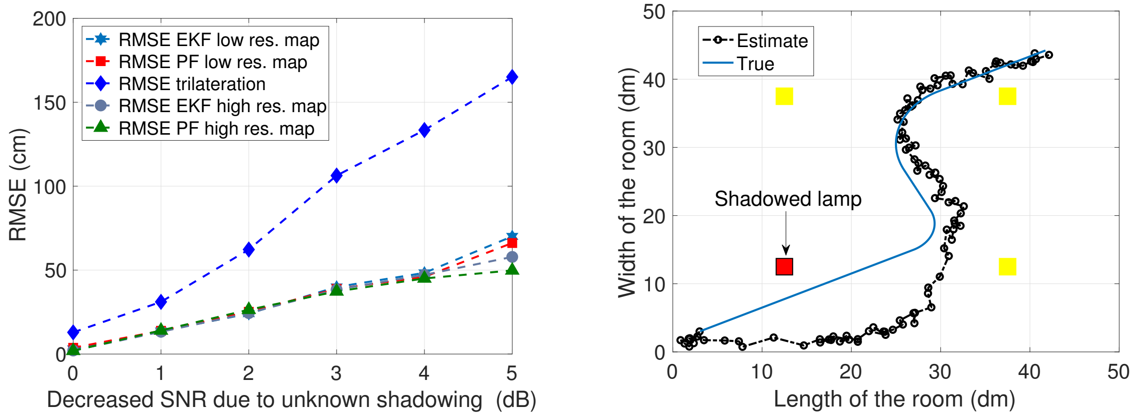

(a) (b)

Figure 4.9: Effect of shadowing on tracking performance: (a) RMSE of position estimate for different shadowing loss levels, $SNR = 45$ dB, and (b) sample tracking using the EKF result when one lamp has unknown shadowing with a loss of 3 dB.

PF systems described above. As a comparison benchmark, the performance of the multilateration algorithm is included using the same parameters as the EKF and the PF algorithms. In this figure, we assume that the shadowing degrades the received SNR, measured as a dB loss. Only one of the four lamps in the room has an unknown shadowing loss, and the rest of the lamps operate normally at 45 dB SNR. From the result, the multilateration algorithm is significantly affected by the shadowing, as expected. However, the EKF and PF using the fingerprint map are robust to shadowing since the fingerprint database is collected in advance.

Fig. 4.9 (b) shows a typical scenario where the EKF is used for tracking an S-shaped user's trajectory. In this experiment, the unknown shadowing for the labeled LED lamp creates a bias in the estimated trajectory, especially if the user is close to that lamp. The effect of the shadowed lamp on the tracking error reduces as the user moves away.

4.3 Fingerprint Database Collection Methods for Indoor VLP

Fingerprinting-based algorithms have several advantages when compared to multilateration-multiangulation and proximity methods, such as fingerprinting does not require time synchronization [65], knowledge of the transmitted power or geometry between the source and the receiver [17], and can operate when there is shadowing in the system [60]. The disadvantage of a fingerprint VLP system is the necessity of a site survey, where the fingerprints are collected before the tracking, and updated over time as the room conditions change over time. The site survey requires precise measurements, which is an error-prone, time-consuming process, and needs to be updated as the fingerprint data changes. Fast temporal changes caused by people moving, background illumination, and random diffusion of signals can make the fingerprint map inaccurate as time progresses. The quality of the fingerprint map directly affects the positioning accuracy.

In this section, we introduce efficient solutions to reduce the complexity of conducting the site survey, and show that the fingerprint maps obtained from the proposed site survey methods can be used for indoor positioning and tracking. Although the site survey problem is well-studied in wireless communications (under the name of radio map building) [29, 66–68], in VLC fingerprint-based indoor positioning studies, the fingerprint map, which consists of the optical measured with the PDs, is assumed to be collected manually [19, 31, 34, 60, 69, 70]. We tackle the site survey with three different approaches to reduce the workload of building the fingerprint map. We test the performance of the simplified/automated site survey methods with nondiffusing and diffusing LED lamp models. We also test the performance of the probabilistic tracking filters to show the effect of the built fingerprint map inaccuracy on the positioning error. The EKF and the PF use the real-time measurements from the PD of the agent and the generated fingerprint maps.

4.3.1 Manual Site Survey with Spatial Interpolation

A manual site survey is defined as the collection of the RSS by someone or some agent that is tasked to measure the RSS in a predefined grid at a fixed height in the room in the offline step. In this section, spatial interpolation methods, which are used in geological sciences to map a terrain [71], are used to estimate the fingerprint map. The goal of using interpolation is to reduce the number of offline measurements. In reality, sampling the RSS at every grid point (offline measurements) in a room to build a fingerprint map is difficult, as discussed in the introduction; hence, measurements at unsampled locations are estimated using spatial interpolation [71]. We consider two different spatial interpolation methods: ordinary Kriging and radial basis function. Simulation parameters are given in Table 4.1, with only one LED lamp located at $(1.25, 1.25)$ m.

Ordinary Kriging

Ordinary Kriging interpolation provides an estimate at unsampled locations by using the correlation between sampled locations. The ordinary Kriging procedure consists of the following steps: exploratory data analysis, variogram modeling, and creating the surface, as described in detail in [68, 72].

In Fig. 4.10 (a) a uniform sampling scenario is considered, the percentage of samples to entire data is %25. The black dots show the sample locations. Fig. 4.10 (b) shows the variogram. The idea of Kriging is to take into account both the distance and the variation between sampling points. The goal is to minimize the variance and minimize the mean of the prediction error. A variogram shows the distribution of

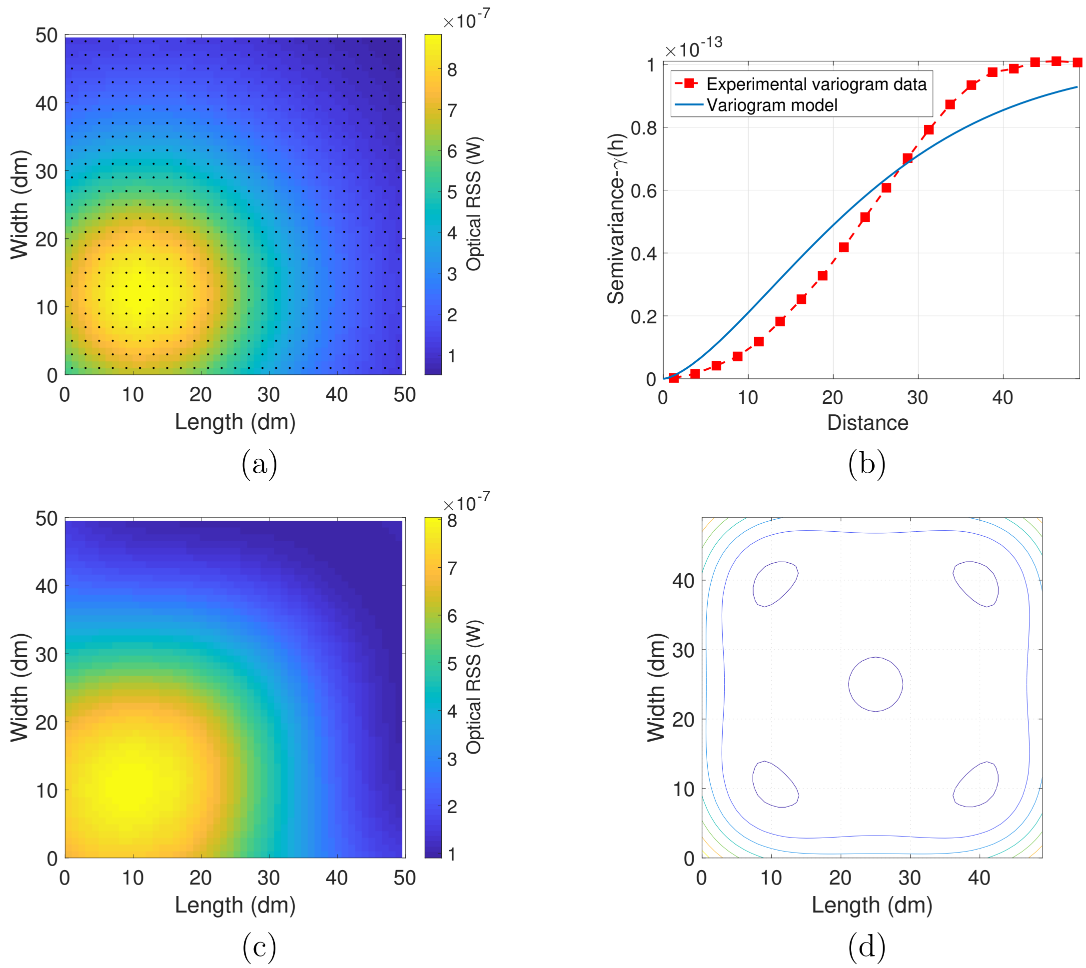

Figure 4.10: Summary of Kriging interpolation method. (a) Sampling, (b) Variogram modeling, (c) Surface construction, and (d) Variance of estimated surface.

variances spatially, and the idea is to pair every sample point with other sample points to calculate the variance. The x-axis shows the distance between sample points, and y-axis is the variance of these points. Fig. 4.10 (c) is the estimated fingerprint map. Fig. 4.10 (d) shows the distribution of the variance over the surveillance area.

Radial basis function

Radial basis function (RBF) interpolation is the second method that we use for estimating the fingerprint map based on a limited number of samples. The RBF ap-

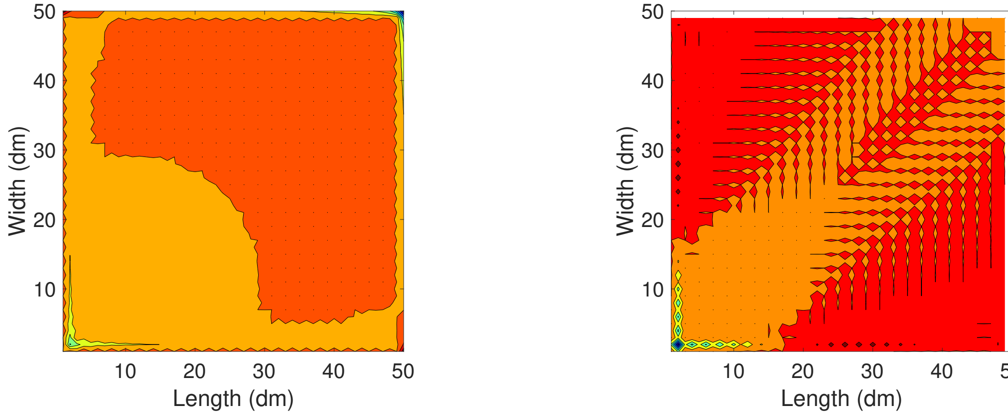

(a) (b)

Figure 4.11: Heat map of (a) RBF interpolation and (b) cubic interpolation

proximates multivariable functions as linear combinations based on a single univariate function [73]. A multiquadratic function is chosen as the kernel for RBF interpolation in this section. The goal of RBF interpolation is to estimate a function in the form of $f(x) = c_0 + c_1 x + \sum_{i=1}^{n} \lambda_i \kappa(|x - x_i|)$, where x_i are the sample locations, and c_0, c_1 and λ_i are the coefficients. $\kappa(|x - x_i|)$ is a multiquadratic function in the form of $\sqrt{1 + \frac{r^2}{\sigma^2}}$, where σ^2 is the variance. Fig. 4.11 compares the performance of RBF and cubic interpolation for the same problem shown in Fig. 4.10. Recall that the probabilistic tracking filters calculate the Jacobian or the likelihood by looking at the fingerprint map. A fingerprint map that has a high variance in the data introduces errors in the estimates.

We envision the use of spatial interpolation methods in two different scenarios. In the first scenario, the PDs used for measuring the optical power (RSS) in the surveillance area are stationary and uniformly distributed with known locations at a typical height for an agent in the room, as shown in Fig. 4.12 (a). In the second scenario, the PDs measure the RSS at known but nonuniformly distributed positions (positioned for measuring convenience), given in Fig. 4.12 (b). The measurements from the PDs are collected and processed by a central processor.

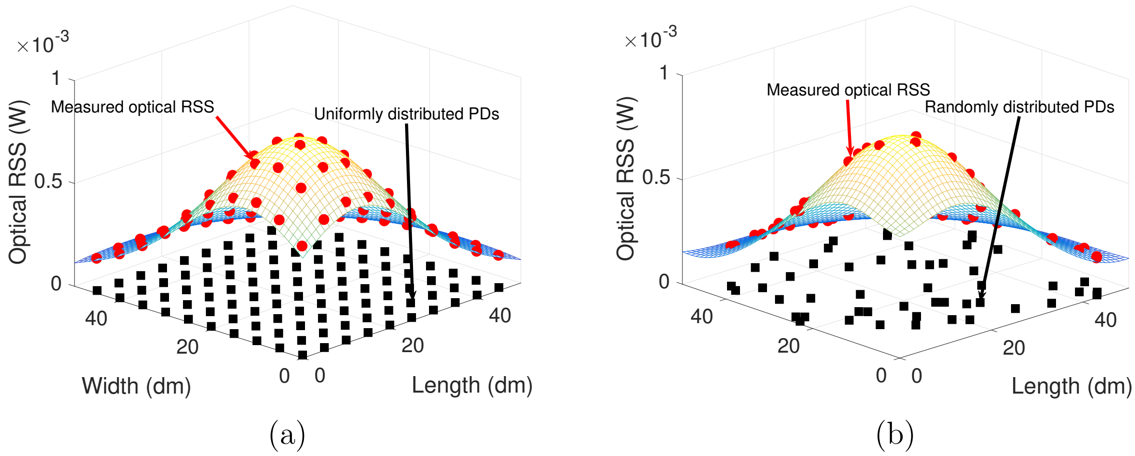

Figure 4.12: Two PD placement setups of the RSS measurements for the spatial interpolation method: (a) uniformly placed PDs, and (b) randomly placed PDs.

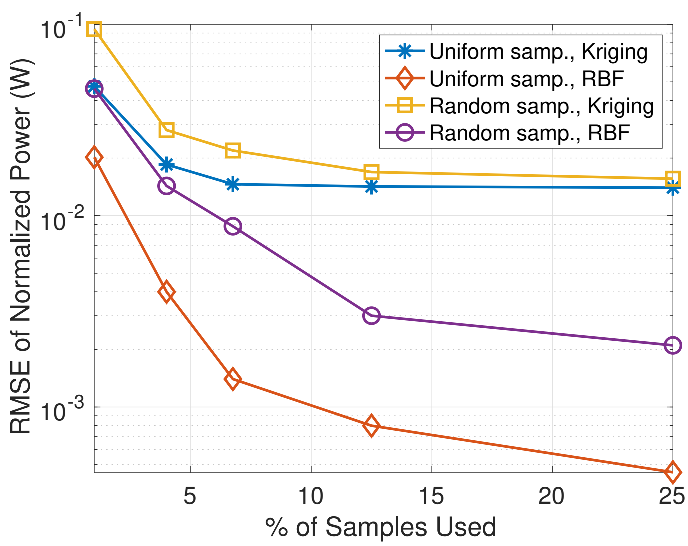

Figure 4.13: Comparison of the RMSE of the normalized power for the fingerprint maps built using spatial interpolation methods with the nondiffusing lamp model; VLC-SNR = 60 dB.

Fig. 4.13 shows a comparison of the root mean square error (RMSE) in creating the power fingerprint map using Kriging and RBF interpolation methods for uniformly and randomly sampled scenarios as shown in Fig. 4.12 for a nondiffusing LED lamp model. The simulation parameters are given in Table 4.1. The performance of the Kriging method saturates after the ratio of used measurements is only 10% of a complete manual site survey for the scenario simulated. The error in the Kriging method reaches a saturation because the technique finds a fit automatically by looking at statistical properties, which stabilize after just a few sample points as discussed in [68, 74]. The RBF performance improves as the number of measurements is increased [75]. For RFF interpolation, uniform sampling significantly outperforms random sampling, as expected for uniform illumination scenarios such as the one tested here.

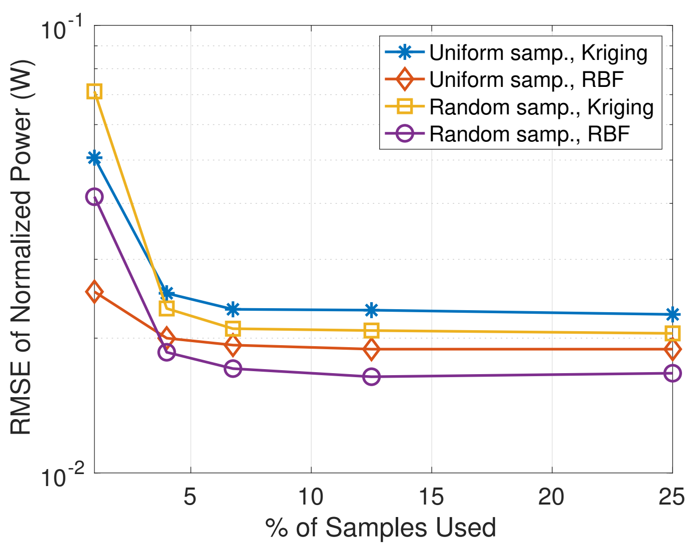

Figure 4.14: Comparison of the RMSE of the normalized power of the fingerprint maps that are built using spatial interpolation methods with the diffusing lamp model; VLC-SNR = 60 dB.

In Fig. 4.14, the same data collection scheme and interpolation methods are tested for the diffusing LED lamp model. The results show that even though the RSS distribution is randomized in the measurement area, we can still build a fingerprint map with an RMSE of less than 2% of the normalized power. Note that, when enough samples are collected, random spatial sampling slightly outperforms uniform sampling when the light distribution is itself nonuniform.

The accuracy of the spatial interpolation methods and which one is more accurate depending on the data [76]. Since in our test the light follows a structured, somewhat smooth distribution, the RBF method performs better than Kriging, as shown in Figs. 4.13 and 4.14. In summary, RBF with uniform sampling has the lowest error among all methods tested. The results show that it is possible to use spatial interpolation as a way of reducing the number of measurements for the manual site survey.

4.3.2 Imaging Sensor-Based Site Survey

In this section, we propose an automated fingerprinting-based algorithm for an indoor tracking system that uses light-emitting diodes (LED) equipped with imaging sensors. The main contribution of this section is to offer a solution to eliminate the manual site survey for fingerprinting. The fingerprint collection part requires a calibration step that consists of the following: (**i**) a theoretic light power distribution is calculated using the visible light communication channel model; (**ii**) the imaging sensors mounted on the LED arrays capture the grayscale images; (**iii**) the captured images and the theoretically calculated light power distribution are used to estimate the light power map.

The reference or *a priori* fingerprint map $\tilde{\mathbf{P}}$ is found theoretically using (2.3) and (2.4) on a grid of size $N \times J$ in the room at a fixed predicted receiver height. The reference fingerprint map is used to estimate the expected power map $\hat{\mathbf{P}}$ in the room.

Each LED array is equipped with a camera, as shown in Fig. 4.15, that is calibrated

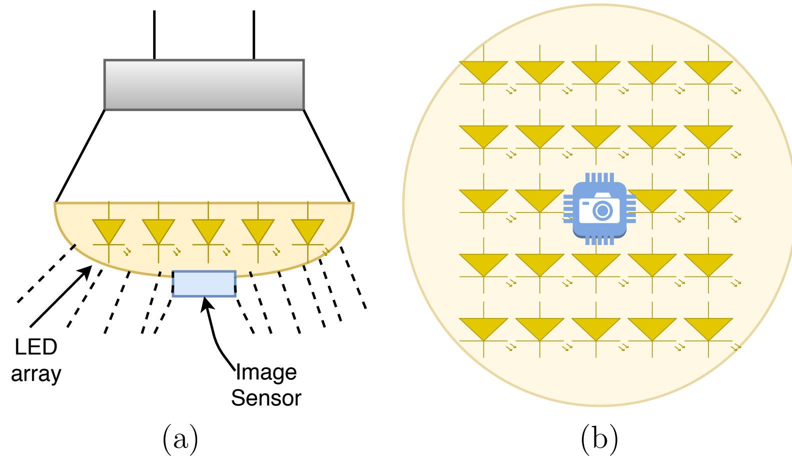

Figure 4.15: LED array equipped with an imaging sensor. (a) Side view. (b) Bottom view.

for the room, and a mapping from the grayscale images, $\mathbf{I}$, to $\hat{\mathbf{P}}$ is found by using $\tilde{\mathbf{P}}$ for the room. The goal is to find an optimal mapping that yields the best $\hat{\mathbf{P}}$ for the particular room. The system is able to decide the best way to update the $\hat{\mathbf{P}}$ by calculating the RMSE between $\tilde{\mathbf{P}}$ and $\hat{\mathbf{P}}$. Therefore, $\tilde{\mathbf{P}}$ is not required when the calibration step is complete. Only the estimated power map, $\hat{\mathbf{P}}$, is provided to the agent. Linear or nonlinear regression, or an artificial neural network is used for mapping from the grayscale pixel values to the light power levels. A PD on the agent measures the light power in real-time.

Imaging Sensor Calibration–Fingerprint Estimation

The imaging sensor is calibrated based on an offline test. We calibrate the camera to an *a priori* power map to estimate $\hat{\mathbf{P}}$ using $\tilde{\mathbf{P}}$ and $\mathbf{I}$. A gamma corrected linear regression, nonlinear curve fitting, or artificial neural network (ANN) based regression method is used to approximate this mapping. Gamma correction helps to find a linear equation for the curve fitting function. Nonlinear regression is used for finding a higher degree polynomial representation without using the gamma correction method. The

ANN is a powerful tool used for function fitting and approximation.

To obtain the most up-to-date estimate of the fingerprint map in the room, images are collected at predefined time intervals. These images are used to predict the newest version of $\hat{\mathbf{P}}$, to replace the stale $\hat{\mathbf{P}}$ in a recursive manner. The optimal update frequency, which is the time intervals chosen to repeat the regression process, depends on the time-varying shadowing, the motion of the users, and changes in the SNR levels.

Gamma Correction Method

Gamma correction, which is a nonlinear stretching function, helps us obtain a uniform grayscale pixel value distribution. It changes the luminance values in a still image [77]. The idea is to use the gamma correction method to find the simplest function for estimating the power from the image, i.e., a line. The dynamic range of the grayscale image is first adjusted to a gamma (γ) value [78]. When the grayscale pixel values of the captured image are plotted versus the light power levels from $\tilde{\mathbf{P}}$ in mW, the distribution may not be exactly a straight line but is approximated using the linear function

$$\hat{\mathbf{P}} = a_1 \mathbf{I}^{\gamma} + a_0. \tag{4.4}$$

$\hat{\mathbf{P}}$ is the estimated power map, $\mathbf{I}$ is the image from the camera, a_0 and a_1 are the coefficients of the linear equation.

Nonlinear Regression Method

In real life, there may be nonlinearities that are not possible to correct using the gamma correction. In such cases, where it is impossible to represent the transformation from the grayscale to the power with a linear function, a high order polynomial is needed for the regression process; the polynomial may be of any order, m, that minimizes the RMSE:

$$\hat{\mathbf{P}} = a_m \mathbf{I}^m + a_{m-1}\mathbf{I}^{m-1} + \cdots + a_1 \mathbf{I}^1 + a_0 \tag{4.5}$$

$a_0, \ldots, a_m$ are the coefficients of the polynomial found through regression.

Artificial Neural Network Method

Artificial neural networks (ANN) are biological-neural-network-like systems that consist of nonlinear equations that work in parallel [79]. Training is used to update the weights of the algorithm during the calculations to decrease the error in estimating the power map. ANNs can be used for curve fitting, especially for nonlinear problems. Depending on the size of the power map, the ANN may be faster than regression methods. The ANN used for this section is a shallow network, consisting of one hidden layer with a sigmoid activation function. The input is the grayscale pixel value from the image $\mathbf{I}$, and the output is the power estimate, $\hat{\mathbf{P}}$.

Numerical Results

We tested the performance of the data fitting methods on two different resolution. The resolution refers to the size of the grid elements ($\Delta x = \Delta y$). In operational mode, we capture the image and use the estimated functional relation to get current $\hat{\mathbf{P}}$. In practice we do this every few minutes, depending on the refresh rate we need. We simulate this by using a 20×20 cm^2 paper and scale to what the room conditions would be. The physical room receiving plane is divided into equal size $N \times J$ grid rectangles.

Fig. 4.16 is a summary of the performance of the fitting methods discussed in this section. The simulation parameters are given in Table 4.1. Fig. 4.16-(a) shows

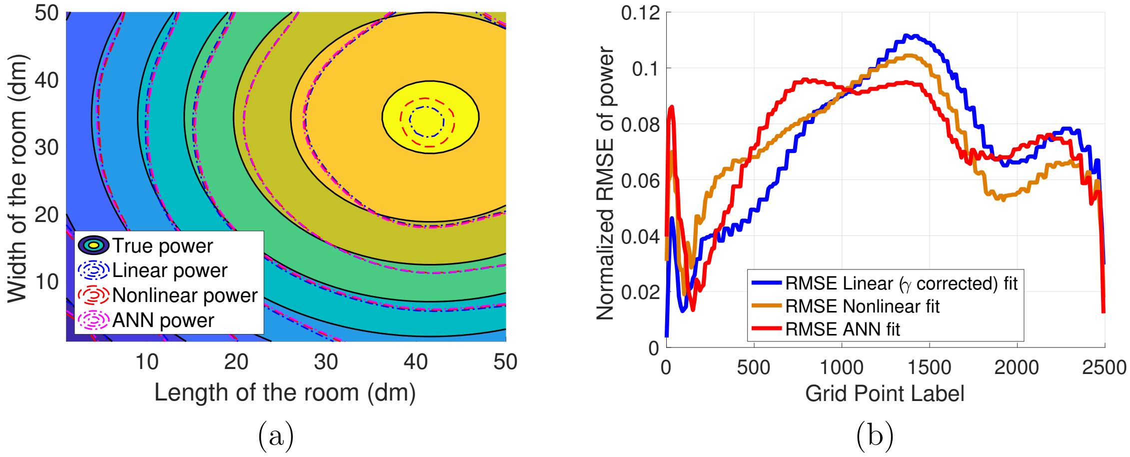

Figure 4.16: Performance of the three different function fitting methods is compared. (a) shows the light power contours when $\Delta x = \Delta y = 1$ dm. (b) is the normalized root mean square error of the methods, normalized to the received power.

the power contours when the image-based site survey is used when $\Delta x = \Delta y = 1$ dm. From Fig. 4.16-(a), we see that there is a bias introduced on each estimated fingerprint map. The bias is a result of calibration error of the images discussed in Section 2.3. The bias affects positioning performance directly. Fig. 4.16-(b) shows the normalized RMSE between the true power and the estimated power of each grid point. The results show that the performances of the three methods yield different normalized RMSE depending on the grid position point for a 50 point by 50 point grid.

We test the performance of the EKF tracking algorithm using the fingerprint map obtained by the camera based method. Fig. 4.17 shows the RMSE for the EKF using one of the different fingerprint maps generated using the algorithms explained in Section 4.3.2. The performance of the true fingerprint map (the true power at every grid point) has the lowest error for both map resolutions, as expected. The interesting point is that the performance of the three image-based methods (linear, nonlinear and ANN) are very similar. This is an expected result as the bias of the three methods is similar, as seen in Fig. 4.16. The higher RMSE errors are due to the errors introduced

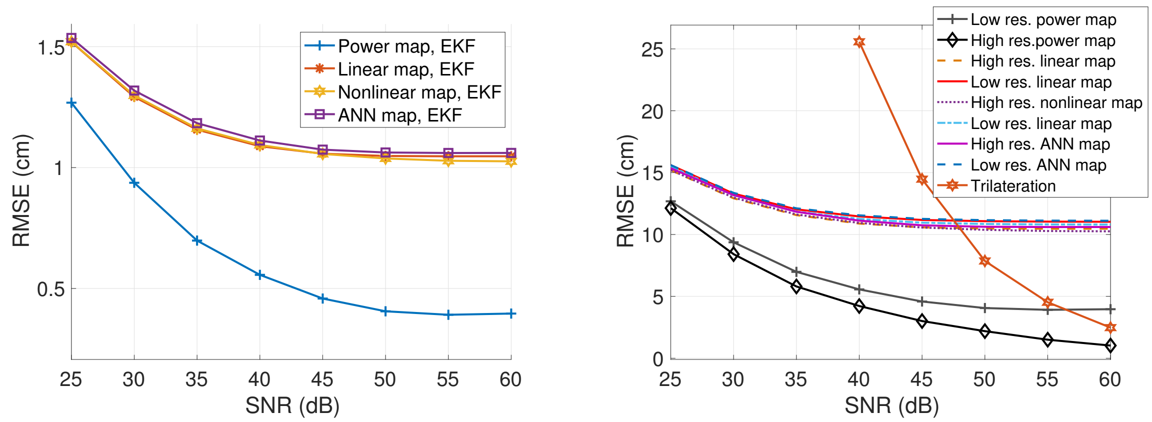

(a) (b)

Figure 4.17: Performance of the three different fingerprint maps and their effect on agent tracking. (a) shows the effect of tracking on the EKF. (b) Multilateration vs. the EKF.

during the image capture process. The fit functions cause information loss during the data fitting process, and it is not possible to fit a function that satisfies the best fit for every pixel value. If attempted, overfitting may occur, which limits the performance and leads to inaccurate mapping from the image pixel values to power levels as the illumination conditions change.

Fig. 4.17 (b) shows a performance comparison between the LED-EKF and the LED-multilateration. The LED-multilateration algorithm's RMSE is not comparable at SNR values below 40 dB. This shows that when the uncertainty noise dominates the system, the LED-multilateration is not accurate, unlike the LED-EKF algorithm.

4.3.3 Hybrid-Crowdsourced Site Survey

For indoor positioning, there are a variety of solutions proposed that utilize ultrasound, Wi-Fi, visible light communications (VLC), etc., as explained in Section 1.1; however, none of them prevails over the other. The solution for creating and updating the fingerprint map we offer in this section uses already deployed systems in the area.

We rely on existing Wi-Fi and LED lighting systems and combine their advantages to enhance positioning accuracy. Wireless RF access points (AP) are present in almost every indoor space, like shopping malls, industrial plants, etc.

We propose a three-step solution. In the first step, the mobile unit uses the Wi-Fi-based multilateration to estimate its rough position. In the second step, the algorithm measures the received light intensity from orthogonally-coded LEDs and assigns them to the position found by Wi-Fi based multilateration. As the user moves, the light intensity measurements are updated. This is called the fingerprint map learning process. The third step is to track the user using an extended Kalman filter (EKF), as described in Section 4.1.1.

Fingerprint Map Learning

In this section, we explain how the fingerprint map is generated. The basic idea is to use the rough location of the user obtained through Wi-Fi multilateration to generate an optical power site survey and use the inherent smoothness expected from optical power distributions to enhance the accuracy of the map.

Wi-Fi Signal Based multilateration

Wi-Fi access points are abundant in our target indoor areas, like shopping malls, industrial facilities, and museums. Multilateration from Wi-Fi-based signals is widely studied in the literature. Wi-Fi-based multilateration relies on accurate estimation of the distance between the transmitter (AP) and the receiver, referred to as the agent (agent). In [36], it is shown that modeling the path loss with the Friis free space propagation model is not accurate. Therefore, we use the following equation given in [36] to model the propagation loss:

$$P_r(d)[\text{dBm}] = P_0(d_0)[\text{dBm}] - 10n_p \log_{10}\left(\frac{d}{d_0}\right) + X_\sigma \tag{4.6}$$

$P_r(d)$ is the RF RSS at a distance d from the transmitter. $P_0(d_0)$ is a known reference power at distance d_0 from the transmitter. n_p is the propagation-environment-dependent path loss exponent, and X_σ is a zero mean normal distributed random variable that models the random effects in the propagation medium with a standard deviation of σ. Given the received power, P_r, the distance between the AP and the receiver, d, can be estimated from (4.6). The unbiased estimate of the distance between the transmitter and the receiver is given in [36] as:

$$\hat{d} = d_0 \left(\frac{P_r}{P_0(d_0)}\right)^{-1/n_p} \exp\left(-\frac{\sigma^2}{2\left(\frac{10}{\ln(10)}\right)^2 n_p^2}\right). \tag{4.7}$$

When the distance between the transmitter and the receiver and the positions of the transmitters are known, the agent positions can be estimated using the least squares method. This method is known as multilateration.

The multilateration method using Wi-Fi signals does not by itself provide accurate position estimation. The estimates will have errors caused by the random effects in the propagation environment; these effects were captured by the random variable X_σ in (4.6). Fig. 4.18 shows the effect of X_σ on the estimated distance in a typical room for one AP. The AP is placed at ($x = 0$ m, $y = 0$ m) in the 5 m $\times$ 5 m room. To do multilateration, at least three APs are needed.

In this section, we propose to use the estimated position from the Wi-Fi multilateration of agents walking in the room to build our site survey. The Wi-Fi multilateration estimates from many users walking in different parts of the room are needed to update

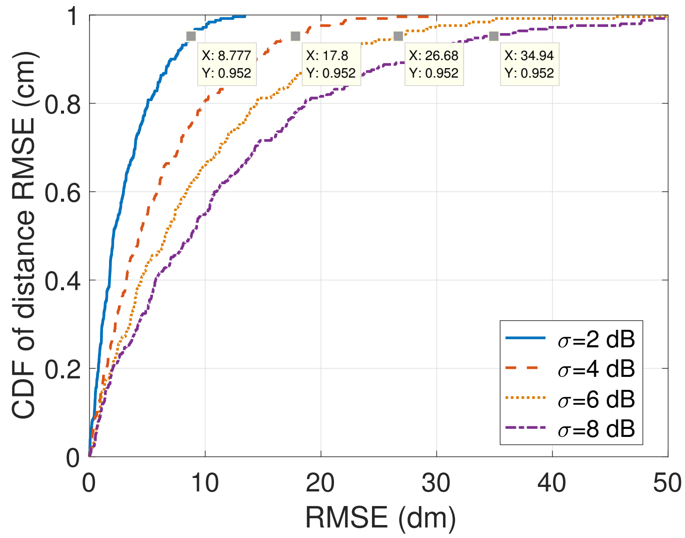

Figure 4.18: Cumulative distribution function of Wi-Fi distance estimation RMSE for various fading levels with respect to a Wi-Fi access point.

the entire fingerprint map. The assumption is that there are N user trajectories, and multilateration is done for all N trajectories. Let the number of sampling points for multilateration for each trajectory in the room be M; this results in a multilateration position estimate matrix of dimensions $N \times M$:

$$\hat{\mathbf{T}} = \begin{bmatrix} (x_{11}, y_{11}) & \dots & (x_{1M}, y_{1M}) \\ (x_{21}, y_{21}) & \dots & (x_{2M}, y_{2M}) \\ \vdots & \vdots & \vdots \\ (x_{N1}, y_{N1}) & \dots & (x_{NM}, y_{NM}) \end{bmatrix}$$

where $(x,\ y)$ represents the Cartesian coordinates. $\hat{\mathbf{T}}$ is used to update the fingerprint map. The received light intensity at the agent's actual position is assigned to the agent's estimated position.

Fingerprint Map Updating

The fingerprint map is a matrix in which the average received power values are stored. The physical area of interest is divided into $K \times J$ rectangles. The matrix of estimated power is denoted by $\mathbf{P} = [P_{ij}]$, where $i = 1, \ldots, K$ and $j = 1, \ldots, J$ are the indices of the Cartesian coordinates. The size of the map is application specific. If high accuracy is needed for sensitive applications, like autonomous robots used in industrial plants, a high-resolution map is needed.

We have examined two approaches of using the multilateration results to generate $\mathbf{P}$. The first is where the initial map is updated sequentially as users walk into the room; the second is to use the matrix $\hat{\mathbf{T}}$ in a batch process. In the first approach, the initial fingerprint map, $\mathbf{P}_0$, is a matrix of zeros with the same dimensions as $\mathbf{P}$. After the first user moves in the surveillance area, four steps are followed:

(i) The position of the agent is found by Wi-Fi multilateration as explained above.

(ii) The received light intensity is measured by the agent at the agent's true position.

(iii) The multilateration positions and measurements are combined: The initial fingerprint map is updated, and is a sparse matrix now; the nonzero values are in the positions found by multilateration. The multilateration introduces positioning errors, which cause a mismatch in the power map. The light intensity measurements will not be assigned to the true positions, but the positions found from multilateration.

(iv) According to (2.3), the light distribution is a smooth function across the room and from the light source to the floor. In this step, the power map data is smoothed to create a smooth surface, which is updated in subsequent iterations. The surface smoothing methodology chosen is to duplicate the nearest non-zero value.

The site survey in the second approach takes longer. In the second approach, we wait until N users have collected multilateration measurements and optical RSS data in the area. The data is used to update and learn the fingerprint map just like in the first approach but in a batch process instead of sequential processing. A linear KF is used to smooth the Wi-Fi multilateration results after step (i) of the first approach. The KF reduces the error between the estimated position and measurements. This also reduces the bias in the final map. The rest of the algorithm is the same as for the first approach.

Once we have an initial surface from one of the approaches described above, the survey map can be used by the EKF as described in Section 4.1.1. However, environments are not static. We envision an adaptive implementation where the power map surface is updated using new crowdsourced data. The mixing rule we use in this work is given as:

$$P_{ij}^{n} = \alpha^{\omega} P_{ij}^{n-1} + (1-\alpha^{\omega})\tilde{P}_{ij}^{n-1} \tag{4.8}$$

P_{ij}^{n} is the updated power values at index ij to be updated from the new trajectory labeled as n. P_{ij}^{N-1} is the power values in the surface from the previous crowdsourcing. $\tilde{P}_{ij}^{N-1}$ is the measured power received from the LEDs at that moment. $\alpha \in (0,\, 1)$ is the learning rate. It decides which one should be trusted more: the previously computed surface or the measurements. ω is the VLC channel coherence, allowing the previous power estimates more or less longevity. As the channel impulse response changes this variable changes. In this dissertation, the VLC channel is chosen as constant, $\omega = 1$.

In the map learning process, the multilateration and light power measurements are done in the agent, then uploaded via Wi-Fi to a central processor. After learning the map $\mathbf{P}$, assuming that the conditions change slowly, the map can be updated based on user-sourced data.

Simulation Results for Hybrid-Crowdsourced Site Survey

We assume that the VLC channel impulse response does not change in this section, for simplicity. The power map is updated in batches. We do not update the map every time a user is introduced, but the system waits until a predefined number of trajectories are available. We assume that α is constant value so that we put equal emphasis on the updated power map values and the real-time measurements.

Wi-Fi multilateration needs at least three APs with known positions. Equations (4.6) and (4.7) are used to estimate the distance between the agent and each of the APs, and the least square solution gives the estimated positions. In the simulations, APs with identical path loss parameters are positioned on three corners of the room.

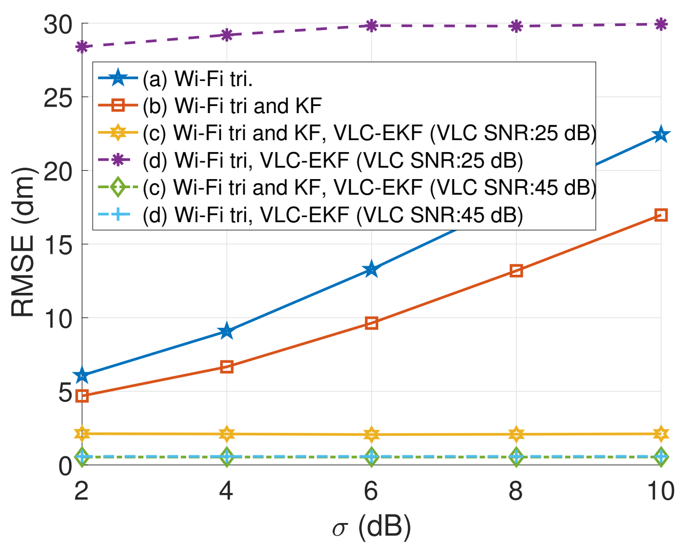

Figure 4.19: Performance of methods (**a**), (**b**), (**c**) and (**d**) are compared as the σ of the random effects in the Wi-Fi propagation medium increases.

Fig. 4.19 gives an overview of the performance of our algorithm using one of four different methods:

(**a**) Wi-Fi multilateration: The distances from the three APs are estimated using

(4.7). The estimated distances are used to solve the multilateration equations.

(**b**) Wi-Fi multilateration and smoothing with a KF: The estimated positions are smoothed using a linear KF.

(**c**) Wi-Fi multilateration, VLC-EKF: The received light intensity powers at the agents' true positions are assigned to the UEs' estimated positions by Wi-Fi multilateration. This step constructs a fingerprint map of the light intensity after smoothing. The fingerprint map is used for EKF-based tracking.

(**d**) Wi-Fi multilateration, KF smoothing, and VLC-EKF: The same as (c); the only difference is the use of a linear KF to smooth the estimates from the Wi-Fi multilateration.

The experiments show that as the random effects in the propagation medium, X_σ, increase, the RMSE increases. The estimates can be more accurate by using a KF on the estimated positions obtained with Wi-Fi multilateration, i.e., the performance of (**c**) is improved in (**d**) by introducing a KF. This is because the KF decreases the error introduced while building $\mathbf{P}$ by smoothing the Wi-Fi multilateration measurements.

In Fig. 4.20 (a), the effect of the number of agent-trajectories and its effect on the tracking accuracy is shown when the method (**c**) is used. Fig. 4.20 (b) shows the number of agent-trajectories needed to create a sufficient and accurate $\mathbf{P}$ that is to be used in the VLC-EKF when the method (**d**) is employed. The agent-trajectories are the source of crowdsourced visible light intensity used to build the map, $\mathbf{P}$. It is clear from the figure that for our particular simulation and room size, after 300 trajectories the performance is indistinguishable. If we compare Figs. 4.20 (a) and (b), we can see that method (**d**) is slightly better than (**c**) in terms of accuracy, especially for lower SNR values like 25 to 30 dB. However, the difference is not significant for moderate to high SNR values.

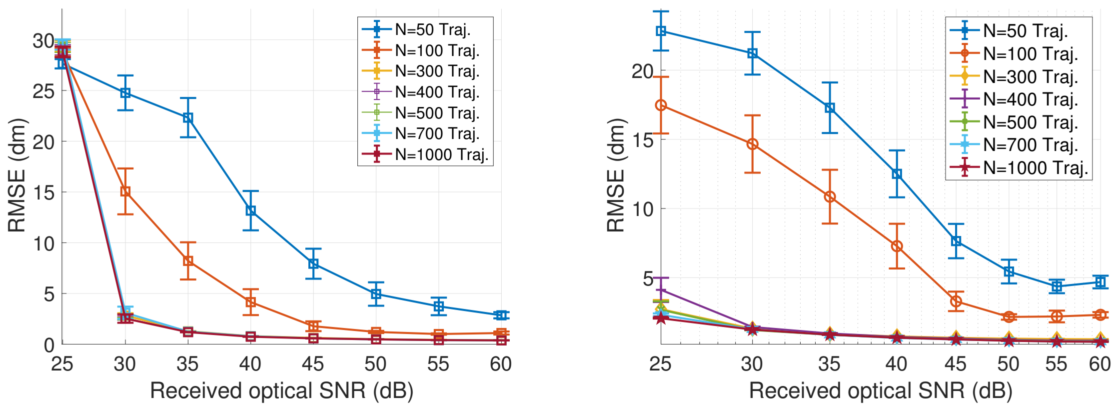

(a) (b)

Figure 4.20: Effect of the number of users on tracking accuracy. (a) The effect of the number of crowdsourced-trajectories, N, on the tracking performance, when method (**c**) is employed. The results show the 95% confidence interval levels. (b) The effect of the number of crowdsourced-trajectories, N, on the tracking performance when (**d**) is employed. The results show the 95% confidence interval levels.

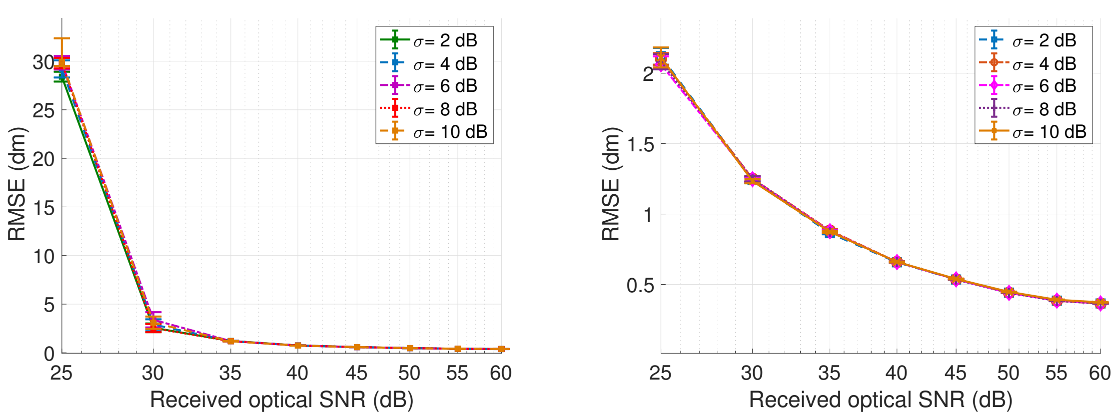

(a) (b)

Figure 4.21: (a) RMSE vs. SNR when method (**c**) is employed. The value of X_σ has almost no effect on the performance. The results show the 95% confidence interval levels. (b) RMSE vs. SNR when method (**d**) is employed. The value of X_σ has almost no effect on the performance. The results show the 95% confidence interval levels.

Fig. 4.21 (a) shows the tracking accuracy results for method (**c**) as the Wi-Fi fading parameter variance is changed. At low SNR, the performance is far worse than methods (**a**), (**b**) and (**d**). However, as the SNR increases, the performance converges to similar values as for (**d**). The question becomes which one of these two methods to use. The latter one requires more calculations due to the use of a linear KF applied on the Wi-Fi multilateration solutions, but yields higher accuracy, especially for low SNRs. The first one sacrifices a little accuracy but does not use a KF. Fig. 4.21 shows that the tracking performance is hardly affected by the value of X_σ, if crowdsourcing method (**d**) is used. Thus, the error introduced from the Wi-Fi multilateration during the crowdsourcing step does not affect the final performance. The figure also shows that with a light intensity map $\mathbf{P}$ defined over a $\Delta x = 1$ dm grid, the RMSE reaches the quantization error (less than 0.5 dm) at higher SNR levels.

As the main contribution in this section, we show that the accuracy can be increased by combining a different modality that exists in every indoor space: visible light. When we introduce the visible light measurements and its modified EKF, as explained in Section 4.1.1, the tracking accuracy increases dramatically. Fig. 4.19 shows this improvement in tracking accuracy for low to moderate VLC-SNR levels. At a low SNR (25 dB), the uncertainty noise dominates, and the performance of (**c**) is worse than (**d**). This is because the error introduced while creating $\mathbf{P}$ limits the system. However, if the SNR increases, for example to 45 dB, this error is reduced, and the tracking performance of (**c**) becomes similar to (**d**). The results in Fig. 4.19 motivate the use of a linear Kalman filter between the Wi-Fi multilateration and the $\mathbf{P}$ building process at the expense of increased computation. It also shows that the results for (**c**) and (**d**) are not affected by X_σ, although X_σ affects the Wi-Fi multilateration directly, and $\mathbf{P}$ indirectly.

4.3.4 Performance Effect of Fingerprint Maps on Indoor Tracking

The purpose of the fingerprint map is to serve as a look-up table for the probabilistic tracking filters. Therefore, the accuracy of the fingerprint map directly affects the performance of indoor positioning and user tracking. As explained above, the EKF uses the fingerprint map for a finite difference method-based linearization; on the other hand, the PF uses particles to simulate the system and chooses the particles with the highest weights. This makes the PF more accurate than the EKF but increases the number computations required, since the PF has to simulate often hundreds of particles [51].

We investigate the effect of the fingerprint maps that are obtained from nondiffusing and diffusing lamps on the tracking accuracy in a scenario where a discrete-time constant-velocity model is used as the dynamic model of the user's motion [50]. The user follows an S-shaped trajectory as given in [60]. The parameters used in the simulations are listed in Table 4.1.

In our results, the true power map is used as a benchmark to compare the other fingerprint maps. Since the RSS map is collected or constructed on a grid (equidistant discrete measurements), quantization error limits the agent tracking performance. As the SNR increases, the positioning accuracy approaches the quantization limit. In [34], a discussion on quantization and its effect can be found, and the quantization error is shown to be $\Delta x/\sqrt{6}$. This limit is drawn in Figs. 4.22–4.25.

Fig. 4.22 shows the effect of the accuracy of the fingerprint map obtained from a nondiffusing lamp on the EKF tracking error. The fingerprint map obtained using an LED mounted imaging sensor has the lowest accuracy; this method has a higher location error because the polynomial regression fit is not accurate enough to map

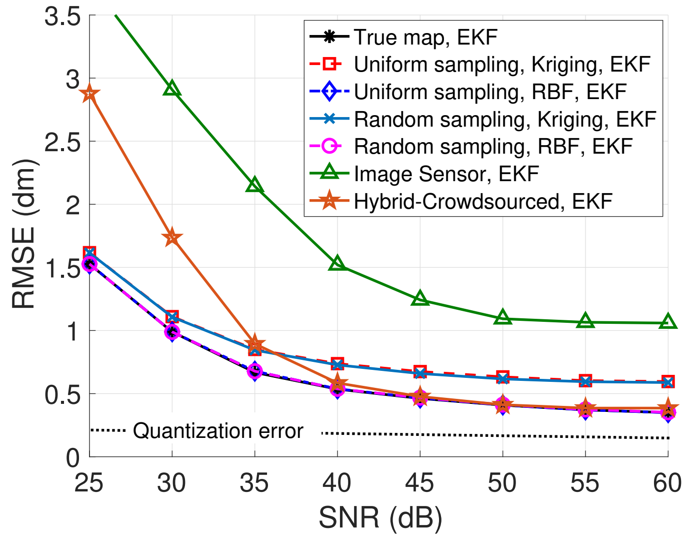

Figure 4.22: RMSE of agent position from EKF tracking based on fingerprint maps obtained from nondiffusing lamps.

from each grayscale pixel value to the corresponding RSS value. At a typical VLC-SNR = 40 dB, the positioning error is on the order of 15 cm. The hybrid-crowdsourced method does not provide high positioning accuracy at low SNR values, where the fingerprint map is not accurate because of the high uncertainty noise; at an SNR of 40 dB, however, the accuracy is around 6 cm, practically the same as the ideal fingerprint map. The agent tracking using a fingerprint map obtained using the RBF method yields better performance than the Kriging method, for both uniform and random placements of the PDs, because the RBF fingerprint maps have a much lower error, as shown in Fig. 4.13. The fingerprint maps obtained using spatial interpolation are obtained using 75% fewer measurements than a completely manual site survey. At an SNR of 40 dB, the best positioning accuracy, 5 cm, is almost as low as if the true power level was known at the grid points.

A PF with 500 particles is used to generate the corresponding results in Fig. 4.23 for the fingerprint maps obtained using a nondiffusing lamp. The same conclusions hold for the tracking results with Kriging and RBF generated maps for Fig. 4.23 as

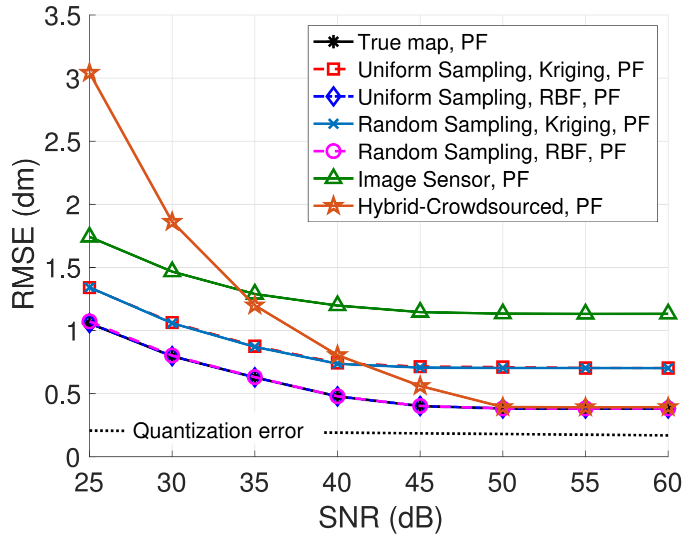

Figure 4.23: RMSE of agent position from PF tracking based on fingerprint maps obtained from nondiffusing lamps.

for Fig. 4.22. The fingerprint maps calculated using RBF yield a higher tracking accuracy. Recall that the accuracy of the Kriging interpolated power map is lower than the one obtained using RBF, and this effect can be seen in the tracking results in Figs. 4.22 and 4.23. The tracking performance using the PF is similar to the EKF also when the fingerprint map is obtained using the hybrid-crowdsourced method. However, the performance of the image sensor-obtained map using the PF is better than the EKF. There are two reasons for this: the noise on the imaging sensor can be a multi-modal or non-Gaussian noise, for which the PF is known to be superior to the EKF [55], and the PF is better than the EKF in dealing with bias introduced from the image sensor method's polynomial fit.

Fig. 4.24 shows the accuracy in agent tracking using an EKF when the fingerprint maps are obtained using a diffusing lamp. The results for the imaging sensor-based fingerprint collection method are not shown since the algorithm was tested using a single LED, and not with a diffusing lamp. The performance of the hybrid-crowdsourced method is poor at low SNR levels. The diffusing lamp creates a nonuniform yet unique

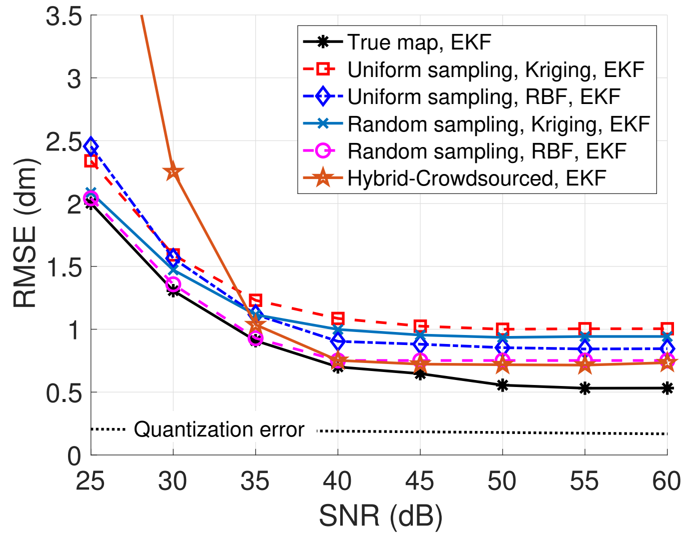

Figure 4.24: RMSE of agent position from EKF tracking based on fingerprint maps obtained from diffusing lamps.

power distribution in the surveillance area, which, when combined with high VLC noise levels, leads to a high positioning error. As the SNR increases, the performance of hybrid-crowdsourced performs almost as well as a perfectly collected fingerprint map. The performance of the spatial interpolation methods is similar to the ones obtained using a nondiffusing lamp. RBF interpolated maps perform better than Kriging interpolated maps, as expected. At an SNR of 40 dB, the accuracy of the spatial interpolation models is around 10 and 13 cm for RBF and Kriging interpolation methods, respectively. Note that the interpolation methods are no longer able to match the performance of the ideal fingerprint map because the optical power error in building the fingerprint map in the diffuse lamp case remains above 0.1 mW.

Fig 4.25 shows the tracking performance of a PF for the fingerprint maps obtained using a diffusing lamp. Results using the image sensor method are again not shown. For the hybrid-crowdsourced method, the main difference between this case and the nondiffusing lamp case shown in Fig. 4.23 is the slight degradation of the tracking accuracy at all VLC-SNR levels. The PF uses simulated particles to collect measure-

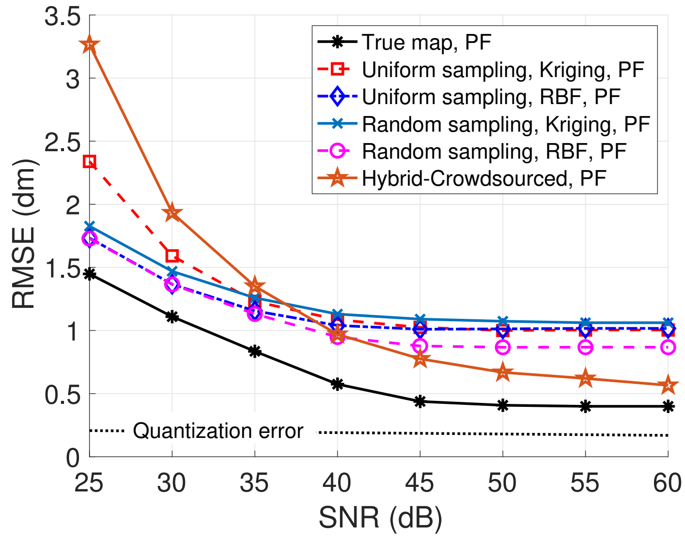

Figure 4.25: RMSE of agent position from PF tracking based on fingerprint maps obtained from diffusing lamps.

ments, as discussed in Section 3.2.4. In this case, the randomness in the fingerprint map and the high noise levels make the particle representation of the measurements inaccurate. The performance of spatial interpolation methods yields an accuracy similar to the ones of the EKF. The RBF interpolation maps provide higher accuracy than the Kriging method, with random sampling slightly outperforming uniform sampling, as expected since the tracking accuracy tends to mirror the fingerprint map building accuracy.

4.3.5 Discussion of Site Survey Methods

In this section, we discuss the applicability of the different site survey methods proposed.

A summary of the characteristics of the various methods is given in Table 4.2, where the advantages and disadvantages of each are listed. The choice of the best site survey approach depends on the indoor area of application. The effects of multipath and user measurement upload requirements are also summarized. For example, the

Table 4.2: Summary of Site Survey Methods

Site Survey	Accuracy	Map Maintenance	Multipath Effect / Requires Upload	Dependence on Crowd	Requirements	Drawbacks	Comments
Manual	High	High	No / No	No	Manual measurements	Time-consuming Error-prone Hard to maintain	Data collection is time consuming
Manual / Spatial Interpolation	High	Medium	No / No	No	Manual measurements	Requires manual data collection	Eases manual data collection
Imaging Sensor	Low	Low	No / Yes	No	Specially designed LED lamps	Low positioning accuracy	Can be used as a complementary system
Hybrid-Crowdsourced	Medium	Low	No / Yes	Yes	Large number of users / Wi-Fi access points	Dependency on user/agents	Developments in IoT and 5G favor this method

imaging sensor-based method is a promising solution for large open indoor areas where pinpoint accuracy is not critical, like a warehouse, and where the environment is not divided or obstructed by furniture or moving people. The hybrid-crowdsourced method is a better choice for indoor spaces such as malls, airports or museums, where the RSS information can be sourced from many users. The spatial interpolation method fits the needs of both spaces. Note that, the spatial interpolation methods can also be integrated with the imaging sensor-based or hybrid-crowdsourced site survey methods.

4.4 Summary

In this section, we describe a fingerprint-based approach to solve the VLC-based indoor positioning problem. We use LEDs and PDs to achieve high accuracy indoor tracking and positioning with a flexible system. Landmarks are defined as stationary VLP-enabled LED ceiling lamps. Once enough RSS and location data is collected from devices and users, we can develop a *cognitive*[1] RSS fingerprint database, which is *situation-aware*[2] to changes in the indoor area and can be used in a probabilistic tracking filter for pinpoint positioning, occupancy detection, and rapid mapping.

[1]Users provide information about the system.
[2]Changes in the database can be detected by one of the site survey methods.

Chapter 5

Localization in Optical Wireless Sensor Networks for IoT Applications

Optical wireless communications (OWC) and the internet of things (IoT) are two recent paradigms that are expected to be ubiquitous in the near future. In this chapter, we introduce an early concept of how OWC can play a critical role in IoT applications in the context of real-time location-based services. Agent localization and tracking problems have been well studied in the OWC research community with the key assumption that either the LED landmark locations are known or a fingerprint map is available. However, in real-life situations, this may not hold. Imagine a scenario, where an LED lamp location is changed, and its new position is not updated in the database, or a portable landmark is used, i.e., an optical wireless positioning-enabled (OWP) electronic device.

In this chapter, we begin our discussion by looking at traditional wireless sensor network (WSN) localization methods. In the second half of this chapter, we focus our attention on the WSN method that can be adapted to the OWC-based landmark localization problem. We consider a scenario where no *a priori* knowledge of the LED and agent locations is available. The LEDs use different codes so they can be distinguished. An agent that uses a single PD to measure the received optical intensity is tasked with discovering the LED landmark locations as it moves around the room. We use optical RSS measurements to compute the distance between the agent and the LEDs, and form geometric relations to estimate their locations. Once the LED locations are found, we can track the agent using the EKF. Moreover, the joint LED localization and agent tracking process is enhanced by using measurements that are collected by other members of the OWC-IoT network.

5.1 Discussion of Landmark Localization Methods

There are several methods of node location discovery in the WSN literature; this problem is similar to landmark initialization in SLAM problems. We restrict our discussion to the methods that use the RSS to calculate the distance. The disadvantage of distance-based methods that use the RSS is high sensitivity to noise and obstructions in the OWC channel. Next, we discuss the most common WSN node localization algorithms in the literature.

The **multilateration** method using a least-squares solution was described in Section 3.3.1. Here, we assume that the locations of the agents are available, and the goal is to localize the LED landmark.

The source localization can be modeled as a nonlinear problem in which the Gauss-Newton method is used to find the position of a LED landmark from a set of measurements at known locations. The **Gauss-Newton** method is a solution to the nonlinear least-squares problem. Assume that the Euclidean distance between the LED landmark at horizontal coordinates (x, y) and the agents at (x_k, y_k) is represented by $D_k = \sqrt{(x - x_k)^2 + (y - y_k)^2}$. The goal is to find a (x, y) value that minimizes the sum of the squares of residuals that is given as

$$S = \sum_{k=1}^{M} \underbrace{(D_k - \sqrt{(x - x_{k+1})^2 + (y - y_{k+1})^2})}_{\mathbf{r}} \tag{5.1}$$

Gauss-Newton requires the calculation of the Jacobian, $\mathbf{J}$, of S in (5.1) with respect to (x, y). The iterations start at an initial guess of (x_0, y_0), D_k represents the Euclidean distance at position index k, and the iteration is given as

$$D_{k+1} = D_k - (\mathbf{J}^T\mathbf{J})^{-1}\mathbf{J}\mathbf{r} \tag{5.2}$$

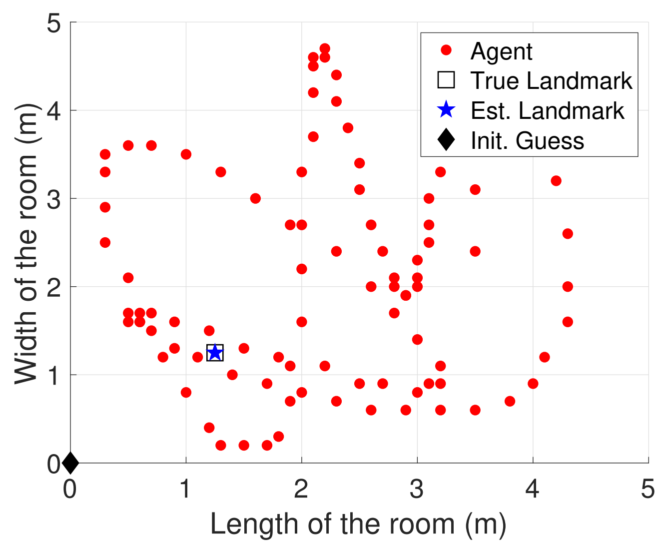

Figure 5.1: Simulation of a single LED localization using the Gauss-Newton method. True LED location is at (1.25, 1.25) meters.

Fig. 5.1 shows the nonlinear least squares solution using the Gauss-Newton method to estimate a single LED landmark location. The initial guess of the landmark is at (0, 0). Locations of the agent and the range to the landmark are assumed to be known at every sampling step.

The **Min-Max** localization method is a simple method where the idea is to measure the distance to a landmark from several locations. A vertex with a length of the estimated distance from the agent location to the landmark is drawn as shown in Fig. 5.2. The landmark location falls into the intersection of these boxes [80]. Fig. 5.2 represents a solution to localize the LED landmark using the Min-Max method.

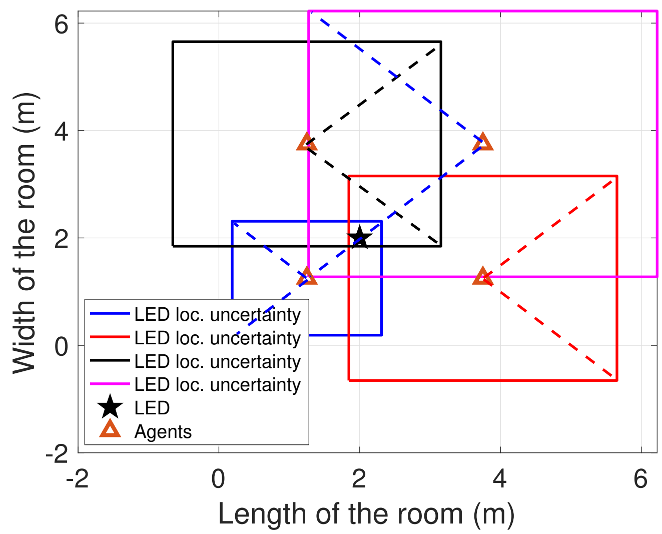

Figure 5.2: Simulation of LED initialization using MinMax method.

In the **weighted centroid localization** (WCL) method, proposed in [81], the agents or landmarks with known locations, $L_j(x,\ y)$ send their location information to all agents in the network. Traditional centroid localization algorithm uses the arithmetic mean of these locations to localize an agent at $L_i(x, y)$. In the WCL method, each agent location is weighted to improve localization accuracy. In the context of OWC, an agent measures the RSS from an LED landmark. The location of the landmarks can be calculated as

$$L_i(x, y) = \frac{\sum_{j=1}^{n}(w_{ij}L_j(x, y))}{\sum_{j=1}^{n} w_{ij}} \tag{5.3}$$

$$w_{ij} = \frac{1}{D_i j^p} \tag{5.4}$$

where w_{ij} is the weight of the distance measurement, and p is an exponent that affects the weights with respect to distance. The weights are functions of the distance since when the agent is close to a landmark, we expect to receive a higher RSS value. If the agent is close to the landmark, the value of p is higher.

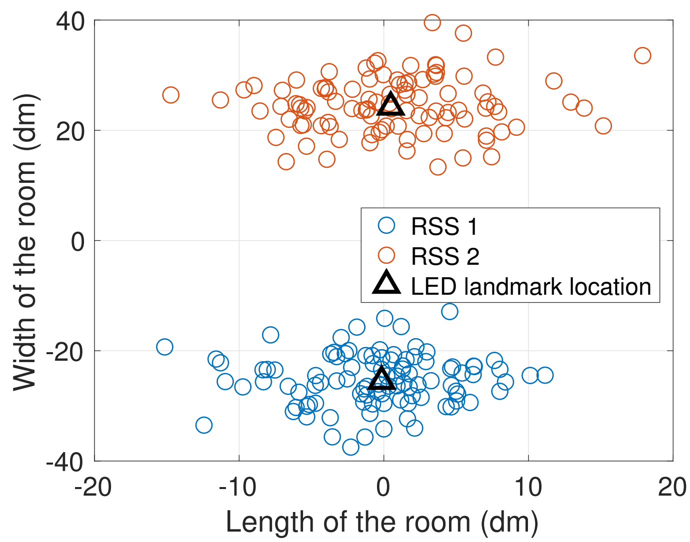

Figure 5.3: Simulation of LED initialization using K-Means clustering method.

The use of the **K-Means** clustering algorithm for source localization is proposed in [82]. The implementation to OWC-IoT sensor network can be explained as follows: assume that there are n RSS measurements from an LED landmark, and the location of the agent during these measurements are known. The centroid point of these RSS points is the LED landmark location.

In the **probability grid** method, the surveillance area is represented as a grid [83].

Each RSS measurement is associated with a grid and a weight. As the number of measurements increase, the grid is filled with RSS measurements, and the largest number of RSS measurements associated with the point corresponds to an LED landmark location.

The method of **Gaussian mixtures** is proposed in [84], where the authors use the Gaussian mixture model to represent the probability density function of the source–in our case the LED landmark. A minimum mean square error estimator (MMSE) is used to approximate this function. The source location is found by looking at the Euclidean distance between this function and its MMSE estimate.

5.2 Distance Geometry

The main difference between the methods discussed above, and the distance geometry method is the assumption that there is no information about the agent, such as odometry or inertial measurement unit information in the distance geometry method. The distance geometry method assumes that the nodes have fixed locations as described in Section 3.3.2. The only available information is the transmitted power level and the received measurement. Using the given information, the distance between node i and agent j can be estimated from (4.2), but the inter-LED distances are still required to localize the LEDs with respect to a reference coordinate system. The inter-LED distances, r_{mn}, from LED m to LED n can be estimated using the closed-form solution given in [37].

Fig. 5.4 shows a simulation scenario when there is a collaboration between the agents, e.g., other mobile users, autonomous robots, or different electronic devices. As the agent that follows the dashed trajectory moves, the RSS measurements sourced from the other agents are used to estimate the LED locations. The measurements from

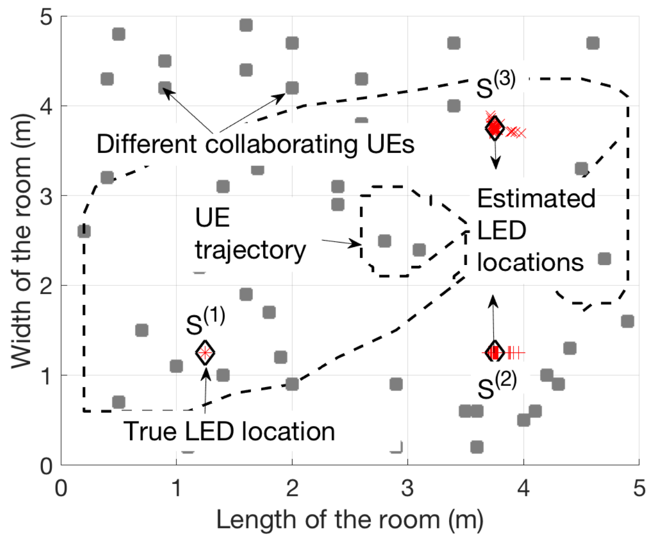

Figure 5.4: One realization of the LED node localization algorithm at 65 dB OWC-SNR. The LED locations are obtained using RSS measurements from the agents in the surveillance area.

other agents help to overcome collinearity and avoid any under-determined solution to the LED localization equations. The simulation parameters used are given in Table 5.1.

5.2.1 Performance of LED Localization Algorithm

We test the performance of the LED localization algorithm for a typical room scenario given in Fig. 5.4 using the simulation parameters listed in Table 5.1. In Fig. 5.5, we compare the performance of a single agent that collects six measurements versus six agents that collects one measurement each.

We assume that one of the LEDs is chosen as the reference node, $S^{(1)} = (0, 0)$, used as the origin of an arbitrary coordinate system. Two important conclusions can be drawn from the results in Fig. 5.5. First, the OWC-SNR level has a direct effect on distance estimation, $\hat{d}_{ij}$, between the agent and the LED, as given in (4.2), as a function of the RSS, P_{ij}. As the OWC-SNR degrades, the distance estimation error

Table 5.1: LED localization simulation parameters

Parameter	Value
Room dimension (L $\times$ W $\times$ H)	$5 \times 5 \times 3$ m^3
Number of LEDs	3
LED lamp transmitted power (P_t)	20 Watts
LED Lambertian mode	1
LED bulb elevation and azimuth	$-90°$ and $0°$
LED bulb positions	1.25 m away from the walls
PD height	0.75 m
PD field of view (Ψ_c)	140°
PD physical area (A_r)	1 mm^2

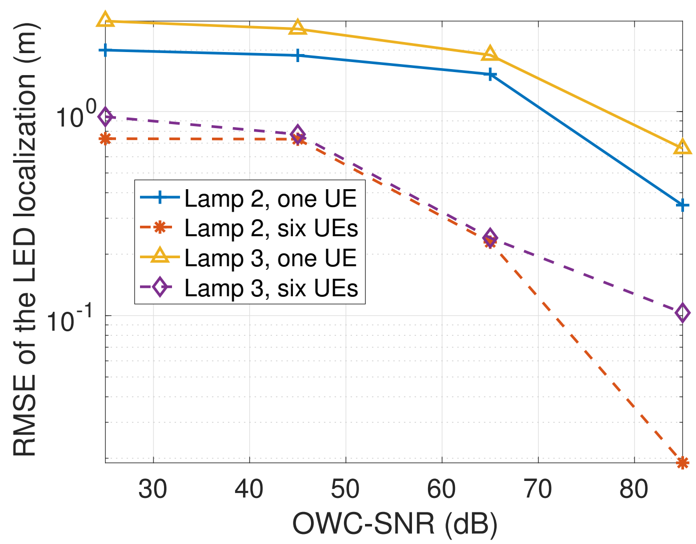

Figure 5.5: Root mean square error (RMSE) of LED location estimates from the RSS measurements sourced from a single user and six users vs. OWC-SNR using the parameters in Table 5.1.

increases. The inaccurately estimated distances increase the LED localization error. The second conclusion, more interesting for IoT device discovery, is that if we solicit the help of IoT agents at unknown locations to provide us optical RSS measurements, the LED node localization accuracy increases. The main reason is that a single agent has little displacement in time and collinearity is likely to occur. Small displacement may make the difference between observed RSS values too small to give an accurate solution to the LED localization equations as discussed in Section 3.3.2. Collinearity may happen during the collection of the RSS measurements due to the path that is followed by the agent. On the other hand, when six users are available, each of them only needs one optical RSS measurement, and the measurements have enough variations to avoid collinearity.

5.2.2 Real-Time Operation of Proposed Algorithm

In this section, we discuss how the proposed algorithm can be extended to a real-world scenario. We describe our solution that relies on measuring at least four RSS measurements from distinct LEDs. The layout of the LEDs inside a building typically follows a uniform distribution with equal distances. This kind of LED layout is common in OWC and OWP research as given in [85–87]. The purpose of this kind of LED layout is to maximize the coverage area, and increase the OWC-SNR while minimizing the interference. Fig. 5.6 shows a typical LED placement that is suitable for an indoor area such as a museum, warehouse, or shopping mall. The distance-based localization algorithm described in Section 3.3.2 does not require a uniform node distribution as long as there are at least three LED nodes in the FOV of the PD. However, the LED initialization algorithm requires one of the LED locations to be the reference point, and since the LEDs are equidistant in this section, the location of the LED with the weakest optical RSS can be found from the equal spacing.

In Fig. 5.6, $S^{(1)}$ is chosen as the reference point, from which the location of $S^{(2)}$, $S^{(3)}$ and $S^{(4)}$ can be found. As the agent moves, new LEDs will be in the FOV of the PD of the agent. Recall that since the LEDs use unique codes, the RSS from different LEDs is distinguishable. When there is a new LED in the FOV, the vector of all optical RSS from the LEDs is sorted, and the strongest three are chosen for the node localization process. The LED with the weakest RSS can be located relative to

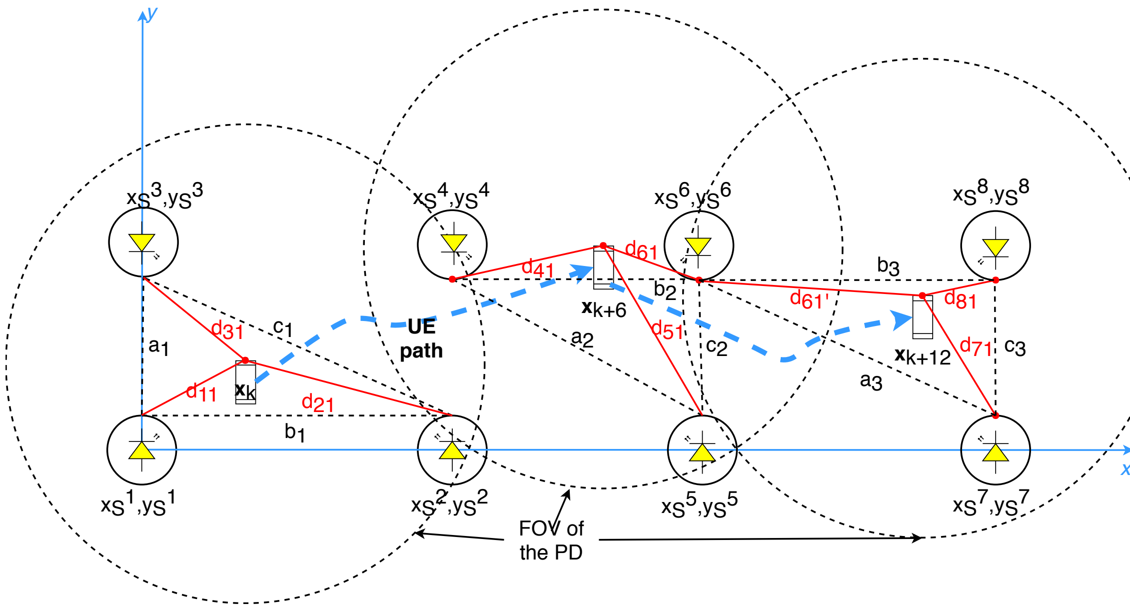

Figure 5.6: Illustration of the real-time operation of LED node and user localizations using only the distance measurements. The agent trajectory is shown as a dashed blue line.

the estimated LED location trio, using the uniform layout of the LEDs. The same steps are followed to make the algorithm general.

5.2.3 Agent Tracking Using LED Nodes

In this section, we describe the agent tracking algorithm. The fundamental difference between the well-known EKF-SLAM problem [52], distance-based sensor networks [58], and the method proposed in this section is the available information that can be used in LED and agent localization. In a SLAM problem, we have odometry information, and the state matrix has to be updated in every step to keep track of the anchors. On the other hand, in a distance-based sensor network localization problem, the node locations are known a priori. The user's location is updated with respect to node locations.

We have no odometry information or inertial measurements of the agents, the locations of the agents, or that of the LEDs. Recall that existing and new LED node locations are updated as new RSS measurements become available, as discussed in Section 5.2.2. We, therefore, do not need to include the LED position estimates in our state vector, i.e., it requires no maintenance (adding or removing LED nodes), unlike a SLAM problem. Once the locations of the LEDs in the FOV are found, the problem reduces to a classical target tracking problem with known anchor locations.

5.2.4 Agent Tracking Simulation Results

Simulation results presented in this section cover the agent tracking problem when there is a single agent, and when we have a collaboration between multiple agents. The RMSE of the agent tracking using range measurements relative to the estimated LED landmarks locations is shown.

The LED layout for simulation is as shown in Fig. 5.6. Simulation parameters needed, different from or in addition to those given in Table 5.1, are given in Table 5.2. The agent's trajectory is modeled as a constant position model as discussed in Section 3.1.

One realization of the simulation is shown in Fig. 5.7 at an OWC-SNR level of 65 dB. In the first scenario shown in Fig 5.7-(a), the RSS measurements are obtained using only one PD on the agent. Fig. 5.7-(b) shows the second scenario, where several agents collect the RSS measurements in the IoT network. These devices are assumed

Table 5.2: Agent tracking simulation parameters

Parameter	Value
Room dimension (L × W × H)	$10 \times 5 \times 3$ m^3
UE process noise variance (V_k)	0.2 m^2
Measurement noise variance (Q_k)	0.1 m^2

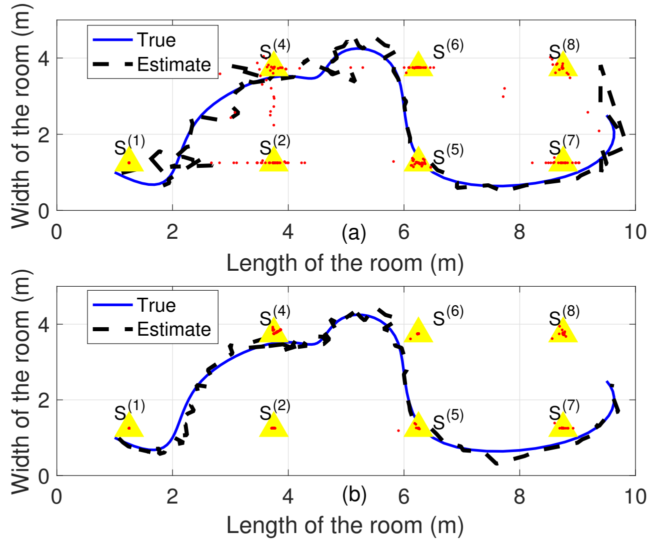

Figure 5.7: Scenarios simulated showing true and estimated agent path where (a) RSS measurements are sourced from a single user, and (b) the RSS measurements are collected from the IoT network. The red dots are the estimated LED locations when the OWC-SNR is 65 dB. The LEDs are represented as yellow triangles.

to be randomly placed. Note that using multiple agents to collect the LED RSS values improves the tracking performance.

As discussed in Section 5.2.2, the PD requires at least three LEDs in the FOV. The LEDs are grouped into trios based on the observed optical RSS intensities. When the agent first enters the indoor space, LEDs 1, 2, and 3 are in its FOV. As the agent moves, the second set of three LEDs are observed, which are LEDs 4, 5, and 7. Since the location of LED 4 is found from the first LED trio, LED 4 becomes the new reference point; the translation of the reference frame from LED 1 to LED 4 can easily be made by using the inter-LED landmark distances. The third set of LEDs is 5, 6, and 8. The same holds for these 3 LEDs: LED 5 is chosen as the reference in this case.

In Fig. 5.8, we show the RMSE results for the agent tracking using each set of LEDs. At high OWC-SNR levels, sourcing the RSS measurements from a single

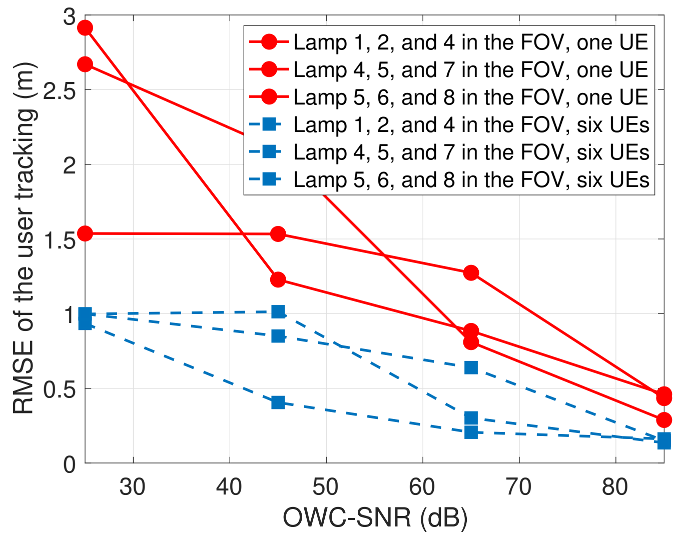

Figure 5.8: RMSE of the agent tracking. LED locations found with single agent vs. six agents collaborating to source RSS measurements for the scenario shown in Fig. 5.7.

agent or multiple agents performs similarly. At low and moderate OWC-SNR levels; however, sourcing the RSS measurements from multiple agents increases the agent tracking accuracy significantly. It can also be observed that different sets of LED trios have different performance. The trajectory of the agent that is being tracked affects the LED localization accuracy, which is directly related to the accuracy of the agent localization. For example, in Fig. 5.7 (a), there is one agent in the surveillance area, and thus the accuracy of LED localization is low. However, in Fig. 5.7 (b), there are six agents to collect the optical RSS, which leads to accurate localization of the LEDs, and the agent can be tracked with a lower error. For high SNR values, the RMSE of the agent tracking is around 10 centimeters. However, for low SNR values, the agent tracking RMSE suffers from inaccuracies in the distance estimation.

5.3 Summary

We believe that OWC systems will play a central role in IoT services. In this chapter, we show that OWC and IoT have the potential to improve LBS in the context of wireless sensor networks. Localization is a key application that can maximize OWC and IoT capabilities, such as increasing the data rate or collecting and exchanging location-application related data. In this chapter, we propose a method of device discovery and agent discovery for an OWC-based IoT network.

We investigate the case of unknown LED and user locations. We use distance measurements that are obtained from the OWC channel model and use a geometric solution to localize the LEDs. Once the LED locations have been found, any device that is connected to this network can be located, and their relative position with respect to each other can be derived. Our system is robust: even when one of the agents in the system fails, other devices connected to the network can replace the failed device without sacrificing localization accuracy.

Table 5.3: Discussion of landmark localization methods

<table>
<tr><th>Method</th><th>A priori requirements</th><th>Advantages</th><th>Disadvantages</th><th>Comments</th></tr>
<tr><td>Distance geometry</td><td>None</td><td>No information required other than distance</td><td rowspan="5">Collinear and noisy measurement decreases accuracy</td><td>Does not require any a priori knowledge</td></tr>
<tr><td>Multilateration</td><td rowspan="8">Measurement locations have to be known</td><td rowspan="3">Easy to implement</td><td rowspan="4">Well-known solution to any localization problem</td></tr>
<tr><td>Nonlinear least squares</td></tr>
<tr><td>MinMax</td></tr>
<tr><td>Weighted centroid localization</td><td rowspan="3">Works well with noisy measurements</td></tr>
<tr><td>K-Means clustering</td><td>Iterations take time</td><td>Requires large number of measurements</td></tr>
<tr><td>Gaussian mixture</td><td colspan="2">Complex</td></tr>
<tr><td>Probability grids</td><td>Easy to implement</td><td>Accuracy depends on grid granularity</td><td>Requires large number of measurements</td></tr>
<tr><td>Maximum likelihood</td><td>Works well with increasing number of nodes</td><td colspan="2">Complex</td></tr>
</table>

The major advantages, disadvantages, and requirements of node localization methods from our perspective are summarized in Table 5.3.

Chapter 6

OWC-Based Indoor Mapping Using Channel State Information

Optical wireless communications (OWC) is an emerging communication paradigm that can provide illumination, data communications, and localization services. In this chapter, we extend the capabilities of OWC one step further by proposing a novel approach that uses OWC channel state information (CSI) to build a "*sparse*" map of the surveillance area using estimated wall locations. OWC-CSI, which consists of the optical received signal strength and channel impulse response, is measured for wall location estimation. The proposed algorithm uses the time-of-flight (TOF) of the rays of the light to estimate the distance to the walls. The estimated wall locations are used as *virtual* landmarks to build a sparse map of the indoor area. This technique can be used to estimate the distance to walls and objects in robotics applications. We propose two approaches to the indoor mapping problem: OWC-infrastructure-based and OWC-infrastructure free.

6.1 Indoor Mapping Using the OWC- Infrastructure Channel State Information

One practical application of OWC is to use the LED infrastructure to find the position of a user, also known as indoor localization. OWC-based localization systems can provide a high positioning accuracy [17, 19]. The primary goal of this section is to propose an algorithm that can be used for indoor mapping or obstacle detection while localizing the user and the LEDs by building a sparse map of the surveillance area. One of the critical assumptions in this part of the chapter is that the LED lamps are equipped with high-speed LEDs or laser diodes so that we can collect the CSI accurately with a PD on the agent. The PD is chosen as the sensor instead of a camera, often used in OWC localization applications, for two reasons: a PD can provide a higher bandwidth compared to a camera [88, 89], which is the primary goal for data communications, and it consumes less power than a camera, which is critical when considering the resource constraints on a mobile agent. Collected OWC-CSI at each sampling step consists of two channel features: the optical received signal strength (RSS) and the channel impulse response (CIR).

The approach we propose in this section is novel for OWC systems, but not so for RF systems. Recently, there has been a growing interest and re-discovery of using non-line-of-sight (NLOS) components of the RF signal for localization and obstacle detection [41–43]. The estimation of a reflector's location using multipath is described in many studies using RF signals [38–40]. RF-based systems, which are widely used for indoor localization, are the main competitor to OWC-based indoor localization systems.

Sparse mapping using features obtained from images is a well-known method known as *simultaneous localization and mapping* (SLAM) [90], described in Sections

3.2.6 and 3.2.7. In this chapter, sparsity refers to localizing the wall locations with respect to the LED locations. To the best of our knowledge, there is no published effort to use OWC signals for mapping applications. The main contribution of this chapter is to propose a novel mapping method that uses optical RSS and OWC-CIR.

6.1.1 System Description

In this section, the OWC-based indoor mapping algorithm is described in detail. Fig. 6.1 shows the steps followed in the algorithm.

The OWC-CSI measurements consist of the optical RSS and features from the OWC-CIR. The peaks of the CIR are used to estimate the TOF of the multiple reflections of the light. Once the TOF is estimated, the total distance traveled by the line-of-sight (LOS) and non-line-of-sight (NLOS) rays can be estimated. Specular reflection geometry can be used to find a closed-form solution to obtain the wall-agent distance. After the distance estimation step, the wall location is resolved using circles of uncertainty that are centered at the agent location and have radii that are equal to estimated wall-agent distances. The tangent points of these circles that follow a straight line give us the wall location to build a map of the environment.

Fig. 2.1 (b) shows a typical OWC-CIR. The CIR is a superposition of the LOS and the NLOS parts of the light. The first peak is the LOS component of the light, whose time of travel is denoted by τ_{c}. The point that is labeled as the reflection from the near wall is the second peak in the OWC-CIR. The time that this peak occurs is denoted as $\tau_{\mathrm{W}}^{(1)}$. The third peak is for the far wall, and this TOF is given as $\tau_{\mathrm{W}}^{(2)}$. The superscripts (1) and (2) denote the order of the walls by the distance to the agent; extending to more walls is trivial.

The assumptions in this work are as follows: we expect the walls to be straight over a length of at least the separation of the LEDs. The vertical height between the

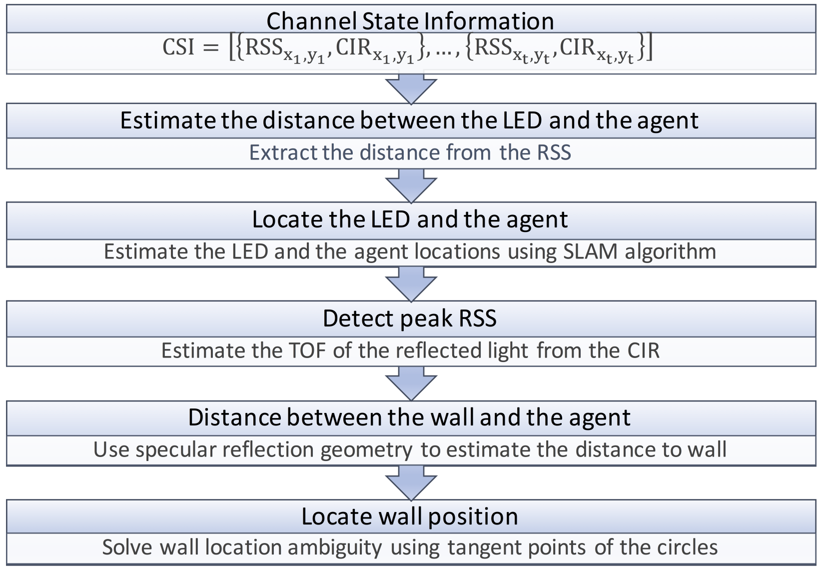

Figure 6.1: Flowchart of the indoor mapping algorithm that uses OWC-CSI in this chapter.

agent and the LED, h, and the transmitted power from the LEDs, P_{T}, are known *a priori*; this is a common assumption as the lamp designs are given and the room height is a fixed architectural feature of the indoor area. We also assume that the LED lamps contain a high-speed LED (white or infrared) to allow us to capture the CIR with high temporal resolution. The agent is assumed to be moving in a hallway with two walls. We also assume that the LED locations are unknown initially. A method to localize the LEDs and the mobile agent is required. We use an extended Kalman filter (EKF) SLAM algorithm as described in Section 3.2.6 to estimate the LED and the agent location [52]. We first explain how to use the information obtained from the channel, and then discuss the SLAM algorithm.

6.1.2 Channel State Information

The CSI in this section has two elements that are collected during the movement of the agent, the optical RSS and the peaks of the CIR. The RSS, $P_R^{(i)}$, from LED

i to an agent located at (x_t, y_t) at time step t is calculated using the OWC channel model described by (2.3) and (2.4) in Section 2.1.

Assuming that the transmitted power $P_{\mathrm{T}}^{(i)}$ is the same for all the LEDs, the estimated distance, d_{i}, between LED i and the agent is computed as described in Section 4.1.2. Each LED has a unique code so the RSS can be identified from different sources using correlation.

Fig. 6.2 shows the relationship between the required LED modulation bandwidth and the ability to distinguish separable peaks in the CIR for a high SNR case. This establishes the minimum discernible perpendicular distance between the wall and the agent. The distance and the bandwidth are approximately inversely proportional. In this section, a large bandwidth is assumed so that the distance between the agent and the wall that the CIR can capture with high temporal resolution is as small as 10 centimeters.

6.1.3 LED Location Estimation Using SLAM

In this section, the LED locations are not known *a priori*. We need an approach to estimate the LED locations. SLAM is a general name given to the problem of locating the agent and the landmarks (the LEDs in our case.) There are several solutions to the SLAM problem – we chose the EKF-SLAM algorithm as the solution to the agent and LED localization tasks [52]. In this work, the agent is equipped with a PD that can only measure the optical RSS and the CIR. The RSS measurement is used to calculate the range between the LED. Since other measurements such as the azimuth angle of the LED are not available, a range-only SLAM approach is used [91].

Fig. 6.3 shows one realization of a typical scenario in a L-shaped corridor environment. The peak OWC signal-to-noise (SNR) ratio is 60 dB. The peak OWC-SNR is described as the SNR value measured at the closest point of approach between the

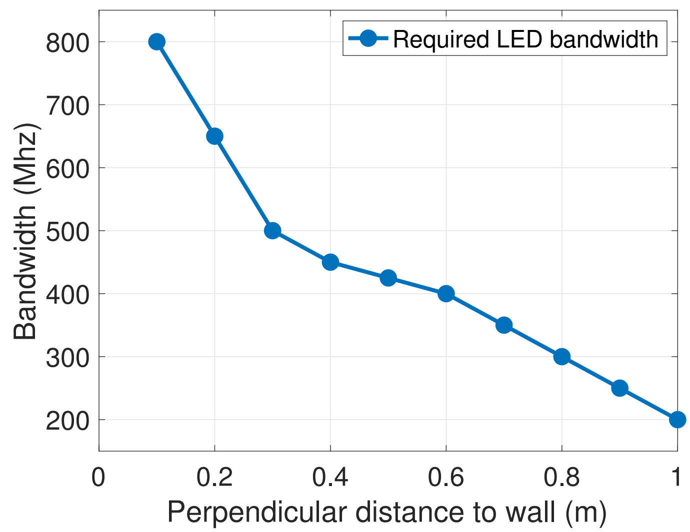

Figure 6.2: LED bandwidth requirement for detecting the OWC-CIR with respect to different distances between the wall and the agent (OWC-SNR = 80 dB).

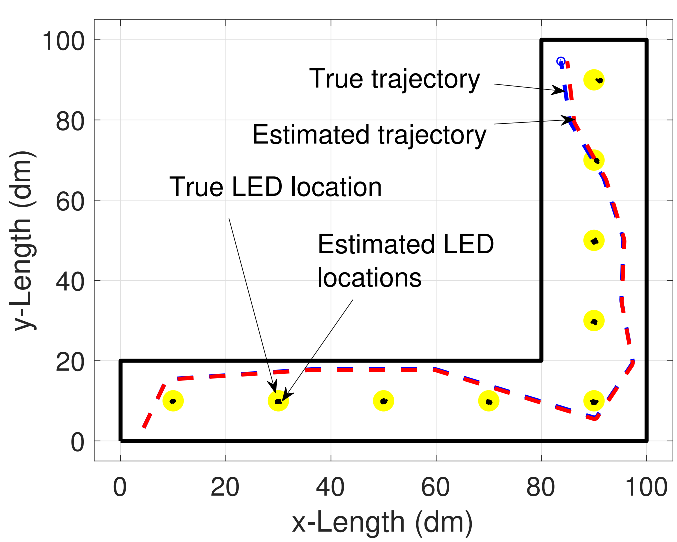

Figure 6.3: Scenario in which the range-only SLAM algorithm is tested. The peak OWC-SNR is 60 dB.

agent and the LED. The agent uses the differentially-steered vehicle dynamic model for the EKF described in [52]. The agent's state vector consists of x and y coordinates and the heading angle. The simulation parameters are given in Table 6.1.

Fig. 6.4 shows the LED localization root mean square error (RMSE) for different OWC-SNR levels. Low OWC-SNR levels have a negative effect on the LED localization accuracy. The additive noise on the optical RSS, $P_{\mathrm{R}}^{(i)}$, makes the estimation of the distance, d_{i}, inaccurate. The second observation is that the LED localization accuracy has a direct relationship with the agent's location. For the agent trajectory given in Fig. 6.3, the error on the agent localization estimates increases towards the end of the agent movement (top right). This is related to the OWC-SNR. Recall that the peak SNR is defined at the closest point of approach to the LED; when the agent moves closer to the walls the OWC-SNR decreases. The agent localization error and the OWC-SNR error increase the LED localization error.

Table 6.1: Simulation parameters for infrastructure-based SLAM

LED parameters	
Parameter	**Value**
Room dimension (L $\times$ W $\times$ H)	$10 \times 2 \times 3$ m^3
Number of LEDs	9
LED lamp transmitted power (P_{T})	20 W
LED Lambertian mode (m)	1
LED bulb elevation and azimuth	$-90°$ and $0°$
LED bulb positions	1 m away from walls and 2 m apart
Agent parameters	
Parameter	**Value**
PD field of view (Ψ_c)	$70°$
PD physical area (A_r)	1 mm^2
Standard deviation of agent velocity	0.01 dm/sec.
Standard deviation of agent angular velocity	$0.05°$

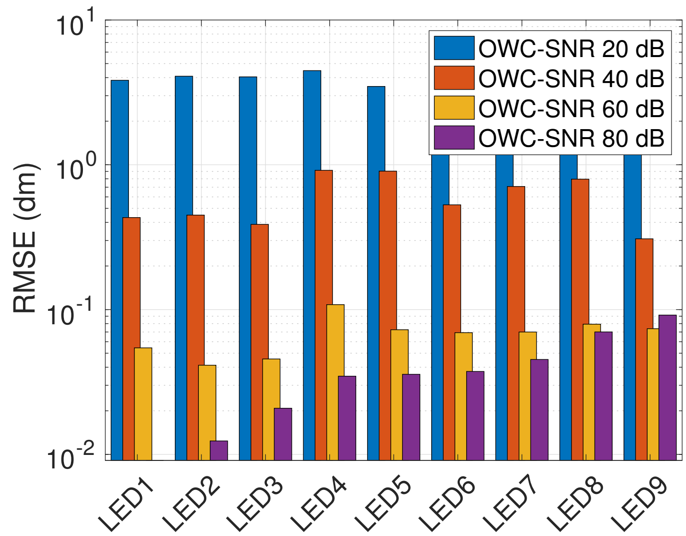

Figure 6.4: RMSE of the LED locations that are obtained using the range-only SLAM algorithm for the scenario in Fig. 6.3. The LEDs are numbered from the lower left to top right.

6.1.4 Geometric Solution to Distance Estimation

Once the LEDs and the agent are localized, the CSI can be used to estimate the distance between the agent and the walls. Fig. 6.5 shows the geometry of a reflected light ray.

TOF information obtained from the CIR tells us the total distance that is traveled by the reflected light. The reflection of the light from the walls is diffuse so many rays contribute to the CIR. Specular reflection geometry is used in this section to identify the peak of the CIR, where we assume that the angle of arrival and the angle of reflection are equal, and denoted by α. This gives the shortest path traveled by the light ray. We find the distance a (and consequently b), the perpendicular distance between the wall and the LED in 2D, as shown in Fig. 6.5. Using the notation given

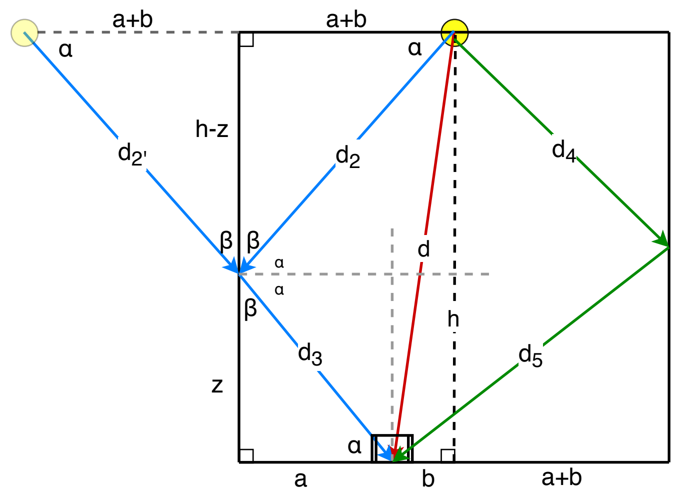

Figure 6.5: Specular reflection geometry used in this section. We assume that the LEDs are located in the middle of the hall, $a + b$.

in the figure, the resulting equations are:

$$\begin{aligned} d_2 + d_3 &= \mathrm{c} \times \tau_{\mathrm{W}}^{(1)} \\ d_4 + d_5 &= \mathrm{c} \times \tau_{\mathrm{W}}^{(2)} \\ (d_2 + d_3)^2 &= (2a + b)^2 + h^2 \\ (d_4 + d_5)^2 &= (3a + 2b)^2 + h^2, \end{aligned} \tag{6.1}$$

where b equals to $\sqrt{d^2 - h^2}$, d is found from (4.2), and c is the speed of light.

The solution of the specular reflection geometry yields an accurate result for the agent location when the agent is on a plane that includes the LED and is perpendicular to the wall. Thus, as the agent moves down the hall, we capture the optical RSS from an LED when the distance between the agent and the LED is minimum, i.e., when the RSS reaches a maximum. To find the maximum RSS, we store the optical RSS values and find the TOF from the CIR at only the peak RSS locations. Although the LEDs are located in the middle of the hall in Fig. 6.5 for notation convenience, we can obtain the distances a and b using (6.1) regardless of the LED location on the ceiling, as long as the maximum RSS is detected.

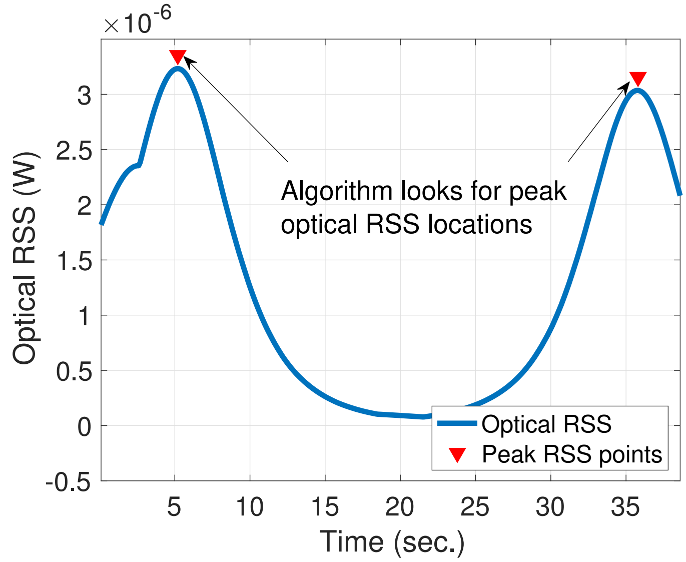

Figure 6.6: Peak RSS locations that give the most accurate solution to (6.1). The velocity of the agent is 6 cm/sec.

Fig. 6.6 shows an example of the optical RSS captured by the agent for two LEDs. The points marked with red triangles are the peak RSS points where the OWC-CIR is captured and translated to the distance a using (6.1).

6.1.5 Wall Location Estimation

The estimated distances using (6.1) give the perpendicular distance between the agent and the walls. However, there is still uncertainty on the exact wall location: the wall can be anywhere on a circle that is centered at the agent's location with a radius obtained from the estimated distance, a or $a + 2b$ (see Fig. 6.5). Recall that we assume that the agent moves in a hallway with two walls.

The ambiguity of the exact wall locations can be used to resolve the circles mentioned above. A history of at least three LED locations is stored, and the a and $a + 2b$ values obtained are used to find the exterior tangent points between the corresponding circles. The wall-location-to-distance association is illustrated in Fig. 6.7.

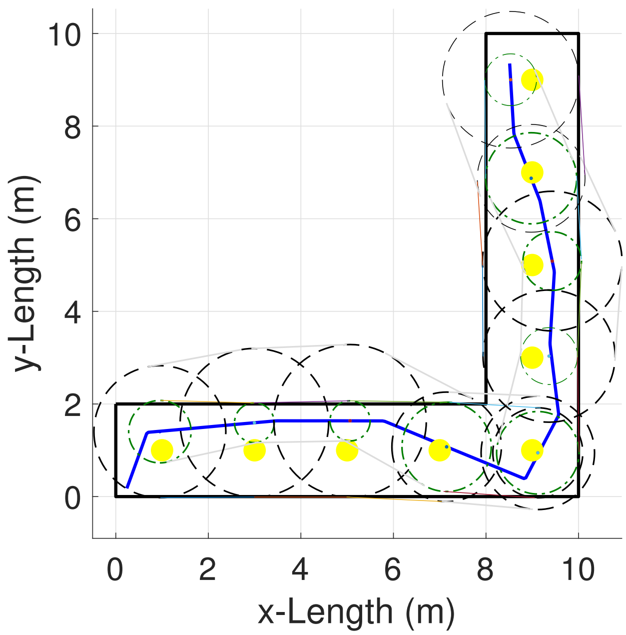

Figure 6.7: Simulation result that uses circle tangents for removing wall location uncertainty. Dash-point circles represent the uncertainty on the near wall, centered at the agent location with a radius a. Dashed line circles are for the far wall with a radius of $a + 2b$.

The agent has a peak optical RSS at each of the nine LEDs during its movement, as shown in Fig. 6.6.

The solution to (6.1) at each of these points gives a, the perpendicular distance between the near wall and the agent, and $a + 2b$ is the distance to the far wall with respect to the agent's location. The tangent points between successive small circle and successive big circle are found using simple geometry. The tangent points from at least three circles are then connected; the connections that follow a straight line represent a wall.

In Fig. 6.8, the connected tangent points are shown as estimated walls. Green lines are estimated walls from the small circle tangent points. Red lines are estimated from the big circle tangent points. Grey lines are from points that do not follow a straight line when connected and are thus rejected as irrelevant artifacts.

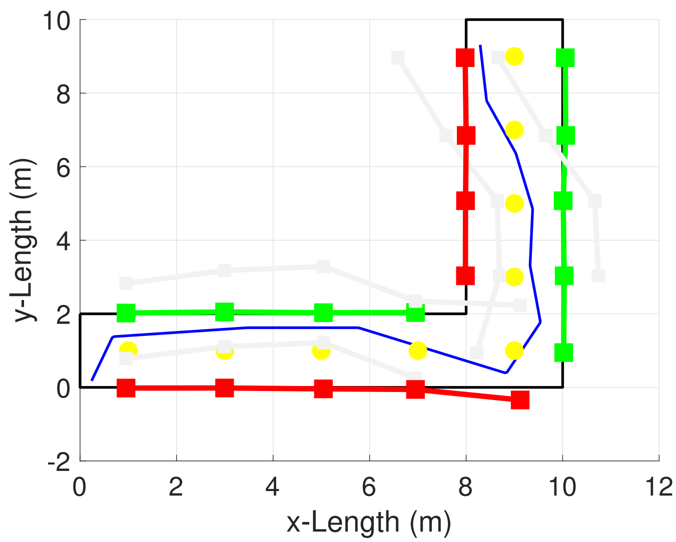

Figure 6.8: Wall locations estimated from connected circle tangents that form a straight line (green and red lines with square markers). Grey lines are the rejected tangent points.

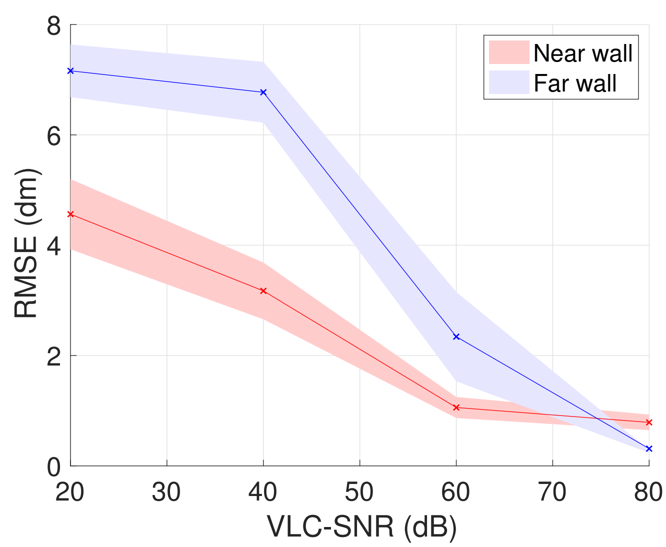

Figure 6.9: RMSE of wall localization with 95% confidence intervals after 100 random trajectories in a straight hallway model.

Fig. 6.9 shows the RMSE of the wall location estimation versus OWC-SNR for 100 random agent locations. The RMSE is high for low SNR values because the proposed algorithm relies on detecting the peak points in the CIR that correspond to reflections from walls, and lower SNR values corrupt the OWC-CIR; the detected peak points are not accurate representations of the true peaks from specular reflections.

The performance of the far wall is better than the near wall for the highest SNR value (80 dB) tested in this section. While solving (6.1) for the far wall, $d_4 + d_5 = c \times \tau_{\mathrm{W}}^{(2)}$ yields a more accurate distance estimate than for the near wall because of the fast speed of light compared with the short distances in the small indoor surveillance area.

6.2 Sparse Environment Recognition and Positioning Using OWC-CIR

In this section, a novel indoor mapping and localization method is proposed. State-of-the-art indoor mapping systems rely on complex and expensive sensing such as light detection and ranging (LIDAR) and cameras. In this section, we propose a novel approach for simultaneous localization and mapping (SLAM) front-end, sparse environment recognition and positioning, which uses an agent mounted laser diode (LD) as the primary signal. The main advantages, such as low power requirement, reduced sensor cost, and low computational complexity, come from the limited number of lasers and no moving parts, compared to a LIDAR. In our approach, an upward facing laser emits light; an upward facing photodetector (PD) measures the optical intensity of the reflected light from the ceiling and the walls. The indoor optical channel impulse response (CIR) is detected using these optical intensity measurements. The distance to the walls with respect to the agent location is calculated from the

CIR. For the SLAM back-end, we use the well-known graph optimization based algorithm described in Section 3.2.7. The results show that the root mean square error of wall localization is sub-decimeters (when using a random sampling and consensus step) for mapping and localization.

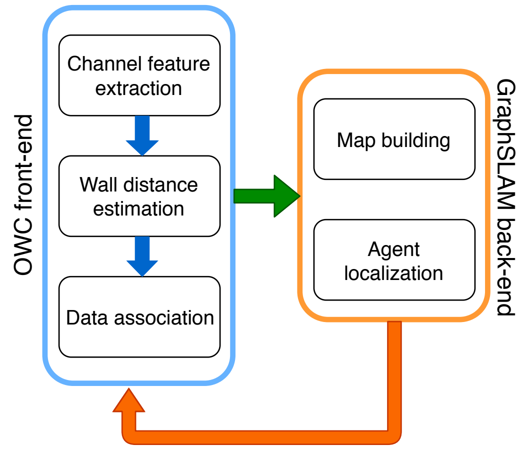

Figure 6.10: Flowchart of the OWC-based SLAM algorithm proposed in this section.

In a SLAM problem, it is common practice to divide the problem into two: front-end and back-end. The steps followed in the OWC-based front-end and the outputs of the graph SLAM-based back-end are shown in Fig. 6.10.

The proposed method can build an indoor map rapidly, and even detect obstacles. For the agent localization, the estimated wall locations can be used as virtual landmarks to find the user's location. In the front-end, the measurements are processed to extract the signal features. The OWC-CIR is used to compute the distance to the walls in the front-end. The measurements are used in the back-end of the SLAM algorithm that uses a graph optimization method.

Our method relies on the estimation of reflector locations, and these locations serve as virtual landmarks in the agent localization process. The constructed map is in 3D and consists of estimated reflection locations from the objects, e.g., walls, and the vertical height of the surveillance area. This sparse map can be used for rapid indoor mapping for robotic applications or mapping using hand-held mobile devices. The proposed method is similar to well-known ORB-SLAM [9], in the sense that estimated key points (wall locations) are used as anchor points, and the map construction process is sparse.

Unlike mapping methods that use a camera or AOA-range pairs, only distances to the walls at unknown locations, which are obtained from the TOF of the peak points in the CIR, are used. The wall location uncertainty can be represented with circles that have radii of estimated distances to the walls. We look at the point where the Euclidean distance is minimum between the circles.

6.2.1 OWC Front-End

In this study, we develop a novel front-end solution to the SLAM problem that computes the wall location by using the OWC-CIR. We start by describing the sensor shown in Fig. 6.11.

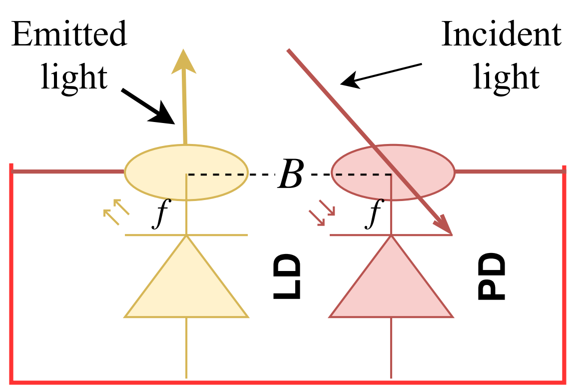

Figure 6.11: Sensor used in this study consist of a LD and a PD.

Our sensor consists of an LD and a PD, and is able to detect the OWC-CIR accurately. The sensor is assumed to be parallel to the ceiling. B denotes the distance between the center points of the LD and the PD, and f is the focal length of the lens. The light emitted from the LD is reflected from a surface and measured by the PD.

To simplify calculations, we assume that B is sufficiently small, the LD and the PD can be thought as located at the same spot.

6.2.2 OWC Channel Model and Impulse Response

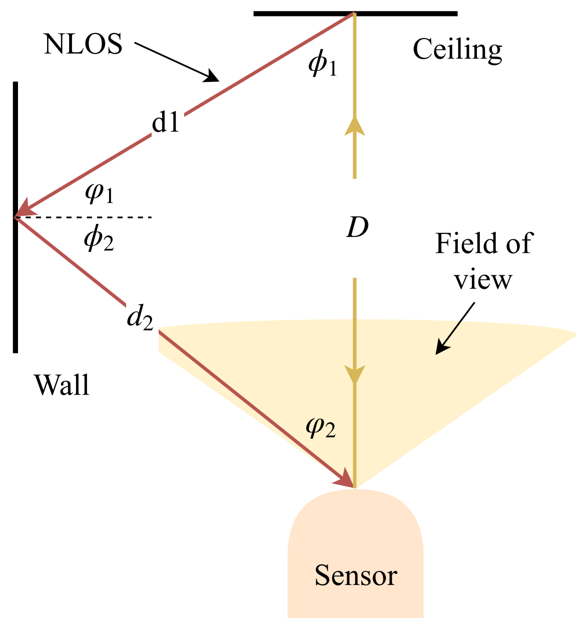

Figure 6.12: Channel geometry for calculating the OWC-CIR used in this study.

In this study, the light reflected from the ceiling and the walls is used as shown in Fig. 6.12. The pulse emitted from the upward facing LD hits the ceiling, and the PD measures the returned pulse. The non-line-of-sight (NLOS) channel gain, $\mathrm{h}_{\mathrm{NLOS}}(t)$, can be calculated as discussed in Section 2.1. According to this, we can no longer assume that the effective light source is a point source because it is a reflection of the ceiling. If the LD divergence angle is chosen narrow enough, the light shined on the ceiling can act like a Gaussian light source as given in [92].

Fig. 6.13 shows a typical normalized impulse response of an indoor OWC channel that is used in this study. The maximum amplitude peak point corresponds to the agent-ceiling-agent part of the light, and the TOF is denoted by τ. τ_{w_i} is the TOF

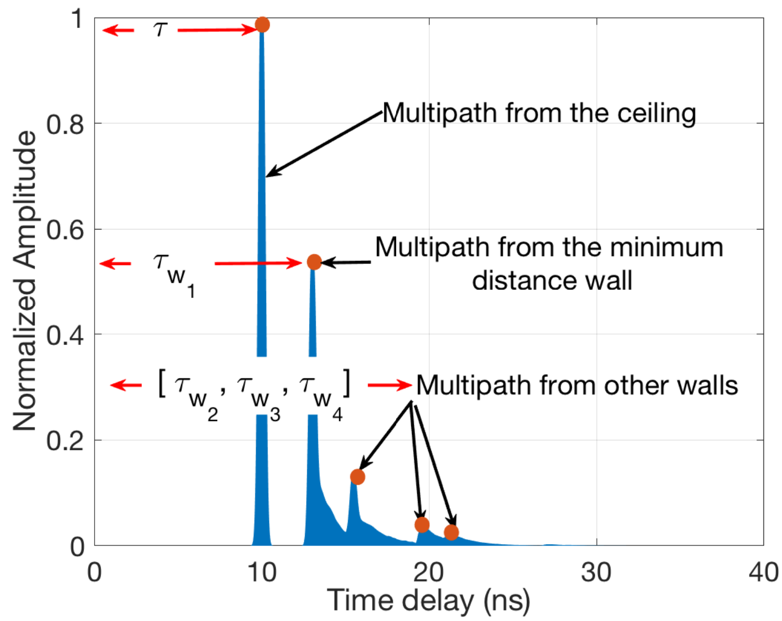

Figure 6.13: Typical normalized OWC impulse response with the multipath from ceiling and walls.

of the reflected light from the ceiling to the wall and back to the sensor, where i is the index of the wall creating the reflection. Recall that there is no LOS in Fig. 6.13, because the transmitter and the receiver are placed on the agent as shown in Fig. 6.12.

The accurate detection of the peak points in the OWC-CIR is related to the divergence angle of the LD, and the distance between the ceiling and the sensor. If the divergence angle is too large, then the spot on the ceiling is too wide to calculate an accurate impulse response. A large divergence angle may lead to inaccuracies in the detection of the peak points of the OWC-CIR.

Fig. 6.14 (a) shows the relationship between the LD divergence semiangle, θ, and the spot radius, r, and can be calculated as $r = D \tan \theta$. The room height, D, can be calculated from the TOF of the first peak in the CIR. The spot size on the ceiling depends on LD's divergence semiangle.

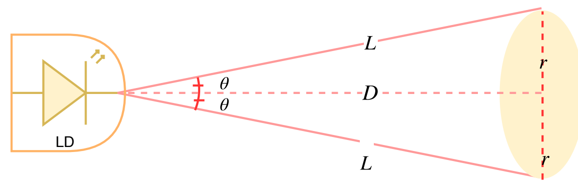

(a)

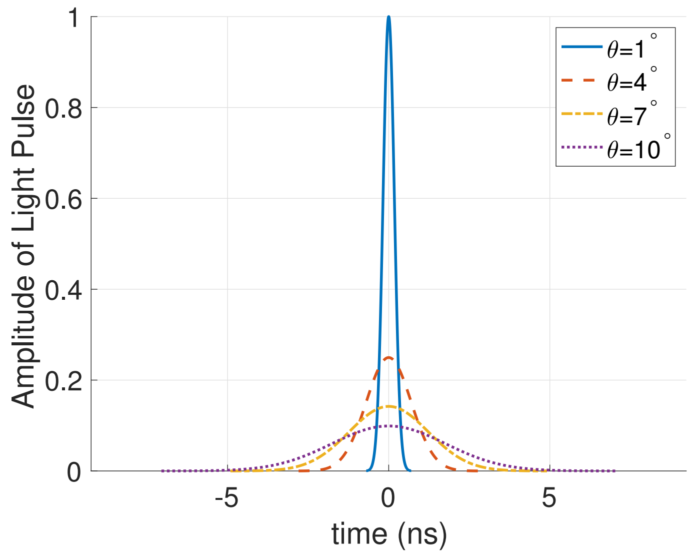

(b)

Figure 6.14: (a) Beam divergence at distance D for an LD with a semiangle of θ. (b) The relationship between the LD divergence angle and the beam shape in time at the PD.

Fig. 6.14 (b) shows the effect of the LD divergence semiangle on the spread of the light pointed to the ceiling. The distance, D, between the sensor and the ceiling is 3 meters. The spreading creates a circular light source, instead of a point source as discussed above. The circular beam shape is divided by the speed of the light, and the x-axis represents the delay of the light due to this circular light source in time. Only narrow sources allow accurate detection of the peak points in the OWC-CIR as in Fig. 6.13.

The convolution of the beam spread in Fig. 6.14 (b) and the OWC-CIR in Fig. 6.13 is shown in Fig. 6.15 for two different agent locations and several transmitted pulse of width values. The second peak that represents the nearest wall reflection is shown

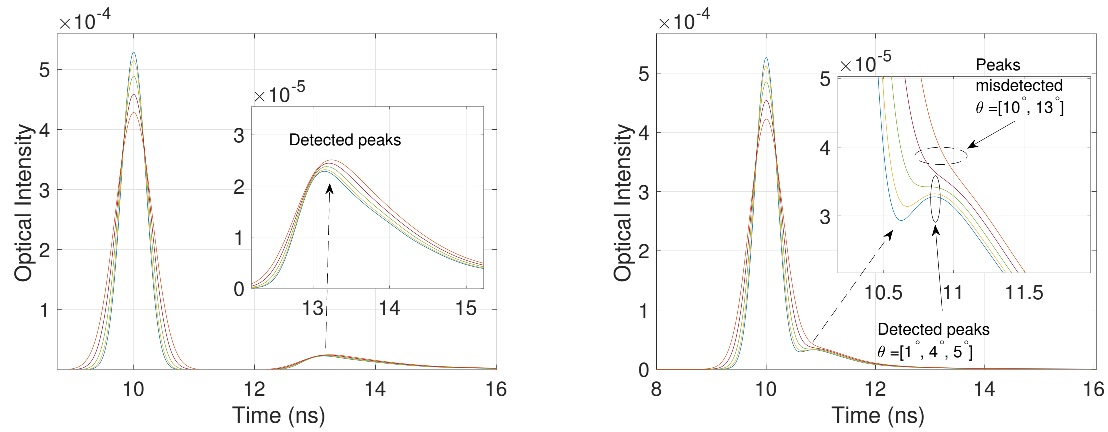

(a) (b)

Figure 6.15: Effect of LD beam divergence angle on peak detection process. Five OWC-CIRs are shown for various LD beam divergence angles for two different perpendicular distance values to the wall: (a) 1 m, and (b) 0.3 m.

in Fig. 6.15. A zoomed in part of the OWC-CIR measured by an agent at 1 m away from the wall is shown in Fig. 6.15 (a). It is seen that the for all the beam divergence angles, the second peak in the OWC-CIR can be detected. Fig. 6.15 (b) shows a zoomed in part of the OWC-CIR for an agent located at 0.3 m away from the wall. The results show that a narrow divergence angle, θ, yields better results for peak detection. The wider divergence angles spread the pulse in time, which makes the first and the second peaks indistinguishable.

6.2.3 Wall Location Estimation

In an OWC system, only real non-negative signals can be transmitted, unlike RF systems. Hence, we are limited to optical intensity measurements. In this section, we describe a way of estimating the distance to the wall using the optical RSS measurements.

Fig. 6.16 illustrates the translation of the OWC-CIR in the signal domain to the physical domain. We take advantage of the specular reflection points on the walls. A

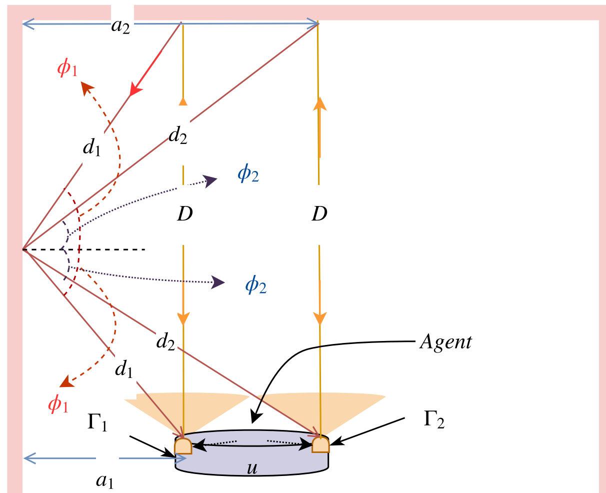

Figure 6.16: Geometric model of two upwards facing sensors. Sensors, Γ_1 and Γ_2, are placed equidistant from the center of the agent, $a_2 \geq a_1$.

specular reflection is defined as the point where the incoming and departure angles of the light are equal, and this is the shortest length ray. As shown in Fig. 6.16, we assume that the point that corresponds to a peak in the CIR is associated with a specular reflection point, which is located at $D/2$. As discussed in Section 6.2.2, the time that corresponds to the peak points in the CIR is used to calculate the distance traveled by the reflected light. If we know the total distance traveled by specular reflection, we can calculate the distance to a reflecting surface using a closed-form geometric equation. This geometry, also known as the two ray multipath [93], is used to calculate the distance between the agent and the wall in $\mathbb{R}^2$:

$$
\begin{aligned}
D &= \tau \times c \\
d_1 &= \frac{c \times \tau_{w_1}}{2} \\
a_1 &= \sqrt{\left(d_1 - \tfrac{D}{2}\right)^2} \\
d_2 &= \frac{c \times \tau_{w_2}}{2} \\
a_2 &= \sqrt{\left(d_2 - \tfrac{D}{2}\right)^2}
\end{aligned}
\tag{6.2}
$$

TOF information is obtained by looking at the OWC-CIR peak point time indices. d_1 and d_2 are the distances from the ceiling to specular reflection points, and also the distance from the specular reflection points to the sensors. c is the speed of light. τ, τ_{w_1}, and τ_{w_2} are the time of peak points in the CIR. a_1 and a_2 are the distance of the sensor locations to the wall. Recall that for simplicity we only show a single wall; extension to multiple wall locations estimation is trivial.

6.2.4 Link Budget Analysis

In this section, we calculate the minimum transmitted power that is required to satisfy the OWC-SNR level for accurate detection of the second peak point in the OWC-CIR. In an OWC, the noise is comprised of two effects: thermal and shot noise. We add a third term as explained is Section 2.3. The total noise variance is the sum of variance the thermal, shot, and uncertainty noise:

$$
\begin{aligned}
\sigma^2_{\text{total}} &= \sigma^2_{\text{thermal}} + \sigma^2_{\text{shot}} + \sigma^2_{\text{uncertainty}} \\
\sigma^2_{\text{thermal}} &= 4\kappa T_K B / R_L \\
\sigma^2_{\text{shot}} &= 2qP_{\text{R}}B
\end{aligned}
\tag{6.3}
$$

where κ is Boltzmann's constant, $T_K = 300$ K is the temperature in Kelvin, $B = 350$ MHz is the receiver bandwidth. $R_L = 50\ \Omega$ is the resistor value in the receiver circuit. q is the electron charge.

As discussed in Section 2.3, the SNR is the ratio of the received optical power to the noise power in the system. If we only consider the contribution of thermal and shot noise calculated using the parameters above, SNR of the first peak is 50 dB. For the second peak, the SNR is 35 dB at a sensor located 0.5 m away from the wall.

Fig. 6.17 shows the contribution of the uncertainty noise on the accuracy of peak detection. From the results, it can be seen that the minimum required SNR value for an acceptable accuracy level is 40 dB. Note that we are interested in the TOF of the second peak, so the receiver needs to accumulate several pulses to achieve the desired performance given the parameters listed above. To achieve that performance, the minimum required transmitted power is calculated to be at least 20 mW with a pulse repetition frequency of 50 KHz [94].

$$SNR_{\tau_{W_1}} = \frac{\nu P^2_{\tau_{W_1}} \rho}{\sigma^2_{\text{total}}} \tag{6.4}$$

where ν is the number of pulses received, and ρ is the PD responsitivity.

6.2.5 Effect of Transmitter Bandwidth on Wall Location Estimation

Another important design parameter of this work is the transmitter bandwidth. The OWC-CIR needs to be measured with high spatial resolution so that the peaks in the CIR can be identified accurately.

Fig. 6.18 shows the RMSE of the wall localization error versus the transmitter bandwidth for various distances to the wall. The results show that the transmitter

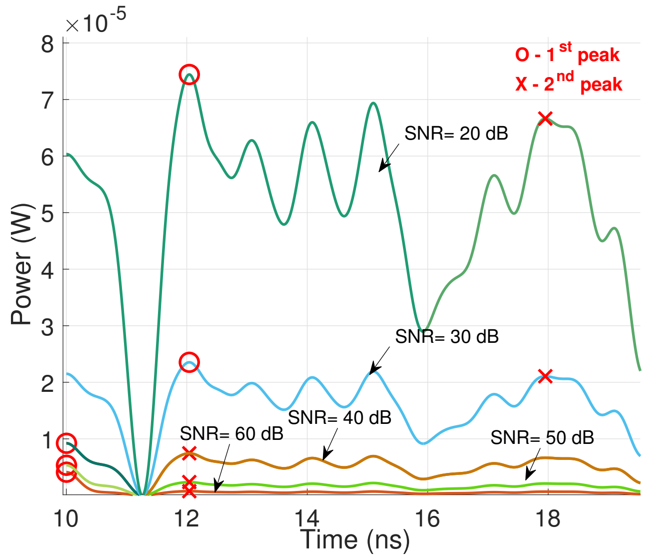

Figure 6.17: Relationship between peak detection and SNR

bandwidth and the perpendicular distance between the wall and the sensor can be a limiting factor on the accuracy. When the sensor is 50 cm away from the wall, the required bandwidth is more than 350 MHz, however, if the sensor is closer to the wall, 20 cm, the required bandwidth to capture the OWC-CIR accurately is more than 1 GHz. Considering the capabilities of new semiconductor devices such as VCSELs, the required bandwidth values are realistic [95].

6.2.6 Resolving Wall Locations Ambiguity

In this study, a sensor located on the agent is denoted by Γ_i, where i denotes the sensor index. There are two sensors with an offset of u from each other as shown in Fig. 6.16, $i = 2$. At each time step t, the LD transmits a coded pulse, and an impulse response is received indicating all main reflections, including the ceiling bounce and the diffuse bounces from the walls. From these measurements, we can find the TOF from which we can compute the distance to the walls.

Recall that we are using PDs, and there is no AOA or visual information regarding

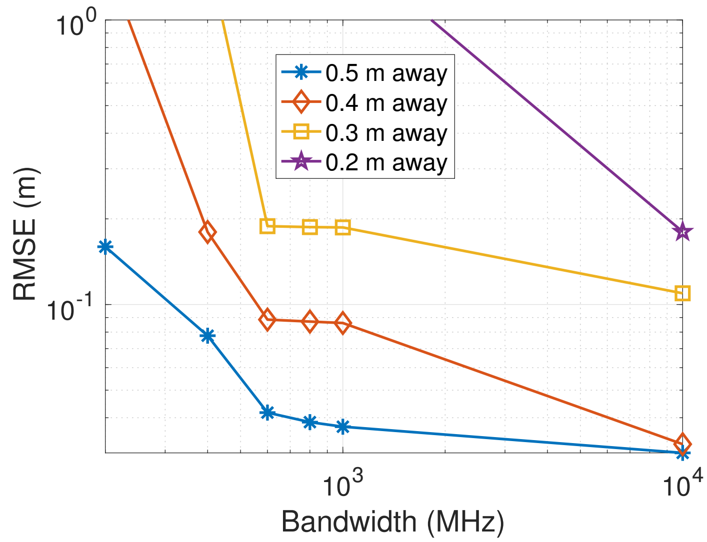

Figure 6.18: Effect of distance and transmitter bandwidth on wall localization RMSE.

the relative wall locations. The agent does not know where the walls are, or which wall the agent is moving towards with respect to the sensor. The problem of data association is a major challenge to overcome for accurate mapping.

Fig. 6.19 illustrates the steps followed to estimate the wall locations. Our approach uses the fact that we estimate two distance values from the sensors by using two PDs. Once the measurement from a sensor to a wall, a_i, is available, we estimate the distance to a wall resulting in a circle of ambiguity. The center of each circle is the sensor on the agent, $\Gamma_i(x, y)$, where x and y are the Cartesian coordinates with respect to the midpoint between the sensors on the agent. If the agent has two sensors, there will be two circles as shown in Fig. 6.19. Using the history of m consecutive measurements as the agent moves, the circle planes are stacked vertically. We see that the points on these two circles with minimum Euclidean distance give us wall location estimates. This method is used to solve the data association problem of estimated distance and the reflected wall problem location in 2D coordinates. We estimate the room height using the ceiling bounce. We end up with a sparse 3D representation of

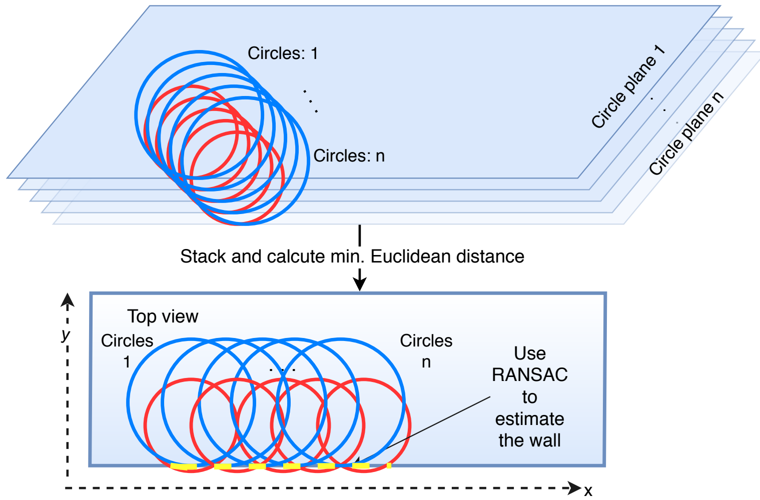

Figure 6.19: Resolving the wall position uncertainty using a history of circles and RANSAC.

the surveillance area.

We can further improve the wall localization estimation by rejecting erroneous wall location estimates. The random sampling consensus (RANSAC) algorithm can be used to fit the best possible line to the history of the estimated wall location points [96].

6.2.7 Graph SLAM Back-End

In this section, we use the graph optimization SLAM [56] described in Section 3.2.7 to build a map of the environment and locate the agent. The estimated wall distances are used to localize the agent. Our goal is to build a graph that consists of nodes and edges from the motion of the agent and the measurements.

Once the problem is represented as a graph, we can optimize this graph to locate the agent and build a map of the space indoor that represents of wall locations. The nodes of the graph correspond to the displacement of the agent between $t-1$ and t, and the distances to observable walls during $t-1$ and t are represented as the edges, where t represent the time index. The edges represent the spatial constraints between the nodes.

The state of the agent is represented by $\mathbf{x}_t = [x_t,\ y_t]$, where x and y are the Cartesian coordinates of the agent, and t represent the time index. At each time step, the control input to the agent, $\mathbf{u}_t$, is known. The distance between the wall and the agent at time step t is denoted by $\mathbf{z}_t$. We use this information to construct the information matrix and vector defined in Section 3.2.7. A more detailed explanation of the graph-SLAM algorithm can be found in [56].

6.2.8 Simulation Results

We test the proposed joint mapping and localization algorithm on different trajectories for the same room conditions. Table 6.2 gives the parameters used in our simulations.

Associating the estimated distances to the corresponding walls using only the OWC-CIR is a challenging task since it is impossible to estimate the direction of arrival of the multipath light signal with a single PD. The method described in Section 6.2.6 is developed to resolve this problem. Fig. 6.20 shows the simulation result for the proposed data association algorithm for a linear trajectory.

Fig. 6.20 shows how to use the circles that are centered on the sensors with radii a and b for wall location estimation. In this simulation scenario, we assume that the agent is equipped with two sensor packages, Γ_i, with an offset of 0.4 m. The simulation parameters are given in Table 6.2. The estimated wall positions correspond to the point where the Euclidean distance between yellow and red circles is a minimum. The circle radii are estimated from the OWC-CIR as described in Section 6.2.3. Note that as the agent moves towards the center of the room, the error of the wall estimation increases. This error is due to quantization introduced during the calculation of the CIR in simulations.

Table 6.2: Simulation parameters for infrastructure-free SLAM

Parameter	Value
Room Dimension	$10 \times 10 \times 3$ m^3
Agent Dimension	$0.5 \times\ 0.5 \times\ 0.1$ m^3
Sensor offset	0.4 m
Agent velocity variance	1 (cm/s)^2
Agent angular velocity variance	0.25°
LD beam divergence	14°
LD transmit power (P_t)	20 mW
LD rise time	1 ns
LD lens refractive index	1.5
Optical concentrator gain	2
Pulse repetition rate (ν)	50 KHz
PD aperture	1 mm^2
PD responsitivity	0.95 A/w
Room reflection coefficient (ρ)	0.8

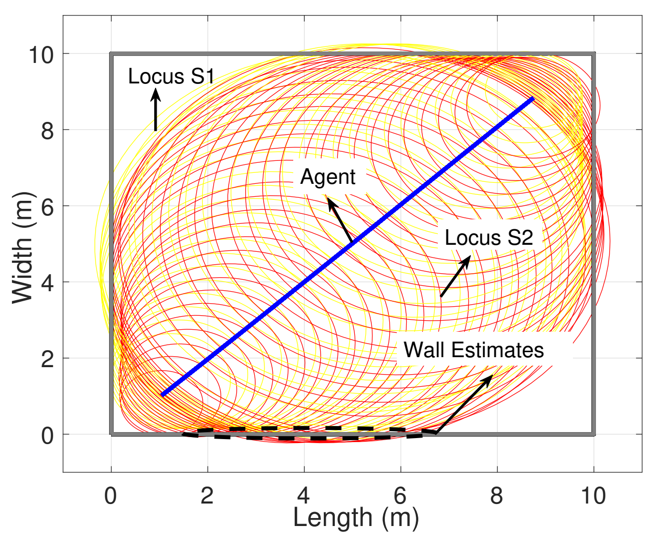

Figure 6.20: Estimated distance-to-wall association using a history of circles for different sectors of an agent movement.

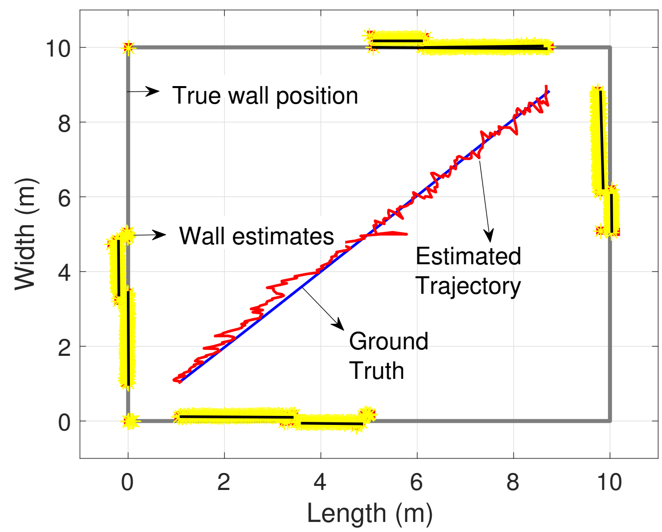

Figure 6.21: Wall localization and user tracking using the proposed mapping and localization method. Yellow asterisks are the estimated wall locations, the black lines are the computed wall locations after RANSAC. Estimated user trajectory is shown with red lines.

Fig. 6.21 shows a realization of the wall location estimation and user tracking for a linear agent trajectory. This kind of trajectory is the worst case scenario for our mapping and localization method because the agent is equidistant from the walls during its movement. Recall that the detection of the peak points in the OWC-CIR is used to find the wall locations, and the detection of the CIR peaks is hard when there are no distinct peak points. Also, since we simulate the CIR using a computer, quantization error is introduced.

In Fig. 6.22, we test the performance of the mapping and localization method for a different user trajectory where this time the user moves closer to the walls, which yields a better CIR in terms of easier peak distinction and detection. This yields a wall localization RMSE under 3 centimeters after applying the RANSAC algorithm.

For the results shown in Fig. 6.23, the peaks in the CIR stemming from the first and second closest walls are used to estimate the wall location. Recall that, in Fig. 6.21 and Fig. 6.22, we assume that the reflection from the closest wall is used to

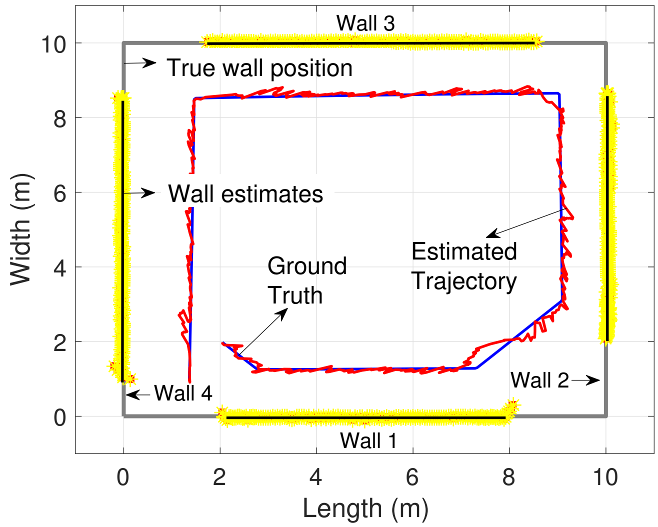

Figure 6.22: Wall localization and user tracking with the proposed mapping and localization method for a user trajectory with different sections.

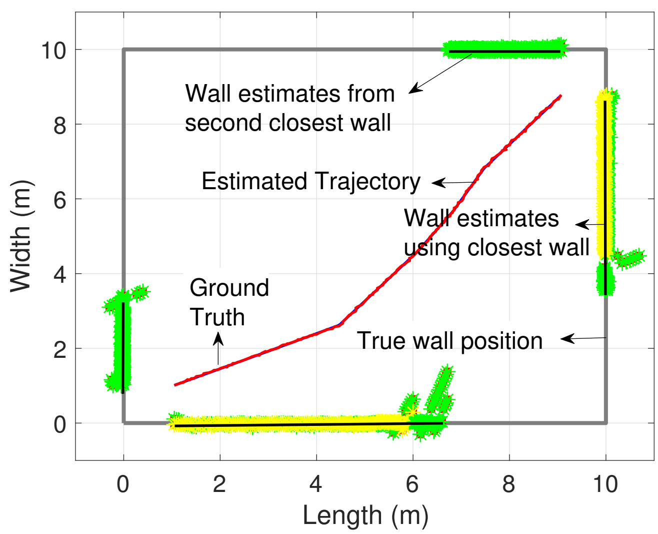

Figure 6.23: Mapping and localization when the reflected light from the first and second closest walls is used. Yellow asterisks are for the closest wall, and the green ones are for the second closest wall.

find the wall locations. The RMSE of the agent tracking is 8 centimeter for the test trajectory. The mapping accuracy is lower in this case compared to mapping using the first peak point. The RMSE of wall localization is around 10 centimeters before the RANSAC. The detection of peaks becomes challenging as the optical RSS of the reflected light decreases, and this makes finding the peak points in the CIR harder as the number of peak points used for mapping is increased.

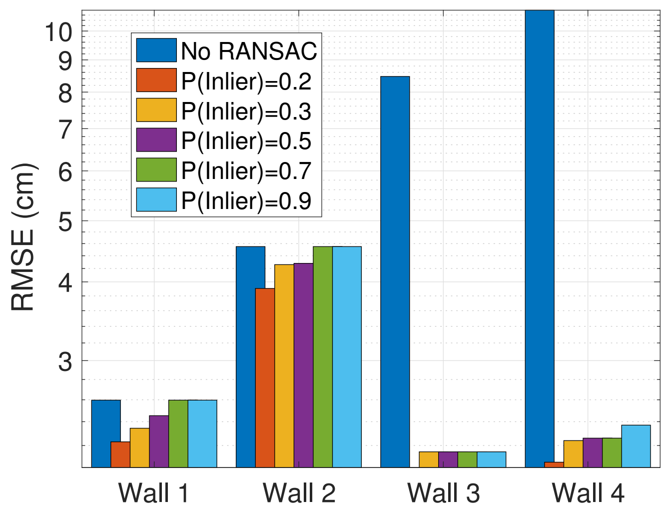

Figure 6.24: RMSE of wall location estimation for scenario shown in Fig. 6.22 before and after the RANSAC with various inlier probability values.

We test the performance of the RANSAC for different inlier probabilities as shown in Fig. 6.24. Inlier probability can be defined as the probability of a point that has a squared error less than a predefined error threshold (10^{-7} in this study). Before RANSAC, the RMSE of the wall error localization error can go as high as 10 cm. The high error and the perpendicular distance to the wall of the agent are correlated. As the agent moves too close to the wall, the detection of the peaks from the OWC-CIR becomes impossible. On the other hand, if the agent moves too far from the wall, the peaks cannot be detected accurately; this leads to a high wall localization RMSE. However, after we apply the RANSAC algorithm, the error decreases dramatically.

This can be observed for walls 3 and 4 in Fig. 6.24. The results are obtained from the test case given in Fig. 6.22. With a low inlier probability, the accuracy of wall mapping can be less than 3 centimeters.

6.3 Summary

In this chapter, we propose an indoor mapping and localization method that uses the OWC-CIR to estimate the TOF information. The method can be infrastructure dependent or infrastructure free. This new approach is suitable for mobile devices with limited power and processing capacity, such as mobile robots or hand-held electronic devices, thanks to its low power sensors and light-weight signal processing algorithms.

Chapter 7

Conclusions and Future Work

This dissertation has addressed three main research tasks: fingerprint-based indoor localization, landmark and device discovery, and mapping using the OWC channel features. The goal is to propose a complete solution for the OWC-based indoor localization and mapping problem.

7.1 Research Contributions

The research contributions of each chapter are as follows.

Fingerprint-based localization

- The problem of linearizing the OWC channel model is a challenging task. This makes using probabilistic tracking filters hard to use for OWC-based indoor positioning. We solve the channel linearization problem by using a finite difference method that relies on a database of *a priori* measurements instead of using the channel model directly, as in multilateration solutions. [19, 60].
- In the ideal case, the LEDs transmit the same power, and the fingerprint

database is built for identical lamps transmitting identical power. In real-world scenarios, one or more of the LED lamps can be broken or operate faultily. We investigate the effect of unexpected RSS measurements in [60].

- The main drawback of fingerprint-based localization is the site survey process, in which location-related measurements are collected. In this dissertation, we propose three solutions to overcome this difficulty of fingerprint-based localization. We propose to use geospatial interpolation methods to build a fingerprint map with a limited number of measurements. An LED lamp that is equipped with a camera can be used to capture the light distribution in the room. The image from this camera is used to build a fingerprint map [61]. Already-existing Wi-Fi infrastructure and the users in the surveillance area can help us to build and update the fingerprint map as proposed in [63].

- In a general localization problem, the locations of reference points are assumed to be always known *a priori*. In real-world problems, however, the locations of the LEDs may be different from the architectural plan or may change over time due to remodeling or changes in the plan. This necessitates a LED landmark discovery step. We propose a method that relies on distance measurements in [97].

- We propose two approaches to build a physical map of an indoor area that can be used instead of the commonly employed LIDARs. In the first method, we assume that the light bulbs are equipped with high speed white or IR LED. We use the PDs on the agent to build a map of the environment from the OWC channel state information. The algorithm relies on detecting the TOF of the light rays [6].

  In the second mapping method, we use the same building blocks as a LIDAR:

laser diodes (LD). These elements attached to the agent are used to build a map of the environment again using the OWC channel state information. The main contribution of this method is its low cost, lightweight signal processing, and low energy consumption compared to a LIDAR.

7.2 Conclusions

In VLC fingerprint-based indoor localization systems, conducting the site survey is challenging, requiring highly accurate offline measurements that require exhausting manual labor. This is why VLC fingerprint-based algorithms are not currently attractive for real-life applications of indoor positioning systems.

In this dissertation, we propose three different solutions for fingerprint collection in VLP systems: spatial interpolation that reduces the complexity of manual site surveying, an imaging sensor-based algorithm, and a hybrid-crowdsourced technique that uses Wi-Fi.

The first approach uses an interpolation method that relies on the smoothness of the indoor lighting and requires fewer measurements than a completely manual site survey. The interpolation methods provide almost as high an accuracy as an ideal fingerprint map. However, these methods require RSS measurements with known locations. The second method, an imaging-based technique, requires equipping the light sources with a camera and a calibration function to transfer from the image domain to the optical RSS domain. Camera-based fingerprint data collection is the simplest to apply; however, the accuracy is the lowest among the algorithms tested. The third method, the hybrid-crowdsourced approach, uses Wi-Fi to help locate the users and relies on the smoothness of the indoor lighting. It uses both the Wi-Fi APs and LEDs for positioning. In the case of LED failure, the Wi-Fi trilateration can still act as a rough positioning system. Our results show that the proposed site survey methods can provide highly accurate fingerprint maps, comparable to a perfectly collected fingerprint survey.

In this dissertation, probabilistic tracking filters are used to track the UE. The fingerprint maps help calculate the Jacobian of the measurement function in the EKF and the likelihood of the particles and measurements in the PF. Our results show that the accuracy of the fingerprint map has a substantial influence on the accuracy of the tracking filter's estimate of the UE position. Comparing the probabilistic tracking filters, the performance of the PF is slightly better than the EKF, as expected. However considering the complexity of the PF, the EKF is a viable solution to the problem. The main issue with the EKF is the linearization of the measurement function, the granularity of the finite difference method for estimating the Jacobian that is related to the fingerprint map resolution affects the tracking accuracy. When the grid step size in decimeters, the RMSE of the agent position is around 5 centimeters.

Another important conclusion can be made for LED localization for future of VLC internet-of-things (IoT) networks. Most of the methods used in wireless sensor networks (WSN) require the location of the agent to localize the landmark. The method that we focused on in this dissertation does not have this constraint. It can localize the landmarks by calculating the distance to at least three landmarks in the FOV of the PD. Although this distance-based geometric method has drawbacks such as susceptibility to noise and collinearity, we believe that this method can be used in cooperation with other WSN methods. A complete free space optical WSN system can be built. LED localization can be below 1 decimeter. The accuracy depends on the VLC channel SNR and the measurement locations.

In the context of indoor mapping, a novel mapping and localization method is introduced that uses low-power LDs and PDs as the sensors. The primary goal is to measure the OWC-CIR as accurately as possible and extract the light reflection TOF from the CIR. Our new approach is suitable for mobile devices with limited power and processing capacity, such as mobile robots and hand-held electronic devices, thanks to its low power sensors and light-weight signal processing algorithms. The accuracy of wall localization is around 2 to 5 centimeters after the RANSAC step.

7.3 Future Work

Visible light positioning (VLP) is an emerging IoT research area that has garnered attention for its positioning accuracy capabilities because of the predictable signal characteristics of visible light. The versatility of VLC systems helps to develop several indoor positioning algorithms that use either a PD- or a camera-based positioning system. VLC has the potential to link all "things", such as mobile phones, computers, gaming consoles, and home appliances to create an energy-efficient, RF-interference-free indoor localization network by using the LED lights and indicators. This VLC-based network of location-aware things can provide position information and situation awareness everywhere in an indoor space, such as smart-buildings. With the help of pervasive LEDs and PD equipped devices, sensing can be smart and efficient to provide detection, tracking, and mapping. We think that in the future it is possible to use LEDs and PDs to achieve high accuracy indoor tracking and positioning with a flexible system that requires no prior position information of the VLP enabled devices. The system will locate the position of the devices with respect to each other from the LED received signal strength (RSS) detected by a PD in a "landmark" discovery step. Landmarks can be defined as stationary VLP-enabled devices. Once enough RSS and location data is collected from devices and users, a cognitive RSS fingerprint database, which is situation-aware to changes in the indoor area, can be used in a probabilistic tracking filter for pinpoint positioning, occupancy detection, remote sensing, and rapid mapping.

Bibliography

[1] A. A. Makarenko, S. B. Williams, F. Bourgault, and H. F. Durrant-Whyte, "An experiment in integrated exploration," in *IEEE/RSJ International Conference on Intelligent Robots and Systems*, vol. 1, Sep. 2002, pp. 534–539 vol.1.

[2] J. Sola, "Simultaneous localization and mapping with the extended Kalman filter." [Online]. Available: http://www.iri.upc.edu/people/jsola/JoanSola/objectes/curs_SLAM/SLAM2D/SLAM%20course.pdf

[3] G. Strang and K. Borre, *Linear algebra, geodesy, and GPS.* Wellesley-Cambridge Press, 1997.

[4] R. Mautz, "Indoor positioning technologies," *ETH Zurich, Department of Civil, Environmental and Geomatic Engineering*, 2012.

[5] P. H. Pathak, X. Feng, P. Hu, and P. Mohapatra, "Visible light communication, networking, and sensing: A survey, potential and challenges," *IEEE communications surveys & tutorials*, vol. 17, no. 4, pp. 2047–2077, 2015.

[6] Z. Vatansever, J. Lian, and M. Brandt-Pearce, "Indoor mapping using the VLC channel state information," in *2018 52nd Asilomar Conference on Signals, Systems, and Computers*, Oct 2018.

[7] IndoorAtlas, "The rise of indoor positioning," Tech. Rep., 2016. [Online]. Available: https://www.indooratlas.com/wp-content/uploads/2016/09/A-2016-Global-Research-Report-On-The-Indoor-Positioning-Market.pdf

[8] F. Dellaert, W. Burgard, D. Fox, and S. Thrun, "Using the condensation algorithm for robust, vision-based mobile robot localization," in *Computer Vision and Pattern Recognition, 1999. IEEE Computer Society Conference on.*, vol. 2. IEEE, 1999, pp. 588–594.

[9] R. Mur-Artal, J. M. M. Montiel, and J. D. Tardos, "ORB-SLAM: a versatile and accurate monocular SLAM system," *IEEE Transactions on Robotics*, vol. 31, no. 5, pp. 1147–1163, 2015.

[10] A. Elfes, "Sonar-based real-world mapping and navigation," *IEEE Journal on Robotics and Automation*, vol. 3, no. 3, pp. 249–265, June 1987.

[11] F. Li, C. Zhao, G. Ding, J. Gong, C. Liu, and F. Zhao, "A reliable and accurate indoor localization method using phone inertial sensors," in *Proceedings of the 2012 ACM Conference on Ubiquitous Computing*, ser. UbiComp '12. New York, NY, USA: ACM, 2012, pp. 421–430.

[12] T. Gigl, G. J. M. Janssen, V. Dizdarevic, K. Witrisal, and Z. Irahhauten, "Analysis of a UWB indoor positioning system based on received signal strength," in *2007 4th Workshop on Positioning, Navigation and Communication*, March 2007, pp. 97–101.

[13] R. Faragher and R. Harle, "Location fingerprinting with Bluetooth low energy beacons," *IEEE Journal on Selected Areas in Communications*, vol. 33, no. 11, pp. 2418–2428, Nov 2015.

[14] C. Yang and H. Shao, "Wi-Fi-based indoor positioning," *IEEE Communications Magazine*, vol. 53, no. 3, pp. 150–157, March 2015.

[15] A. Bekkali, H. Sanson, and M. Matsumoto, "RFID indoor positioning based on probabilistic RFID map and Kalman filtering," in *Wireless and Mobile Computing, Networking and Communications, 2007. WiMOB 2007. Third IEEE International Conference on.* IEEE, 2007, pp. 21–21.

[16] H. Zhang, J. Chen, and K. Zhang, "Reliable and efficient RFID-based localization for mobile robot," in *2013 IEEE International Symposium on Robotic and Sensors Environments (ROSE)*, Oct 2013, pp. 184–189.

[17] M. K. Weizhi Zhang, M. I. Sakib Chowdhury, "Asynchronous indoor positioning system based on visible light communications," *Optical Engineering*, vol. 53, no. 4, pp. 1 – 10, 2014.

[18] K. Gligoric, M. Ajmani, D. Vukobratovic, and S. Sinanovic, "Visible light communications-based indoor positioning via compressed sensing," *IEEE Communications Letters*, vol. 22, no. 7, pp. 1410–1413, July 2018.

[19] Z. Vatansever and M. Brandt-Pearce, "Visible light positioning with diffusing lamps using an extended Kalman filter," in *2017 IEEE Wireless Communications and Networking Conference (WCNC)*, March 2017, pp. 1–6.

[20] Y.-S. Kuo, P. Pannuto, K.-J. Hsiao, and P. Dutta, "Luxapose: Indoor positioning with mobile phones and visible light," in *Proceedings of the 20th Annual International Conference on Mobile Computing and Networking*, ser. MobiCom '14. New York, NY, USA: ACM, 2014, pp. 447–458.

[21] Y. U. Lee and M. Kavehrad, "Two hybrid positioning system design techniques with lighting LEDs and Ad-Hoc wireless network," *Consumer Electronics, IEEE Transactions on*, vol. 58, no. 4, pp. 1176–1184, November 2012.

[22] T.-H. Do and M. Yoo, "An in-depth survey of visible light communication based positioning systems," *Sensors*, vol. 16, no. 5, p. 678, 2016.

[23] X. Zhang, J. Duan, Y. Fu, and A. Shi, "Theoretical accuracy analysis of indoor visible light communication positioning system based on received signal strength indicator," *Journal of Lightwave Technology*, vol. 32, no. 21, pp. 3578–3584, 2014.

[24] S.-H. Yang, H.-S. Kim, Y.-H. Son, and S.-K. Han, "Three-dimensional visible light indoor localization using AOA and RSS with multiple optical receivers," *Journal of Lightwave Technology*, vol. 32, no. 14, pp. 2480–2485, 2014.

[25] L. Li, P. Hu, C. Peng, G. Shen, and F. Zhao, "Epsilon: A visible light based positioning system," in *11th USENIX Symposium on Networked Systems Design and Implementation (NSDI 14)*. Seattle, WA: USENIX Association, 2014, pp. 331–343.

[26] H. Steendam, "A 3-D positioning algorithm for AOA-based VLP with an aperture-based receiver," *IEEE Journal on Selected Areas in Communications*, vol. 36, no. 1, pp. 23–33, Jan 2018.

[27] C. Zhang and X. Zhang, "Pulsar: Towards ubiquitous visible light localization," in *Proceedings of the 23rd Annual International Conference on Mobile Computing and Networking*. ACM, 2017, pp. 208–221.

[28] B. Viel and M. Asplund, "Why is fingerprint-based indoor localization still so hard?" in *Pervasive Computing and Communications Workshops (PERCOM*

Workshops), 2014 IEEE International Conference on. IEEE, 2014, pp. 443–448.

[29] S. He and S. H. G. Chan, "Wi-Fi fingerprint-based indoor positioning: Recent advances and comparisons," *IEEE Communications Surveys Tutorials*, vol. 18, no. 1, pp. 466–490, Firstquarter 2016.

[30] B. Molina, E. Olivares, C. E. Palau, and M. Esteve, "A multimodal fingerprint-based indoor positioning system for airports," *IEEE Access*, vol. 6, pp. 10 092–10 106, 2018.

[31] J. Vongkulbhisal, B. Chantaramolee, Y. Zhao, and W. S. Mohammed, "A fingerprinting-based indoor localization system using intensity modulation of light emitting diodes," *Microwave and Optical Technology Letters*, vol. 54, no. 5, pp. 1218–1227, 2012.

[32] X. Guo, S. Shao, N. Ansari, and A. Khreishah, "Indoor localization using visible light via fusion of multiple classifiers," *IEEE Photonics Journal*, vol. 9, no. 6, pp. 1–16, 2017.

[33] M. Xu, W. Xia, Z. Jia, Y. Zhu, and L. Shen, "A VLC-based 3-D indoor positioning system using fingerprinting and k-nearest neighbor," in *Vehicular Technology Conference (VTC Spring), 2017 IEEE 85th.* IEEE, 2017, pp. 1–5.

[34] H. Hosseinianfar, M. Noshad, and M. Brandt-Pearce, "Positioning for visible light communication system exploiting multipath reflections," *arXiv preprint arXiv:1707.08203*, 2017.

[35] Z. Zheng, Y. Chen, T. He, L. Sun, and D. Chen, "Feature learning for fingerprint-based positioning in indoor environment," *International Journal of Distributed Sensor Networks*, vol. 11, no. 10, p. 452590, 2015.

[36] G. Mao, B. Fidan, and B. D. Anderson, "Wireless sensor network localization techniques," *Computer Networks*, vol. 51, no. 10, pp. 2529 – 2553, 2007.

[37] J. Guevara, A. R. Jiménez, J. C. Prieto, and F. Seco, "Auto-localization algorithm for local positioning systems," *Ad Hoc Networks*, vol. 10, no. 6, pp. 1090–1100, 2012.

[38] N. Thomas, D. Cruickshank, and D. Laurenson, "Calculation of mobile location using scatterer information," *Electronics Letters*, vol. 37, no. 19, pp. 1193–1194, 2001.

[39] V. Y. Zhang and A. K.-S. Wong, "Combined AOA and TOA NLOS localization with nonlinear programming in severe multipath environments," in *Wireless Communications and Networking Conference, 2009. WCNC 2009. IEEE.* IEEE, 2009, pp. 1–6.

[40] B. Y. Shikur and T. Weber, "TDOA/AOD/AOA localization in NLOS environments," in *Acoustics, Speech and Signal Processing (ICASSP), 2014 IEEE International Conference on.* IEEE, 2014, pp. 6518–6522.

[41] M. Kotaru, K. Joshi, D. Bharadia, and S. Katti, "Spotfi: Decimeter level localization using WiFi," in *ACM SIGCOMM Computer Communication Review*, vol. 45, no. 4. ACM, 2015, pp. 269–282.

[42] D. Vasisht, S. Kumar, and D. Katabi, "Decimeter-level localization with a single WiFi access point," in *13th USENIX Symposium on Networked Systems Design and Implementation NSDI 16*, 2016, pp. 165–178.

[43] E. Soltanaghaei, A. Kalyanaraman, and K. Whitehouse, "Multipath triangulation: Decimeter-level WiFi localization and orientation with a single unaided

receiver," in *Proceedings of the 16th Annual International Conference on Mobile Systems, Applications, and Services*, ser. MobiSys '18. New York, NY, USA: ACM, 2018, pp. 376–388.

[44] J. Zhang and S. Singh, "LOAM: Lidar odometry and mapping in real-time." in *Robotics: Science and Systems*, vol. 2, 2014, p. 9.

[45] Lumentum Operations LLC., "Making vehicles smarter and safer with diode laser-based 3D sensing," 2018.

[46] J. M. Kahn and J. R. Barry, "Wireless infrared communications," *Proceedings of the IEEE*, vol. 85, no. 2, pp. 265–298, Feb 1997.

[47] T. Komine and M. Nakagawa, "Fundamental analysis for visible-light communication system using LED lights," *Consumer Electronics, IEEE Transactions on*, vol. 50, no. 1, pp. 100–107, Feb 2004.

[48] J. Lian, M. Noshad, and M. Brandt-Pearce, "Multiuser MISO indoor visible light communications," in *Signals, Systems and Computers, 2014 48th Asilomar Conference on*, Nov 2014, pp. 1729–1733.

[49] M. Rahaim, G. Prince, and T. Little, "State estimation and motion tracking for spatially diverse VLC networks," in *Globecom Workshops (GC Wkshps), 2012 IEEE*, Dec 2012, pp. 1249–1253.

[50] X. R. Li and V. P. Jilkov, "Survey of maneuvering target tracking. Part I. Dynamic models," *IEEE Transactions on Aerospace and Electronic Systems*, vol. 39, no. 4, pp. 1333–1364, Oct 2003.

[51] S. Sarkka, "Bayesian filtering and smoothing," *Institute of Mathematical Statistics Textbooks, Cambridge University Press*, 2013.

[52] S. Thrun, W. Burgard, and D. Fox, *Probabilistic Robotics (Intelligent Robotics and Autonomous Agents).* The MIT Press, 2005.

[53] P. Newman, "EKF based navigation and SLAM." [Online]. Available: http://legolab.cs.au.dk/DigitalControl.dir/NXT/Lectures/Lecture9/SLAM%20Summer%20School%202004%20Newman.ppt

[54] R. E. Kalman, "A new approach to linear filtering and prediction problems," *Transactions of the ASME–Journal of Basic Engineering*, vol. 82, no. Series D, pp. 35–45, 1960.

[55] M. S. Arulampalam, S. Maskell, N. Gordon, and T. Clapp, "A tutorial on particle filters for online nonlinear/non-Gaussian Bayesian tracking," *IEEE Transactions on Signal Processing*, vol. 50, no. 2, pp. 174–188, Feb 2002.

[56] S. Thrun and M. Montemerlo, "The graph SLAM algorithm with applications to large-scale mapping of urban structures," *The International Journal of Robotics Research*, vol. 25, no. 5-6, pp. 403–429, 2006.

[57] W. Dargie and C. Poellabauer, *Fundamentals of wireless sensor networks: theory and practice.* John Wiley & Sons, 2010.

[58] M. Cao, B. D. Anderson, and A. S. Morse, "Sensor network localization with imprecise distances," *Systems & control letters*, vol. 55, no. 11, pp. 887–893, 2006.

[59] J. Luo, L. Fan, and H. Li, "Indoor positioning systems based on visible light communication: State of the art," *IEEE Communications Surveys Tutorials*, vol. 19, no. 4, pp. 2871–2893, Fourthquarter 2017.

[60] Z. Vatansever and M. Brandt-Pearce, “Effects of unknown shadowing and non-line-of-sight on indoor tracking using visible light,” in *MILCOM 2017 - 2017 IEEE Military Communications Conference (MILCOM)*, Oct 2017, pp. 501–506.

[61] ——, “Image-sourced fingerprinting for LED-based indoor tracking,” in *2017 51st Asilomar Conference on Signals, Systems, and Computers*, Oct 2017, pp. 903–907.

[62] D. Dardari, P. Closas, and P. M. Djuric, “Indoor tracking: Theory, methods, and technologies,” *IEEE Transactions on Vehicular Technology*, vol. 64, no. 4, pp. 1263–1278, April 2015.

[63] Z. Vatansever and M. Brandt-Pearce, “Hybrid indoor tracking using crowd-sourced measurements,” in *2017 26th International Conference on Computer Communication and Networks (ICCCN)*, July 2017, pp. 1–7.

[64] J. Lian and M. Brandt-Pearce, “A Multiuser MIMO Indoor Visible Light Communication System Using Spatial Multiplexing,” *Journal of Lightwave Technology*, vol. 35, no. 23, pp. 5024–5033, 2017.

[65] J. Armstrong, Y. A. Sekercioglu, and A. Neild, “Visible light positioning: a roadmap for international standardization,” *IEEE Communications Magazine*, vol. 51, pp. 68–73, 2013.

[66] P. Davidson and R. Piche, “A survey of selected indoor positioning methods for smartphones,” *IEEE Communications Surveys Tutorials*, vol. 19, no. 2, pp. 1347–1370, Secondquarter 2017.

[67] A. M. Hossain and W.-S. Soh, “A survey of calibration-free indoor positioning systems,” *Computer Communications*, vol. 66, pp. 1–13, 2015.

[68] C. Liu, A. Kiring, N. Salman, L. Mihaylova, and I. Esnaola, "A Kriging algorithm for location fingerprinting based on received signal strength," in *2015 Sensor Data Fusion: Trends, Solutions, Applications (SDF)*, Oct 2015, pp. 1–6.

[69] S.-H. Yang, D.-R. Kim, H.-S. Kim, Y.-H. Son, and S.-K. Han, "Visible light based high accuracy indoor localization using the extinction ratio distributions of light signals," *Microwave and Optical Technology Letters*, vol. 55, no. 6, pp. 1385–1389, 2013.

[70] A. M. Vegni and M. Biagi, "An indoor localization algorithm in a small-cell LED-based lighting system," in *2012 International Conference on Indoor Positioning and Indoor Navigation (IPIN)*, Nov 2012, pp. 1–7.

[71] L. Mitas and H. Mitasova, "Spatial interpolation," *Geographical information systems: principles, techniques, management and applications*, 1999.

[72] A. Sen, M. U. Gümüsay, A. Kavas, and U. Bulucu, "Programming an artificial neural network tool for spatial interpolation in GIS-A case study for indoor radio wave propagation of WLAN," *Sensors*, vol. 8, no. 9, pp. 5996–6014, 2008.

[73] G. B. Wright, "Radial basis function interpolation: Numerical and analytical developments," Ph.D. dissertation, University of Colorado at Boulder, Boulder, CO, 2003.

[74] F. G. Horowitz, P. Hornby, D. Bone, and M. Craig, "Fast multidimensional interpolations," *The 26th Proceedings of the Applications of Computers and Operations Research in the Minerals Industry: Soc. for Mining, Metallurgy and Exploration Inc*, pp. 53–56, 1996.

[75] C. Laoudias, P. Kemppi, and C. G. Panayiotou, "Localization using radial basis function networks and signal strength fingerprints in WLAN," in *GLOBECOM 2009 - 2009 IEEE Global Telecommunications Conference*, Nov 2009, pp. 1–6.

[76] J.-P. Costa, L. Pronzato, and E. Thierry, "A comparison between Kriging and radial basis function networks for nonlinear prediction," in *NSIP*, 1999.

[77] C. Poynton, *Digital Video and HDTV Algorithms and Interfaces*, 1st ed. San Francisco, CA, USA: Morgan Kaufmann Publishers Inc., 2003.

[78] V. Štruc and N. Pavešić, *Photometric normalization techniques for illumination invariance.* IGI-Global, 2011, pp. 279–300.

[79] R. Lippmann, "An introduction to computing with neural nets," *IEEE ASSP Magazine*, vol. 4, no. 2, pp. 4–22, Apr 1987.

[80] K. Langendoen and N. Reijers, "Distributed localization in wireless sensor networks: a quantitative comparison," *Computer networks*, vol. 43, no. 4, pp. 499–518, 2003.

[81] J. Blumenthal, R. Grossmann, F. Golatowski, and D. Timmermann, "Weighted centroid localization in Zigbee-based sensor networks," in *2007 IEEE International Symposium on Intelligent Signal Processing*, Oct 2007, pp. 1–6.

[82] B. Lee and J. Choi, "Multi-source sound localization using the competitive k-means clustering," in *2010 IEEE 15th Conference on Emerging Technologies Factory Automation (ETFA 2010)*, Sep. 2010, pp. 1–7.

[83] R. Stoleru and J. A. Stankovic, "Probability grid: A location estimation scheme for wireless sensor networks," in *2004 First Annual IEEE Communications So-*

ciety Conference on Sensor and Ad Hoc Communications and Networks, 2004. IEEE SECON 2004. IEEE, 2004, pp. 430–438.

[84] J. T. Flam, J. Jalden, and S. Chatterjee, "Gaussian mixture modeling for source localization," in *2011 IEEE International Conference on Acoustics, Speech and Signal Processing (ICASSP)*, May 2011, pp. 2604–2607.

[85] S. Pergoloni, M. Biagi, S. Colonnese, R. Cusani, and G. Scarano, "Optimized LEDs footprinting for indoor visible light communication networks," *IEEE Photonics Technology Letters*, vol. 28, no. 4, pp. 532–535, Feb 2016.

[86] J. Luo, L. Fan, and H. Li, "Indoor positioning systems based on visible light communication: State of the art," *IEEE Communications Surveys & Tutorials*, vol. 19, no. 4, pp. 2871–2893.

[87] Z. Jiao, B. Zhang, M. Liu, and C. Li, "Visible light communication based indoor positioning techniques," *IEEE Network*, vol. 31, no. 5, 2017.

[88] M. Noshad and M. Brandt-Pearce, "Can visible light communications provide Gb/s service?" *arXiv preprint arXiv:1308.3217*, 2013.

[89] R. Boubezari, H. Le Minh, Z. Ghassemlooy, and A. Bouridane, "Smartphone camera based visible light communication," *Journal of Lightwave Technology*, vol. 34, no. 17, pp. 4121–4127, 2016.

[90] R. Mur-Artal, J. M. M. Montiel, and J. D. Tardos, "ORB-SLAM: a versatile and accurate monocular SLAM system," *IEEE Transactions on Robotics*, vol. 31, no. 5, pp. 1147–1163, 2015.

[91] E. Menegatti, A. Zanella, S. Zilli, F. Zorzi, and E. Pagello, "Range-only SLAM with a mobile robot and a wireless sensor networks," in *2009 IEEE International Conference on Robotics and Automation*, May 2009, pp. 8–14.

[92] X. Zhang, K. Cui, M. Yao, H. Zhang, and Z. Xu, "Experimental characterization of indoor visible light communication channels," in *Communication Systems, Networks & Digital Signal Processing (CSNDSP), 2012 8th International Symposium on*. IEEE, 2012, pp. 1–5.

[93] T. S. Rappaport *et al.*, *Wireless communications: principles and practice*. prentice hall PTR New Jersey, 1996, vol. 2.

[94] Texas Instruments, "Nanosecond Laser Driver Reference Design for LiDAR," Tech. Rep., 2018. [Online]. Available: http://www.ti.com/lit/ug/tidue52/tidue52.pdf

[95] M. E. Warren, R. F. Carson, J. R. Joseph, T. Wilcox, P. Dacha, D. J. Abell, and K. J. Otis, "High-speed and scalable high-power VCSEL arrays and their applications," in *Vertical-Cavity Surface-Emitting Lasers XIX*, vol. 9381. International Society for Optics and Photonics, 2015, p. 93810C.

[96] M. A. Fischler and R. C. Bolles, "Random sample consensus: a paradigm for model fitting with applications to image analysis and automated cartography," *Communications of the ACM*, vol. 24, no. 6, pp. 381–395, 1981.

[97] Z. Vatansever, M. Brandt-Pearce, and N. Bezzo, "Localization in optical wireless sensor networks for IoT applications," in *2019 IEEE International Conference on Communications (ICC)*, 2019.